Saeed, Ali (2023) *On the dynamic effects upon unsteady cooling of Lithium-ion batteries*. PhD thesis.

https://theses.gla.ac.uk/84094/

On the dynamic effects upon unsteady cooling of Lithium-ion batteries

Ali Saeed

Submitted in fulfilment of the requirements for the
Degree of Doctor of Philosophy in Mechanical Engineering

Primary Supervisor: Prof. Manosh Paul
Secondary Supervisor: Dr Nader Karimi

James Watt School of Engineering
College of Science and Engineering
University of Glasgow

August 2023

Abstract

The consumption of fossil fuels has been recognised as a major contributor to climate change, air pollution, and environmental degradation. In response to the growing public awareness of these issues, regulatory bodies and the public are emphasising the need to reduce harmful gas emissions and our dependence on fossil fuels. The transport sector, in particular the automobile market, has been a significant source of pollutants, leading to a shift towards electric vehicles (EVs) to combat emissions.

The broader adoption of EVs faces many challenges related to their initial costs, driving range, and overall performance – all of which are linked to the battery cell. Battery themal management systems (BTMS) play a vital role in overcoming these barriers due to the direct influence on the battery cells' operational temperature to their performance.

While extensive research has focused on steady-state scenarios, the unsteady nature of EVs necessitates a deeper understanding. In particular, battery cooling is influenced by unsteady heat generation, extreme driving conditions, and mechanical vibrations. Therefore, robust BTMS technologies require dynamic tools capable of predicting the thermal evolution of battery cells.

This thesis utilises a battery module based on real cell dimensions and employs high-fidelity simulations to investigate various temporal scenarios. The research explores the impact of disturbances on the battery cells and evaluates the system linearity using Fast Fourier Transforms (FFT) and Phase portraits (Lissajous patterns).

Firstly, a battery module subjected to unsteady surface heat flux and the corresponding numerical data is analysed to examine the extent of nonlinearity of the thermal system. Water and nonfluids are found to be far better at attaining linearity. However, regardless of fluid type, as long as the disturbances are of low amplitudes and short, the system can be approximated as linear. Increasing the forcing frequency causes the nonlinearity of the system to increase.

Furthermore, a battery module is subjected to realistic transient scenarios from standard driving cycles. The resultant surface-averaged temperature of each battery cell is analysed to determine the maximum overshoot, settling, heating, and cooling times. The results show that water-cooled battery cells consistently remain within their safe operating range and exhibit quicker response times to changes in the internal generation compared to air. regardless of coolant type, short period ramps result in higher values of settling time.

Lastly, batteries can experience mechanical vibrations due to several reasons, such as road roughness, the effects of which have largely been unexplored. A series of high-fidelity numerical simulations of a vibration battery cell are conducted to attain further understanding of the heat transfer processes involved and to identify conditions under which the thermal dynamics can be predicted. The resultant data is analysed and shows that only the water-cooled battery cells under low modulation amplitudes can be characterised as linear. Using air always leads to a strongly nonlinear thermal response.

Table of Contents

List of Figures

List of Tables

Acknowledgements

Firstly, I would like to express my sincerest gratitude to Dr Nader Karimi and Dr Manosh Paul for being great supervisors and for their invaluable guidance and continuous support. I would also like to thank the other members of the academic staff, IT staff, and technical staff for assisting me where needed and enriching my time at the University of Glasgow.

My greatest thanks to my dearest parents and brothers for their continuous love and support throughout my studies and for always motivating me to keep moving forward.

I gratefully acknowledge the scholarship awarded to me by the College of Science & Engineering and the Engineering and Physical Sciences Research Council (EPSRC), making it possible for me to enrol in the PhD. Additionally, funding was provided by the Systems, Power and Energy (SPE) research division at the University of Glasgow concerning my research.

This project used the EPSRC-funded high-performance computing (HPC) centre Cirrus (Cirrus) and the SPE-funded ARCHIE-WeSt (ARCHIE-WeSt – Research Computing for the West of Scotland). The former facility was funded by EPSRC award number EP/R513222/1.

Author’s Declaration

The author confirms that the thesis comprises only of the author’s own research except where indicated. Standard reference practices are applied to any ideas or techniques from other works.

…………………………………….

Ali Saeed

August 2023

Nomenclature

A	Electrode area (m^2)
a	Amplitude
c_e	Electrolyte concentration (m·mol/L)
$c_{s,max}$	Lithium concentration maximum in both electrodes, solid phase (m·mol/L)
$c_{s,surf}$	Lithium concentration at the surface, solid phase (m·mol/L)
c_l	Lithium concentration, electrolyte phase (m·mol/L)
c_p	Specific heat capacity (J/kg·K)
D	Diameter (m)
dl	Length from inlet to battery cell (m)
F	Faraday constant (C/mol)
F_d	Discrete Fourier transform
f	Frequency (Hz)
g	Gravity (9.81 m/s^2)
Gr	Grashof number
G_k	Turbulent kinetic energy for velocity
G_b	Turbulent kinetic energy for buoyancy
h	Heat transfer coefficient ($W/m^2 \cdot K$)
H	Total model height (m)
I	Current (A)
j_0	Current density of exchange (A/m^2)
j_n	Local charge current density (A/m^2)
j^{Li}	Current density in the Li-ion battery cell (A/m^2)
k	Thermal conductivity (W/m·K)
k	Turbulent viscosity
k_e^{eff}	Effective electrolyte conductivity (S/m)
$k_{D,e}^{eff}$	Effective diffusion electrolyte conductivity (S/m)
k_s^{eff}	Effective solid conductivity (S/m)
k_0	Reaction rate constant
L	Total model length (m)
L_c	Length from inlet to battery cell (m)
m	Mass (kg)
ndd	Nondimensional delay
Nu	Nusselt number
$\overline{Nu}$	Time-averaged Nusselt number
n_e	Euclidean norm
P	Power (W)
p	Pressure (Pa)
q''	Heat flux (W/ m^2)

R	Universal Gas constant (J/K·mol)	u	Velocity (m/s)
Re	Reynolds Number	u'	Fluctuating velocity (m/s)
R_i	Internal resistance (Ω)	V	Voltage (V)
S_c	Heat source term (W/m^3)	V_s	Battery cell volume (m^3)
St	Strouhal number		
T	Temperature (K)	Δx	Cell-to-cell length internal (m)
t	time (s)	x, y, z	Cartesian coordinate system
t_d	Cross corelation time delay (s)	Y_M	Fluctuating dilatation
U_{eq}	Open circuit potential (Volts)		

Greek Symbols

α	Thermal diffusivity (m^2/s)	δ	Kronecker delta function
α_a	Anodic Charge transfer coefficient	δ_{nl}	Measure of nonlinearity
α_c	Cathodic Charge transfer coefficient	ν	Kinematic viscosity (m^2/s)
β	Coefficient of volume expansion	σ_ϵ	Turbulent Prandtl number for ϵ
ϵ	Dissipation rate	σ_k	Turbulent Prandtl number for k
ρ	Density (kg/m^3)	ϕ_s	Potential, solid phase (Volts)
μ	Dynamic viscosity (kg/m·s)	ϕ_e	Potential, electrolyte phase (Volts)
μ_t	Turbulent viscosity (kg/m·s)	ϕ_{f_SOU}	Face value 2nd order upwind
τ	Shear stress (Pa)	ϕ	Cell-centred value
η	Local over potential (V)	$\nabla\phi$	Cell-centred gradient

Subscripts

f	Fluid	i, j, k	Coordinate directions
S	Solid	ref	Reference
nf	Nanofluid	$surf$	Surface

List of Abbreviations

Abbreviation	Meaning
BTMS	Battery Thermal Management System
CBD	Central Business District
CFD	Computational Fluid Dynamics
CFL	Courant-Friedrichs-Lewy
CHT	Conjugate Heat Transfer
CPCM	Composite Phase Change Material
DCT	Dimensionless Cooling Time
DHT	Dimensionless Heating Time
DST	Dimensionless Settling Time
EV	Electric Vehicle
FFT	Fast Fourier Transforms
FTP	Federal Test Procedure
HEC	Hybrid Electric Vehicle
ICE	Internal Combustion Engine
IEA	International Energy Agency
Li-ion	Lithium ion
MSMD	Multi-Scale Multi-Domain
NYCC	New York City Cycle
P2D	Pseudo Two-Dimensional
PCM	Phase Change Material
PISO	Pressure Implicit with Splitting of Operator
RANS	Reynolds-Averages Navier Stokes
SIMPLE	Semi-Implicit Method for Pressure-Linked Equations
SISO	Single Input Single Output
UN ECE	United Nations Economic Commission for Europe
US-EPA	United States – Environmental Protection Agency
UUDS	Urban Dynamometer Driving Schedule

Publications stemming from this work

A. Saeed, N. Karimi, M.C. Paul, “Analysis of the unsteady thermal response of a Li-ion battery pack to dynamic loads”, Energy 231 (Sep. 2021), 120947, https://doi.org/10.1016/J.ENERGY.2021.120947.

A. Saeed, N. Karimi, M.C. Paul, “Computational assessment of the thermal response of a Li-ion battery module to transient loads”, Journal of Power Sources 552 (Dec. 2022), 232217, https://doi.org/10.1016/j.jpowsour.2022.232217.

A. Saeed, N. Karimi, M.C. Paul, “On the effects of harmonic axial vibration on the thermal response of a Li-ion battery cell - Characterisation of the system dynamics”, Applied Energy (Dec. 2023). Manuscript Submitted for review.

Chapter 1. Introduction

1.1 *Motivation*

The electrification of vehicles illustrates a transformative shift in the automotive industry. As public awareness of climate change and environmental degradation has increased, governments, agencies, automobile manufacturers, and consumers recognise the importance of reducing greenhouse gas emissions and dependence on fossil fuels [1]. As a result, automakers are boosting their attention to electric vehicles and hybrid-electric vehicles (HEV) as attractive alternatives to internal combustion engine (ICE) vehicles in helping reach environmental, societal, and health objectives. Thus, the motivation behind the electrification of cars can be summarised by three primary factors – (i) environmental concerns, (ii) energy security, and (iii) advancements in battery technology [2, 3].

Statistics by the U.S. Energy Information Administration and the House of Commons Business, Energy and Industrial Strategy Committee show that the transportation sector is one of the most significant contributors of carbon dioxide, with passenger vehicles accounting for a substantial portion [4]. EVs offer zero tailpipe emissions, making them essential in tackling air pollution and, consequently, the quality of human life. EVs enable the use of diverse energy sources, such as renewable energy, decreasing the reliance on imported oil and leading to solid and sustainable energy systems [5, 6]. Additionally, a significant portion of the fuel consumed by ICE vehicles is transformed into heat energy during the combustion cycle, further contributing to climate change. Whereas EVs are two to four times more efficient than traditional ICE vehicles, further reducing the overall footprint of the transport sector [7]. A report by the International Energy Agency (IEA), *"Global EV Outlook 2021"*, shows that EV fleets are growing at an incredible pace throughout several of the world's largest automobile markets, accounting for an almost 50% increase in 2020 compared to 2019 [1]. Thus, the automobile industry plays a vital role in mitigating climate change. A general wireframe of an EV with the battery pack highlighted in red and a view focused on the battery pack can be seen in Figures 1-1a and 1-1b, respectively.

The introduction of advanced battery technologies in the late 20th century has catapulted EV development. Although the electrification of vehicles offers several advantages, numerous factors influence the positive perception of EVs [8]. These factors include initial vehicle costs, driving range, and overall EV performance, all linked to the battery cell [9, 10]. Battery packs make up the most considerable capital required during the manufacturing phase. However, the costs of battery packs have continued to decrease with emerging energy storage solutions, particularly lithium-ion (Li-ion) and Li-ion-based battery cells [11]. Li-ion batteries offer lightweight, high-energy density, long life cycle, and improved safety compared to Lead-acid or Nickel-metal hybrid batteries [12]. Nevertheless, even when using Li-ion battery cells, EVs still have a shorter driving range than their counterparts. Figure 1-2 shows the typical composition of a Li-ion cell, a battery module comprising many battery cells and the makeup of a battery pack containing many battery modules.

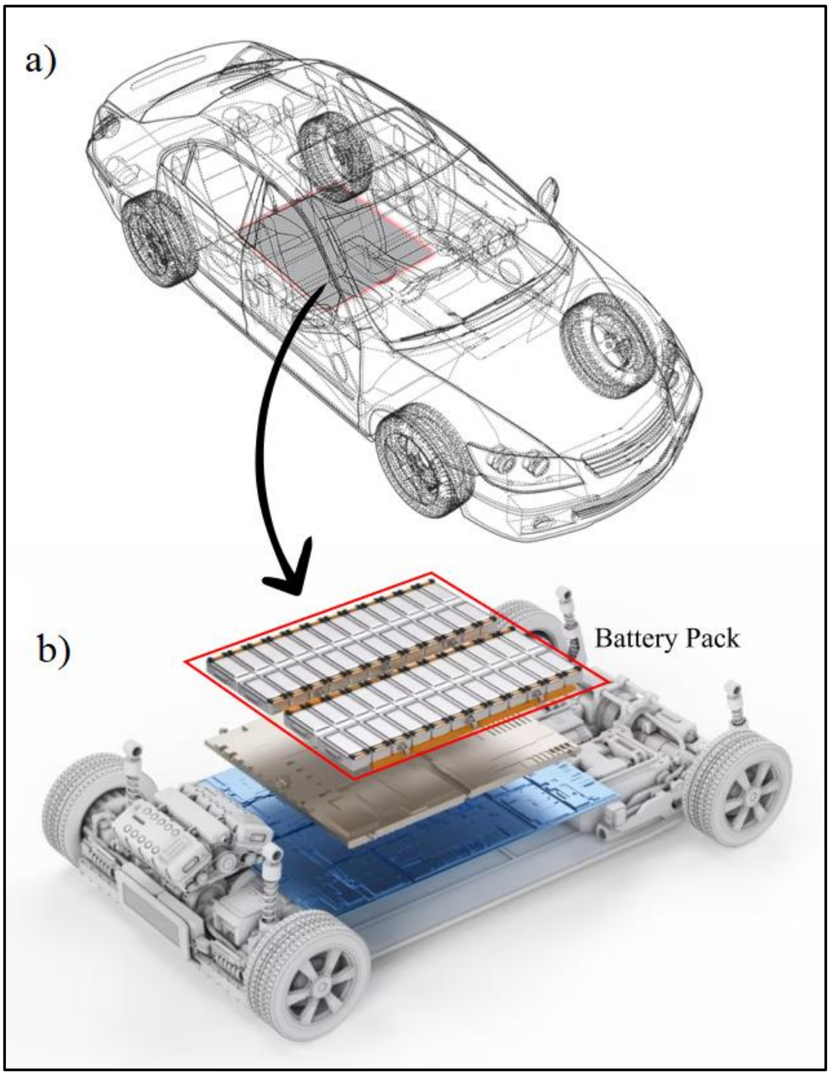

Figure 1-1 – a) General EV wireframe and b) Battery pack comprised of 48 battery modules [13, 14].

Finding energy storage solutions capable of quick charging, high mileage, and high-performance driving is imperative to ensure a continued trend in phasing out ICE vehicles and adopting EVs. However, the Battery safety and performance – charge and discharge capacity and life cycle – are dominated by its’ operational temperature. Consequently, the battery thermal management system is a crucial part of EVs' overall battery management system [12, 15].

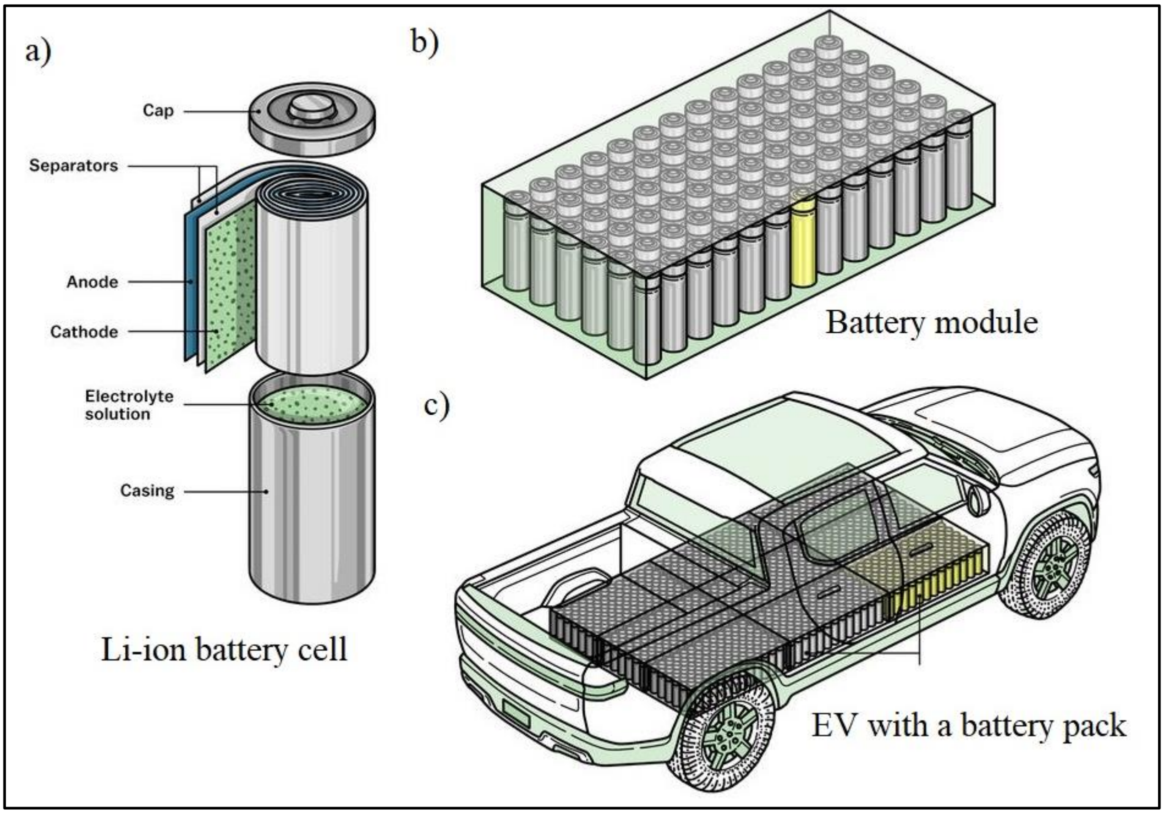

Figure 1-2 – a) Typical Li-ion battery cell composition, b) Battery module made up of many battery cells, and c) battery pack comprising of many battery modules [16].

The operational and design constraints posed on automakers by the thermal limitations [17, 18] for working batteries to ensure high performance and safety have made the underlying heat transfer dynamics of battery cells the centre of attention of extensive research [19–21].

1.2 *Battery Cell Thermal Limitations and Modelling*

It is challenging to develop a systematic and comprehensive cooling mechanism to ensure high-performance and safety of Li-ion batteries due to the sheer number of electrochemical materials and mixtures used by commercial batteries [22, 23]. Nevertheless, the temperature change of batteries is inevitable since they are affected by environmental and operational conditions [24]. Therefore, effective BTMSs are required to maintain the optimal temperature range and minimise the adverse effects on the battery cells' chemistry. Previous studies [25] have shown that Li-ion battery cells' optimal operational capacity is between 15°C and 35°C. Further, the maximum cell-to-cell temperature difference within a battery module should not exceed 5°C [26]. The combination of tight temperature tolerances, the battery cells' complex, and relatively unstable chemistry, unreasonably high or low temperatures can lead to irreversible electrolyte loss, threatening the battery cell's life and safety. Further, this threat is magnified when hundreds or thousands of cells are tightly connected in an EV [27]. The existence of significant temperature differences between the battery cells for prolonged periods can cause poor inconsistency within the battery module leading to cell-by-cell thermal variations. This further enlarges the hot spots within the battery module, creating a vicious cycle. The discrepancies will directly impact the charging and discharging capabilities of the entire battery pack, i.e. the weakest cell may determine the performance of the whole battery pack [28, 29]. The high energy density of Li-ion cells far outperforms all previous competing batteries; however, with the growing EV market, EVs demand higher energy density batteries and to amass more cells into a battery pack to increase the overall mileage. As a result, internal heat generation and heat accumulation within a battery module is further risen, acknowledging the importance of an effective BTMS.

Developing highly robust BTMSs requires more profound knowledge and understanding of three mechanisms – thermal generation, thermal transport, and thermal dissipation [30]. The three mechanisms can be assessed at either the cell level, where the thermal performance of a single battery cell can be researched, or at the module level, where a group of battery cells are evaluated together. A battery thermal workflow describing the two different levels of research can is shown in Figure 1-3. Assessing the thermal response of a single cell offers the value of heat generation, its transport throughout the battery cell, and the necessary boundary conditions required under steady and transient states [31]. Whereas the battery module shows the dispersion and management of the heat to ensure the battery cells remain within their optimal temperature range while minimising the cell-to-cell temperature variations [31, 32]. The combination of responses from both levels provides essential information, such as battery cell temperature history and distribution, which is vital to design powerful BTMSs for combating thermal runaway and ensuring safe operation.

A battery module's thermal configuration first requires understanding of the battery cell, which includes factors such as the cell geometry and thermal properties and, most importantly, the electrochemical characteristics of each battery cell. The three most popular battery cell shapes are prismatic, pouch, and cylindrical [33, 34]. The difference between the three battery types can be seen in Figure 1-4. The shape and thermal properties of the battery cell directly impact the current distribution within the battery cell and the internal and external thermal gradients. Prismatic and pouch cells are susceptible to deformation in high-pressure and humidity environments, impacting their safety and useability [35]. On the other hand, cylindrical batteries are less prone to deforming but suffer from uneven cooling – flow facing side of the battery cell will cool more than the backside. However, cylindrical cells are the most used shape within EVs since they are easier to manufacture and offer far easier thermal management control while tightly packed [33, 36]. Increasing the battery cell dimensions can lead to higher energy densities but directly impacts the surface area-to-volume ratio, resulting in the battery cell retaining more heat and higher temperature gradients.

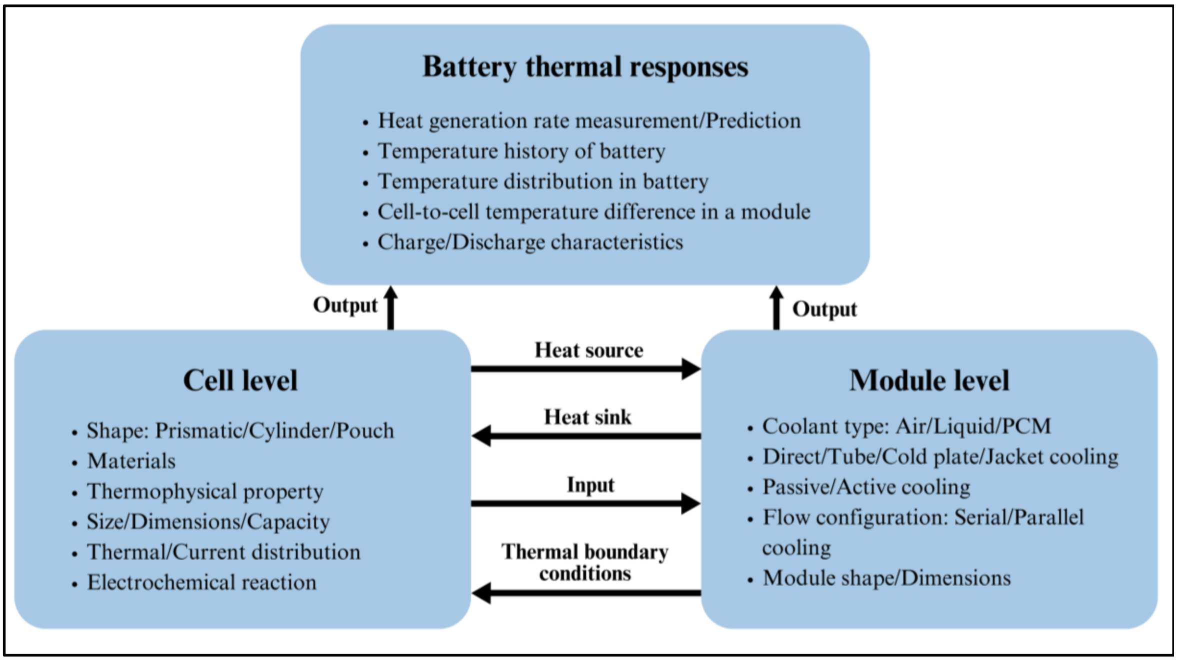

Figure 1-3 – Workflow for modelling for thermal issues at the cell and module level [30].

Furthermore, the most used coolants within EVs are air, liquid, and phase change materials (PCM) – with air being the most frequent [37]. Although it has poor thermal conductivity and heat capacity, its applicable simplicity and low cost makes air-based BTMS the preferred method of cooling by several manufacturers [30]. Generally, fans are used to propel air over the surface of the battery cells, as seen in Figure 1-5. However, the air temperature can rise significantly due to heat absorption from the battery cell near the inlet leading to higher temperatures for battery cells closer to the outlet – an undesirable result [38]. However, this result can be mitigated by increasing the surface heat transfer area or increasing the Reynolds number (Re) by increasing the flow rate.

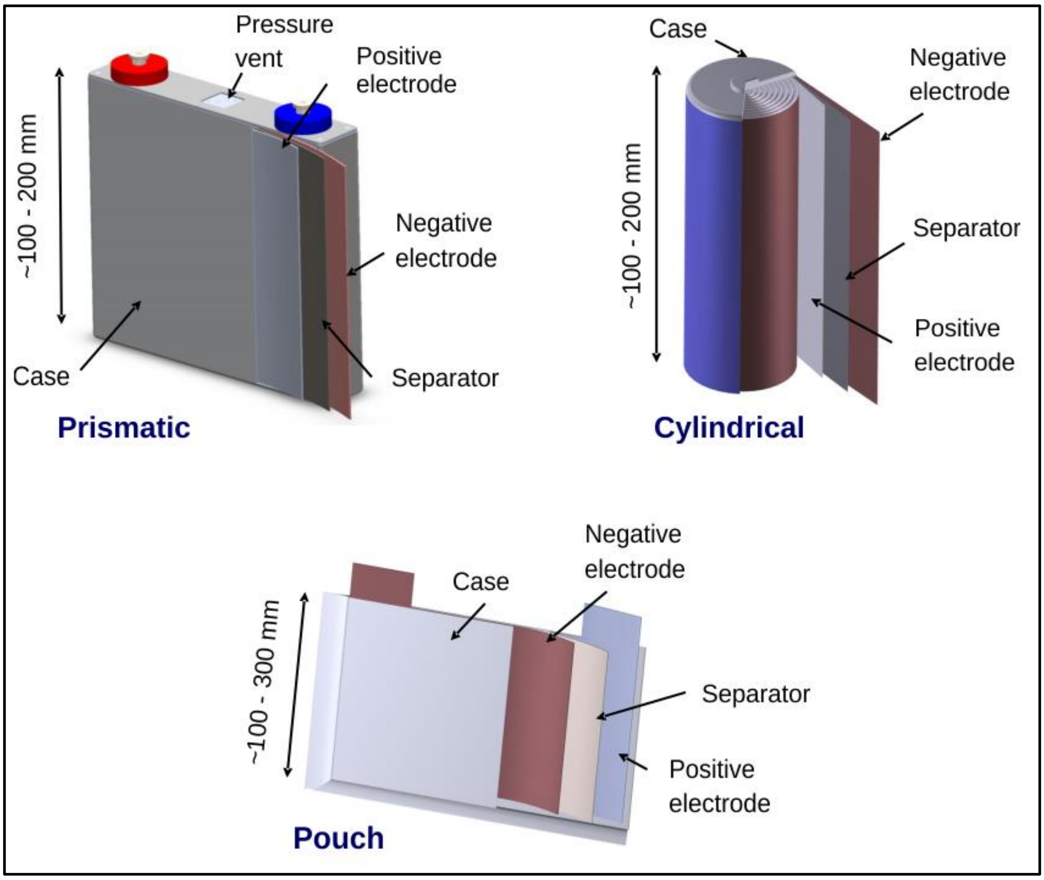

Figure 1-4 – Different battery cell types [39].

Moreover, battery modules are not configured in a purely series manner. Instead, manufacturers pack battery cells to maximise space and energy density using a series-parallel configuration, with the two standard methods for battery arrangement being aligned or staggered [40]. An example of both designs can be seen in Figure 1-6. In Figure 1-6a, 35 battery cells are organised in a 5S7P method – five cells in series and seven in parallel. Using the series-parallel approach over the series-only arrangement brings three main advantages. As previously stated, the first advantage is maximised space efficiency since most EVs come equipped with thousands of battery cells. Further, a study by Wang et al. [36] shows that a series-parallel configuration dramatically reduces the coolant flow path resulting in a more uniform cooling of the battery cells. Lastly, reducing the flow path decreases the pressure drop across the system, resulting in less parasitic power consumption.

Further, the thermal performance of the aligned and staggered arrangements was compared by Yang et al. [40]. The study used air as the coolant fluid and found that the maximum temperature is directly proportional to the longitudinal distance between each cell for the staggered arrangement. Whereas for the aligned setting, it is inversely proportional. The authors could further enhance the cell heat dissipation by increasing the spacing between each cell. However, this would lead to fewer tightly packed battery cells, sacrificing space efficiency. Although both arrangements offer different benefits, the ever-increasing need to pack more battery cells together into a single battery pack necessities the need to use the staggered arrangement for maximised space efficiency and being able to control the battery cells' temperature effectively.

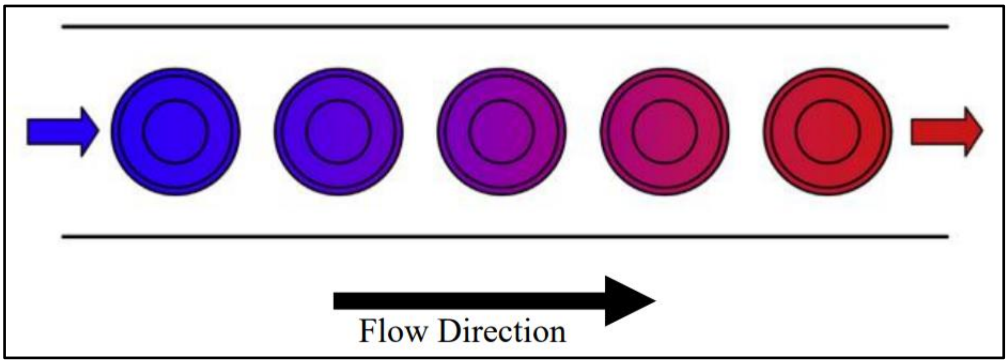

Figure 1-5 – Battery cell configuration (Fully series) [38]. Where blue are cooled battery cells and red are hot battery cells.

In large-scale battery modules (which contain hundreds of battery cells) or in cases of high battery cell discharge rates, the cooling capabilities of air cannot meet the requirements set within BTMSs [27, 41]. However, liquid coolants, such as water, offer numerous advantages over air. Liquid coolants require far less driving power (low Re required) while being over 35 hundred times more efficient [42]. Also, liquid cooling can significantly reduce the operational noise and the battery module can be more tightly packed without causing thermal problems [37]. However, operational complexities, high maintenance costs, and potential for leakage make liquid cooling less desirable for manufacturers. Nevertheless, a study by Bandhauer et al. [25] showed that the heat transfer problem from battery cells is a low conductivity problem rather than a heat flux issue. Thus, high thermal conductivity liquid-coolants such as water are ideal for cooling battery cells. As battery cell technologies further advance and bring about high energy and power density battery cells, the thermal problem might eventually become a heat flux issue.

Additionally, liquid cooling has two modes, direct and indirect cooling. The former is when the liquid flows over the battery cells. In contrast, the latter is when the liquid is used to cool another material responsible for extracting heat from the battery cells. An example of indirect cooling would be using a copper plate to extract heat from the surface of the battery cells, and the plate would be cooled using a liquid. Direct cooling offers some advantages over its counterpart; for example, it is far better at achieving temperature uniformity from one end of the battery cell to the other [33]. However, to effectively cool the battery module, the cooling media must have high thermal conductivity – to remove heat from the battery cells quickly, high heat capacity – to avoid boiling, and low viscosity – to avoid large pressure drops across the system. Coolants with low heat capacity would require far less energy to boil, introducing two-phase convection and adding further complexities to an already complex BTMS. Additionally, the coolant having direct contact with the battery cells can be dangerous in direct cooling, from the possibility of a short circuit to electrochemical corrosion, compromising the safety and lifetime of the battery pack. However, the possibility of a short circuit can be mitigated by using dielectric liquids, i.e. deionised water, as suggested in a study by Zhu et al. [43].

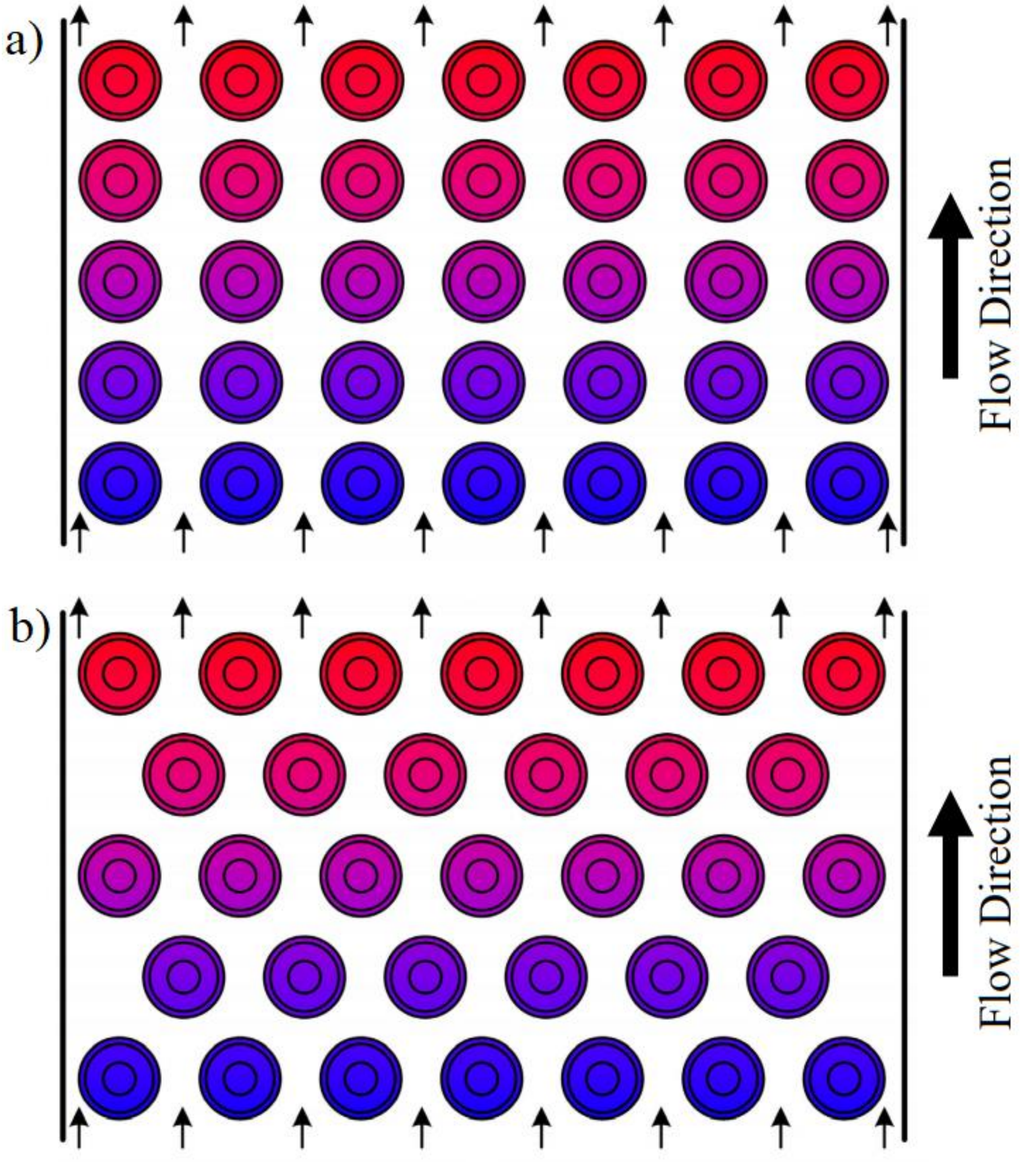

Figure 1-6 – Series-Parallel battery cell configuration. a) Aligned and b) staggered arrangement [38]. Where blue are cooled battery cells and red are hot battery cells.

Additionally, another potential liquid coolant for BTMSs are Nanofluids. The advancement of technology and the invention of high-performance devices requires fluids different from traditional fluids – water, oil, and oil-based mixtures. The fluids must be capable of high heat transfer rates for optimal performance, from the macro-level (engines) to the micro-level (microchips) [44, 45]. Modern nanotechnology has allowed the invention of nanofluids, which use a conventional fluid, like water, as the base fluid but carry suspended metallic nanoparticles throughout. Typically, metals are far better conductors of heat; therefore, nanofluids utilise the flow characteristics of a fluid with the thermal conductivity of metals, achieving the best of both. A one percent nanoparticle concentration significantly enhances the base fluid’s thermal properties, improving its’ convective heat transfer rate by up to 10% [44]. Therefore, many studies have been conducted to determine the impact of using nanofluids for cooling battery cells [46–48]. A study by Wiriyasart et al. [49] used a mixture of water and Titanium dioxide nanoparticles and found that adding nanoparticles in comparison to only having the base fluid led to significantly better cooling performance, resulting in a 27.6% decrease in the battery surface temperature. Study by Sefidan et al. [46] used a mixture of water and Aluminium oxide nanoparticles and found that the maximum cell temperature dropped from 16K to 24K depending on the cell arrangements and maintained far better temperature uniformity across the battery module. However, these studies are conducted numerically using an indirect battery cell cooling approach.

Nanofluids are modelled using two methods: single-phase or two-phase [50]. The former is modelled by taking the changes in the thermophysical properties – thermal conductivity and dynamic viscosity – and applying them to the base fluid [51]. The latter is when the nanofluids’ fluid and solid phases are treated separately. The first modelling method is far simple and easy to compute, whereas two-phase modelling is far more complicated and computationally expensive. Therefore, in the following thesis, nanofluids are modelled using the single-phase method.

1.3 *Aims and Objectives*

The overall objectives of this thesis are three-fold. First, it aims to provide a further understanding of heat transfer with an unsteady output from a battery module using different cooling mediums. The heat transfer characteristics are broken down into simpler harmonics and studied in greater detail to find areas where the thermal output from a battery cell can be predicted and where the predictions fail due to complex harmonics. Second, assess the ability of a BTMS to react to realistic scenarios in which much power is drawn from a battery module in a short period. The delay in response to the heating up of the battery cell and the time taken to cool down each battery cell back to its original temperature are studied in detail. Lastly, attain a better understanding of the thermal aspects of a battery cell due to vibrations. In particular, the influence of different vibrational frequencies and amplitudes is carefully examined. The specific objectives of this thesis are as follows:

- Develop a numerical heat transfer model using a realistic battery module in which the battery cells undergo unsteady thermal inputs based on preexisting data.
- Compare the numerical results against other numerical and experimental data to ensure the validity of the numerical model.
- Using numerous coolant fluids, analysing the spatiotemporal evolution in Nusselt number and battery cell temperatures.
- Analyse the nonlinearity of the dynamic response of heat convection and determine parameters in which the battery cell behaviour can and cannot be predicted.

Chapter 2. Literature Review

2.1 *Existing research*

The rapid development of EVs has accelerated the trend for more significant research. Therefore, many theoretical, numerical, and experimental studies have been conducted over the last decade to understand the thermal characteristics and heat generation of battery packs/modules/cells.

Studies by Yang et al. [40], Chu et al. [52], Panchal et al. [53], and Ling et al. [54] have numerically studied battery thermal management systems using varying designs but have focused on understanding the thermal behaviour of the battery cells. Yang et al. [40] used a two-dimensional conjugate heat transfer (CHT) model coupled with a one-dimensional electrochemical model to study the impact of the cooling performance of a battery module to varying designs for optimising airflow. The longitudinal and radial distance between the battery cells heavily impacts the fan power required to cool the battery cells effectively. However, there is a critical point at which the impact reverses due to the recirculation of air behind each battery cell, causing large temperature gradients to develop within each battery cell. The BTMS cooling configuration used by the authors can be seen in Figure 2-1; this figure shows a series-parallel, staggered battery cell arrangement.

Chu et al. [52] used the parallel-series design to model a large battery pack with indirect liquid cooling. The authors verified their design using experimental data and found that the BTMS's effectiveness highly depends on the heat transfer area. Increasing the cross-sectional ratio of the coolant could lower the maximum battery cell temperature by up to 2.5^{o}C, and the heat transfer rate could be further improved by increasing the number of cooling walls. However, this method would incur large pressure drops across the system, causing considerable power required to drive the fluid. These results were also confirmed by Zhang et al. [55]. Zhang et al. [55] also found that increasing the coolant velocity did improve battery cell surface temperature but incurred more significant gradients within each battery cell due to heat dissipation from the cell surface to the surroundings leading to an overall worse outcome.

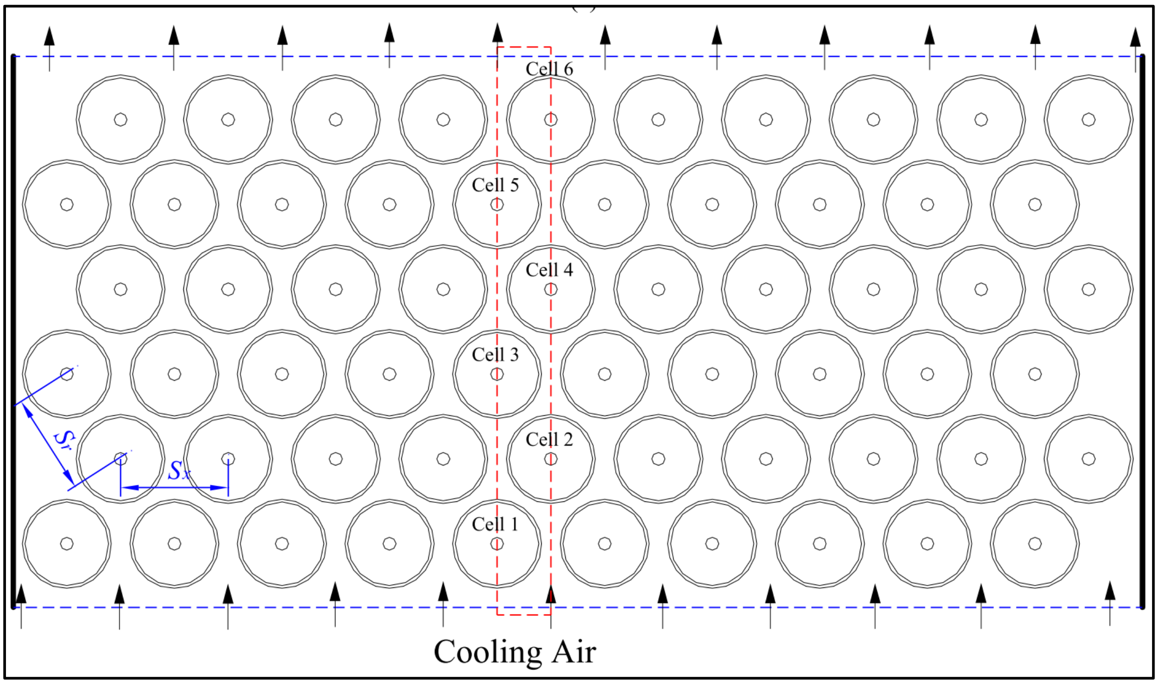

Figure 2-1 – BTMS cooling configuration (staggered arrangement) by Yang et al. [40]. Red section used during analysis. Where S_r and S_x are the radial and x-axis separation distance.

Moreover, Panchal et al. [53] studied the heat transfer of a single battery using indirect liquid cooling, like Chu et al. [52]. However, Panchal et al. [53] used microchannels around the battery cell, whereas Chu et al. [52] used cooling walls. The authors used Starccm+ as their numerical modelling software and verified their design using experimental data. Increasing the discharge rate of the battery cell led to a more significant temperature distribution and higher heat flux measurements across different parts of the battery cell. Additionally, investigations have also been conducted by Ling et al. [54], Pesaran [31], Chen et al. [37], and Karimi and Li [56] on varying BTMS designs to optimise the heat transfer rate and maintain optimal battery temperature for safe operation. The preceding literature review indicates that the existing BTMSs are primarily concerned with accurately evaluating the temperature field of the cooling fluid and heat generation inside battery cells. However, due to the highly unsteady nature of EVs, steady-state cases rarely apply to real life. Thus, a summary of the formally stated literature is given. More detail on the steady-state cases can be found in BTMS review papers from different years; 2023 [19, 57, 58], 2022 [18, 20, 59, 60], and 2021 [17, 21, 61, 62].

With the above in mind, it is imperative to understand the thermal behaviour of battery modules/cells under unsteady conditions, which needs to be addressed in most studies due to the highly complex nature of the problem as well as the extensive computational resource requirement. Nevertheless, few studies exist on the transient (ramps/step change) [63–65] and unsteady (sinusoidal) [38, 66, 67] nature of battery cells. Wang et al. [38] investigated the thermal management of a Li-ion battery module under dynamic loads using numerical and experimental methods. The authors utilised a detailed computational fluid dynamic (CFD) analysis to create a reduced-order model capable of predicting the battery surface temperature using far less computational resources. The experimental setup comprised four cylindrical battery cells excited by a dynamic profile and a fixed fan, as shown in Figure 2-2. The fixed fan controller used a feedback loop from the battery surface temperature sensors to reduce or turn off the airflow and avoid over-cooling. The feedback loop allowed the investigator to ensure the battery cells would remain within their optimal temperature range while minimising fan power consumption. The authors found that using a control algorithm to actively cool the battery module reduced parasitic power consumption by up to 30% compared to the same scenario using continuous cooling. Mahamud and Park [66] numerically studied the impact on the thermal performance of a fully-series battery module using reciprocating airflow. The authors used a single, fixed fan and flip doors to change the flow direction to improve temperature uniformity. The investigation found that using a reciprocating airflow reduced the cell-to-cell temperature by 4^{o}C – a 72% decrease in comparison to a non-reciprocating flow.

Additionally, Zhang et al. [67] numerically investigated optimisation techniques to enhance the thermal performance of air-cooled BTMSs by developing an efficient transient heat transfer model. The authors validated their model by comparing it against experimental data. They concluded that the transient heat transfer model could effectively predict the heat transfer rate and temperature of the battery cells at a low cost compared to full model simulations. Further, the authors suggested coolant channel optimisation techniques to enhance the cooling performance and reduce power requirements under different flow rates. Huang et al. [63] studied a battery module’s transient and ultimate thermal behaviour using indirect liquid cooling. The authors used a central cold plate as the BTMS and focused on understanding the relationship between discharge rate, inlet flow rate, and the corresponding heat transfer coefficient. The investigation found that increasing the flow rate of water will directly improve the cooling performance of the BTMS, as expected. However, the authors found an upper limit to the flow rate, after which the BTMS would no longer be effective in cooling the battery cells. An explanation of the upper limit could be the existence of large pressure drops across the system, decreasing the overall system performance. Moreover, an abrupt change in the inlet flow rate would cause the BTMS response time to experience a hysteresis effect. At the end of the study, Huang et al. [63] presented two correlations, one for the Nusselt number and another for the time delay against the battery cell discharge rate.

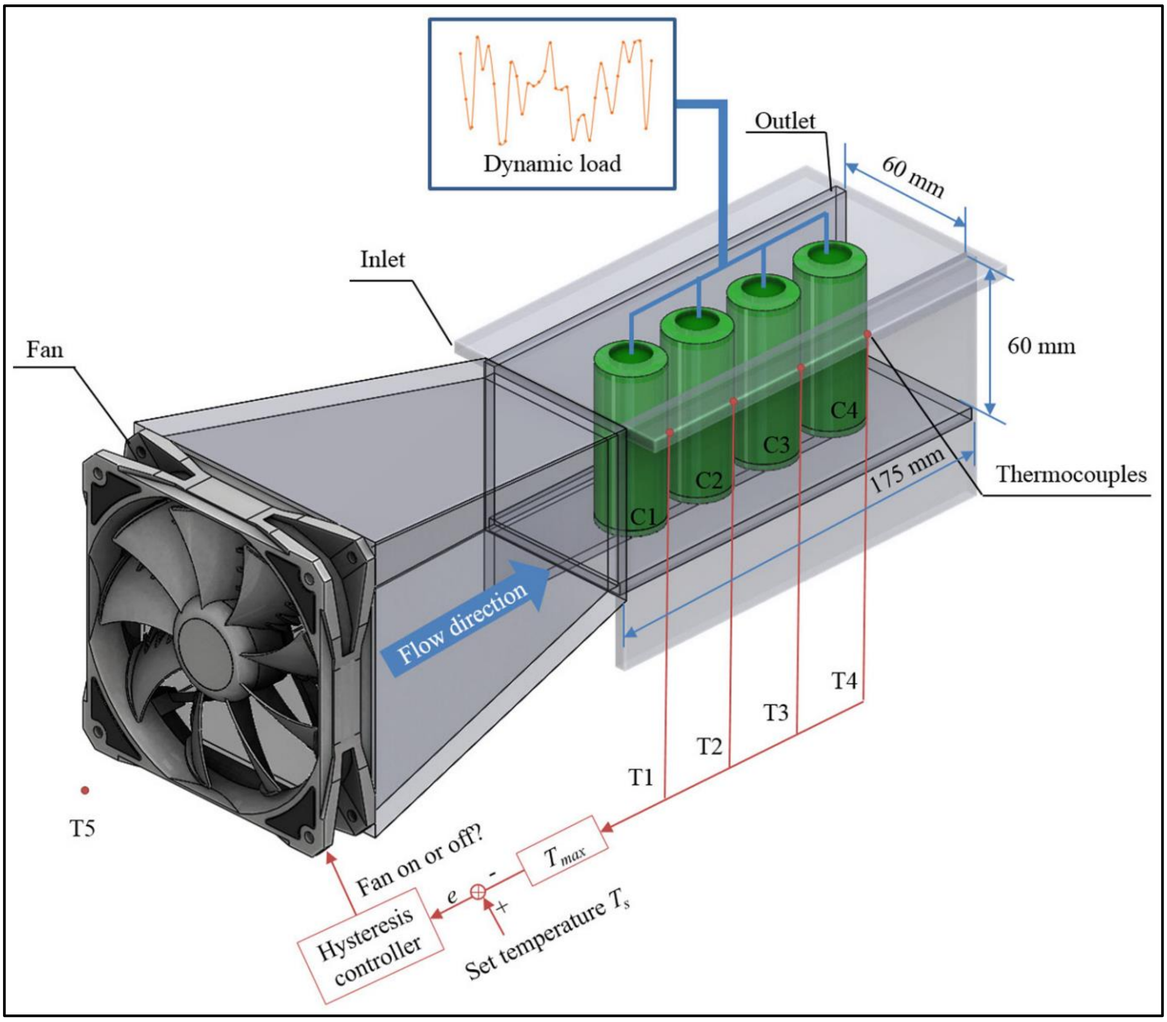

Figure 2-2 – Experimental setup used by Wang et al. [38].

The thermal performance of mini-channel cold plate BTMS under transient heat loads was numerically investigated by Fang et al. [64]. The study focused on the effects of changing the coolant flow rate, heat flux, and channel numbers on the overall performance of the BTMS. As expected, increasing the flow rate decreased the overall average temperature of the battery module and the cell-to-cell temperature deviation. However, much like the study by Huang et al. [63], Fang et al. [64] also found an upper limit to the flow, where exceeding this limit would begin to impact the BTMS negatively. The investigation revealed that the battery cell temperatures immediately increased by increasing the heat flux. Increasing the number of channels improved the performance of the cold plate slightly; however, it could lead to worse temperature uniformity due to a decrease in the per-channel flow velocity. Zhu et al. [65] developed an experimental setup to test a battery thermal management system's start-up and transient thermal behaviour. The study focused on understanding the effect of the flow rate, heat flux, and cold-source temperature on the start time delay of the BTMS and the corresponding transient thermal impact on the battery cells. As the flow rate of the refrigerant is decreased, the transient performance of the system is improved, leading to a quicker start-up. Thus, a quicker start-up allows the BTMS to combat changes in the battery cell temperature more effectively, lowering the average temperature and the maximum temperature difference. Increasing the heat flux improved the transient performance of the BTMS initially; however, increasing the heat flux above a certain point led to a weakened performance.

The battery cells within a battery module are naturally subject to continuous vibrational excitation due to numerous factors: such as vehicle acceleration, deceleration, and road roughness [68]. Although the vibrations are inherently random, they are dominated by suspension systems and settings. However, only a few studies have chosen to study the impact of vibration on the thermal performance of a BTMS, such as [69–71]. Shukla et al. [69] investigated the impact on the thermal fields of Li-ion batteries under vibration. The authors focused on understanding each battery cell's discharge temperature under three different frequencies and amplitudes. The investigation found that introducing vibration to the system dramatically influences the transient temperature distribution, and increasing the vibrational frequency further impacts the output surface temperature of each battery cell. Moreover, the battery cell's top region (negative electrode) heats faster than the rest. However, a uniform temperature distribution is eventually reached. Finally, a maximum change of 5^{o}C is observed when comparing the temperature distribution results of no vibration vs trainset cases.

Zhang et al. [70] studied the impact of mechanical vibrations on the thermal fields of a small battery pack cooling using composite PCMs (CPCM). Much like Shukla et al. [69], Zhang et al. [70] also utilised an experimental approach to the study; however, they opted to use prismatic battery cells rather than cylindrical ones. The authors choose to study a frequency range of 10-30 Hz with a minimum vibration amplitude of two and a maximum amplitude of four millimetres. The study found that small vibrations enhanced the heat transfer characteristics of the CPCM, which aided in prolonging the latent heat utilisation of the CPCM, extending the optimal battery operating range. However, too low, too high, or prolonged periods of frequencies negatively impact heat transfer. Finally, changes in the vibration frequency proved to have the most significant impact on the performance of the BTMS, whereas changing the vibration amplitude led to minute differences in the heat transfer properties of the battery cells. Another study on understanding the vibration impact on the trainset thermal of a battery and the corresponding performance of a BTMS was conducted by Joshy et al. [72]. The authors also used an experimental approach, however, used a PCM instead of a CPCM. The investigation found that increasing the vibrational frequency and amplitude caused the battery cell surface temperatures to increase. Further, at low discharge rate values, frequency significantly impacts the battery cells' surface temperature compared to the vibrational amplitude. However, at high discharge rate values, the vibrational frequency and amplitude impact the battery cells' surface temperature rise.

2.2 *Electrochemistry*

Electrochemistry is the process of electron transfer across a solution/electrode interface due to chemical reactions, a vital process that allows batteries to become energy storage devices [73]. Li-ion battery cells transfer Lithium-ions and electrons from the anode to the cathode across an electrolyte layer. During discharge, the anode produces positively charged Li-ions and negatively charged electrons during an oxidation half-reaction. Once the Li-ions move through the electrolyte and the electrons move through the external circuit – creating power – they recombine at the cathode in a reduction half-reaction [73, 74]. During discharge, the ions and electrons move from the negative electrode (anode) to the positive electrode (cathode) and during charging, these reactions and transports are reversed [75]. Figure 2-3 visually represents the charging and discharging process in a Li-ion cell.

This process can be described using the following chemistry equations [73]. The anode half-reaction of a typical Li-ion cell using graphite is

$$LiC_6 \rightleftharpoons C_6 + Li^+ + e^- \tag{2.1}$$

The cathode half-reaction for a Lithium-Cobalt oxide substrate is

$$CoO_2 + Li^+ + e^- \rightleftharpoons LiCoO_2 \tag{2.2}$$

Thus, the full reaction during discharge is

$$LiC_6 + CoO_2 \rightleftharpoons C_6 + LiCoO_2 \tag{2.3}$$

During charging, Eq. (2.3) is reversed. Electrochemistry is an essential aspect of battery cells; therefore, vital for use within BTMS research to accurately represent the charge and discharging cycle. Furthermore, the operation characteristics of a battery cell are tied to its' temperature – the working temperature of the battery cell directly influences the electrochemistry of that cell. However, due to the sudden need and climb of BTMS research, few commercially available packages are capable of accurately evaluating a battery cell. Available packages are computationally extremely demanding; thus, most research takes the experimental route, as the literature shows.

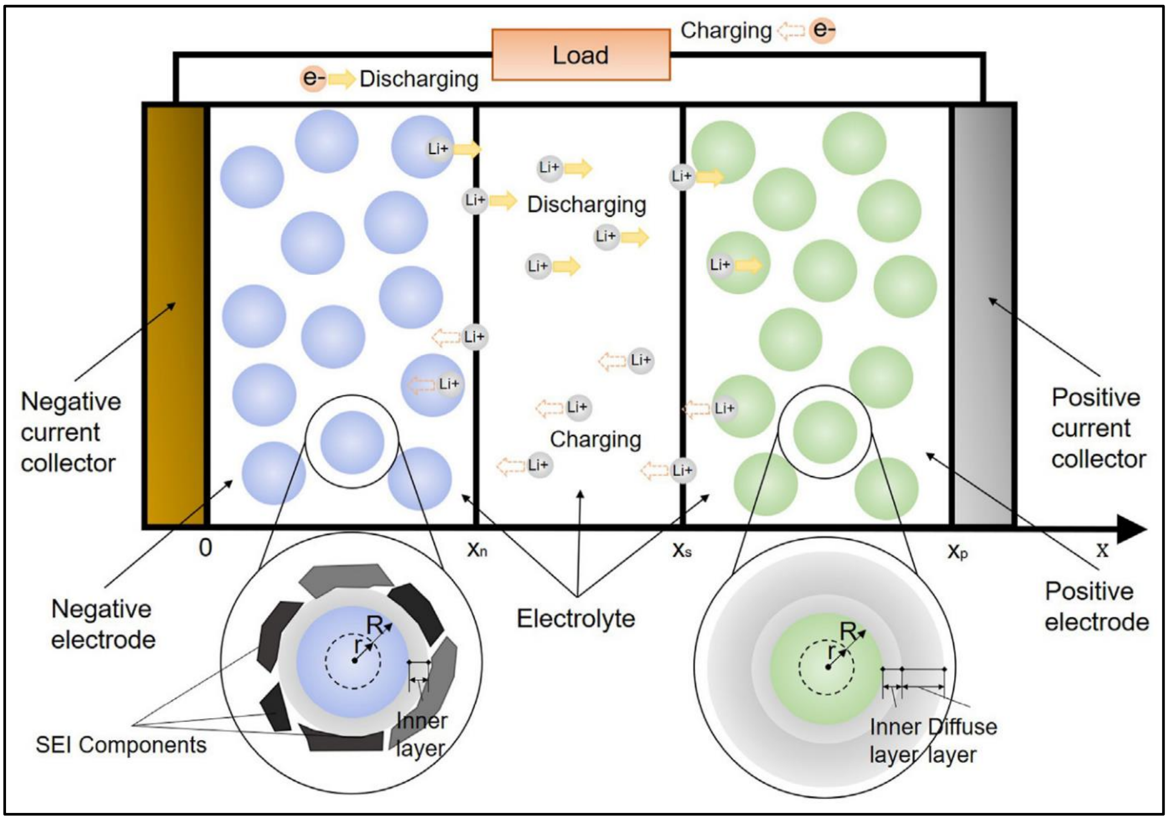

Figure 2-3 – Electrochemical structure of a Lithium-ion battery cell during charging and discharging [76].

Regardless, there have been numerous studies on implementing and improving electrochemistry in commercial CFD packages to improve numerical simulations of battery storage devices. The Pseudo 2D (P2D) scaling model was first proposed by Doyle, Fuller and Newman in 1993 [77] and later improved in 1994 [78]. The P2D model describes the inner workings of a Li-ion battery cell in detail with formulas based on the theory of the concentrated solution and the porous electrode. The P2D has been used as a building block for developing improved or simplified electrochemical models, which have been commonly used in battery state estimation and terminal voltage simulations. Studies by Ma et al. [79] and Dao et al. [80] developed simplified electrochemical models based on the modelling process of the P2D model and verified the simulated accuracy of the voltage estimation under charging and discharging conditions. Further, another study [81] simplified the P2D model, establishing a single-particle model considering the electrolyte phase, and verified its accuracy to sinusoidal excitations of current. However, Li-ion batteries are used in a wide array of applications (from watches, pacemakers, and mobile phones to portable power packs and automobiles), thus, experiencing a wide frequency range of excitation [82]. Therefore, the electrochemical model must reflect accurate characteristics of a Li-ion battery cell under all excitations over a wide frequency band.

Zhang et al. [76] tested the accuracy of the P2D model by numerically exciting a Li-ion battery cell within a frequency band of 0.01 kHz to 1 kHz. The authors stated that the P2D model can accurately capture the behaviour of the battery cell at high frequencies; however, it fails to achieve good accuracy at low frequencies. The study also presented a new and improved model capable of increased accuracy in the time and frequency domain. Panchal et al. [83] present a mathematical model capable of predicting the transient voltage and temperature distributions of a Li-ion battery cell. The authors first experimentally analysed the behaviour of a 18650 battery cell under four constant discharge rates. Later, they used the experimental data to develop and improve a numerical model using ANSYS CFD software. The study found that the experimental and numerical data on the voltage and temperature profiles were in close agreement.

Moreover, Li et al. [84] experimentally and numerically studied the voltage and temperature profiles of a prismatic Li-ion battery cell for the sole purpose of improving the ANSYS Fluent MSMD electrochemical model coupled with mass, charge, energy conservation, and electrochemical kinetics. The authors found that separating the heat generation terms into their respective parts and improving the heat sources improved the overall temperature results of the numerical analysis. This phenomenon was also confirmed by Kim et al. [85] and Meng et al. [86], who found that most heat generation and high-temperature gradients were due to electrical contact resistance. The distribution of discharge voltage and current density were also examined and agreed well with the experimental results. Finally, the non-uniformity in the voltage and current distribution was due to the shape of the battery cell rather than inaccuracies with the model.

2.3 *Research needs*

The literature on battery thermal management systems is relatively new, with most research occurring in the last decade. Therefore, there is still much to be unearthed regarding finding ways to best optimise a BTMS to operate battery cells within their optimal range and ensure the safety of the battery pack. Most research is primarily concerned with accurately evaluating the temperature of the coolant and heat generation inside the battery cells. Unsurprisingly, this demands costly computations to accurately predict the thermal behaviour of the battery cells and the BTMS. Ultimately, the results from these studies will be used to improve or design new BTMSs to prevent thermal runaway of the battery pack. Furthermore, most literature uses steady-state scenarios, whereas the operation of EVs is highly dynamic by nature. Thus, high-order models are difficult to be utilised within BTMS [38]. There is a pressing need for low-cost predictive models to detect changes in the battery cells' behaviour in advance. System dynamics can be studied from a single point or set of points, assuming that the dynamics of the measured quantity can also represent the dynamics of the whole system. Nevertheless, most studies on BTMS have concerned themselves with steady-state cases and have neglected the transient or unsteady nature of battery cells despite being critical in designing BTMSs. Therefore, there is a need for further research to understand the limits at which linear predictive tools can no longer be used to predict the thermal dynamics of a battery cell, further, how a battery module/cells are impacted, resulting in unsafe operation by different unsteady/transient scenarios.

2.4 *Overview*

The methods used in this work on battery thermal management and the numerical and theoretical details of the work shown throughout this thesis are presented in Chapter 3. The studies on unsteady battery surface heat flux, transient loads, and battery cell vibration are in Chapters 4, 5, and 6, respectively. A summary of the conclusions of the current work and suggestions for future research are in Chapter 7. Appendix A contains the main MATLAB code written to post-process the numerical datasets. Appendix B contains the C-code, which introduces vibration to the battery cell.

Chapter 3. Theoretical and Numerical Methods

This chapter introduces the general methodology used to conduct the numerical analysis presented in this thesis; any specific set of equations or methods are discussed before each results chapter. The first part describes the Reynolds-Averaged Navier-Stokes (RANS) equations for turbulent flow. Then the numerical model of choice and discretisation scheme are discussed. Finally, the pressure solver method is discussed.

3.1 *Governing equations*

The Reynolds-Averaged Navier-Stokes (RANS) are time-averaged equations describing the motion of the fluid flow. RANS equations use Reynolds decomposition, where the instantaneous quantities are broken into their time-averaged and fluctuating portions, as proposed by Reynolds [87] in 1895. These equations can be used to give approximate time-averaged solutions to the Navier-Stokes equations.

The mass continuity equation expressing the law of mass conservation using the Einstein notation is given by [88]

$$\frac{\partial \rho_f}{\partial t} + \frac{\partial}{\partial x_j}\left(\rho_f u_j\right) = 0 \tag{3.1}$$

where, ρ_f is the fluid density, u is the velocity component, t is the time coordinate, and j denotes x, y, and z axial directions terms using Einstein notation.

Newton's second law of motion states that the momentum variation rate is equal to the applied forces [89]. Therefore, the conservation of momentum for the fluid flow in the cartesian form is given by

$$\frac{\partial}{\partial t}\left(\rho_f u_j\right) + \frac{\partial}{\partial x_j}\left(\rho_f u_i u_j\right) = -\frac{\partial p}{\partial x_i} + \frac{\partial}{\partial x_j}\left(\tau_{ij} - \rho_f u_i' u_j'\right) \tag{3.2}$$

where p is the static pressure, the terms $\rho_f u_i' u_j'$ are known as the Reynold stresses, and τ_{ij} is the stress tensor expressed as

$$\tau_{ij} = \mu_f \left(\frac{\partial u_i}{\partial x_j} + \frac{\partial u_j}{\partial x_i}\right) - \frac{2}{3}\mu_f \left(\frac{\partial u_k}{\partial x_k}\right)\delta_{ij} \tag{3.3}$$

where μ_f is the molecular viscosity and δ_{ij} is the Kronecker delta function defined in Eq. (3.4) [89, 90].

$$\delta_{ij} = \begin{Bmatrix} 1 & i = j \\ 0 & i \neq j \end{Bmatrix} \tag{3.4}$$

The conservation of energy for heat within the system and its boundaries is defined using [88, 91]

$$\frac{\partial}{\partial t}\left(c_{p,f}\rho_f T_f\right) + \frac{\partial}{\partial x_j}\left(c_{p,f}\rho_f u_j T_f\right) = -\frac{\partial}{\partial x_j}\left(q_j''\right) \tag{3.5a}$$

$$q_j'' = c_{p,f}\rho_f\left(-\alpha_f \frac{\partial T_f}{\partial x_j} + T_f{}'u_j'\right) \tag{3.5b}$$

$$\rho c_{p,s}\frac{\partial T_s}{\partial t} = k_s \frac{\partial^2 T_s}{\partial x_i^2} + S_c \tag{3.5c}$$

where Eqs. (3.5a and 3.5b) are for the fluid and Eq. (3.5c) is for heat conduction throughout the battery cell with an energy source term, S_c. $c_{p,f}$ is the specific heat capacity of the fluid, T_f is the fluid temperature, α_f is the fluid thermal diffusivity defined as the ratio of thermal conductivity and the volumetric heat capacity. ρ_s is the density of the solid, $c_{p,s}$ is the solid specific heat capacity, T_s is the solid temperature, and k_s is the thermal conductivity of the solid.

3.2 *Numerical schemes*

The RANS approach to turbulence requires the Reynold stresses in Eq. (3.2) to be modelled appropriately for closure. The most common method of modelling employs the Boussinesq approximation [97] which relates the Reynolds stresses to the mean velocity gradients as shown in Eq. (3.6),

$$-\rho_f u_i' u_j' = \mu_t\left(\frac{\partial u_i}{\partial x_j} + \frac{\partial u_j}{\partial x_i}\right) - \frac{2}{3}\left(\rho k + \mu_t \frac{\partial u_k}{\partial x_k}\right)\delta_{ij} \tag{3.6}$$

where the Kronecker delta function, δ_{ij}, is defined in Eq. (3.4). The turbulent eddy viscosity, μ_t, is computed using the following relation.

$$\mu_t = \rho C_\mu \frac{k^2}{\epsilon} \tag{3.7a}$$

where C_μ is found using Eq. (3.7b).

$$C_\mu = \frac{1}{A_0 + A_s \frac{kU^*}{\epsilon}} \tag{3.7b}$$

where the values of U^*, A_0, A_s and all other default values for the realisable $k - \epsilon$ turbulence model are given in [95, 96].

The realisable $k - \epsilon$ model is applied to the turbulence model in this work. This model builds on the standard $k - \epsilon$ model proposed by Launder and Spalding [93] in 1974. The new model contains a new formulation for the turbulent viscosity, k, and the dissipation rate, ϵ. Unlike the standard model, the realisable model satisfies certain mathematical constraints on the Reynolds stresses. The realisable model can also provide superior performance for boundary layers, separation, and recirculation [94, 95]. As stated in refs. [95, 96], the turbulence model transport equations are

$$\frac{\partial}{\partial t}(\rho_f k) + \frac{\partial}{\partial x_j}(\rho_f k u_j) = \frac{\partial}{\partial x_j}\left[\left(\mu_f + \frac{\mu_t}{\sigma_k}\right)\frac{\partial k}{\partial x_j}\right] + G_k + G_b - \rho_f \epsilon - Y_M \tag{3.8a}$$

$$\begin{aligned}\frac{\partial}{\partial t}(\rho_f \epsilon) + \frac{\partial}{\partial x_j}(\rho_f \epsilon u_j) \\ = \frac{\partial}{\partial x_j}\left[\left(\mu_f + \frac{\mu_t}{\sigma_\epsilon}\right)\frac{\partial \epsilon}{\partial x_j}\right] + \rho_f C_1 S_\epsilon - \rho_f C_2 \frac{\epsilon^2}{k + \sqrt{\nu_f \epsilon}} \\ + C_{1\epsilon}\frac{\epsilon}{k} C_{3\epsilon} G_b\end{aligned} \tag{3.8b}$$

where C_1 is defined by

$$C_1 = max\left[0.43, \frac{\eta}{\eta + 5}\right], \qquad \eta = S\frac{k}{\epsilon}, \qquad S = \sqrt{2S_{ij}S_{ij}} \tag{3.8c}$$

σ_k and σ_ϵ are the turbulent Prandtl numbers for k and ϵ, respectively. G_k is the turbulent kinetic energy generation due to mean velocity, G_b is the turbulent kinetic energy generation due to buoyancy, Y_M is the fluctuating dilatation in compressible turbulence. $C_{1\epsilon}$, C_2, and $C_{3\epsilon}$ are constants.

Furthermore, depending on the fluid type, different fluid models are used. As previously stated, the idea gas model is used when the coolant fluid is air, whereas the constant density is applied for liquids (like water). The ideal gas model uses the ideal gas law to express density as a function of temperature. However, as the name suggests, the constant density model assumes no change in the fluid density irrespective of temperature and pressure.

$$\rho_f = \frac{p}{RT_f} \tag{3.9a}$$

$$\rho_f = constant \tag{3.9b}$$

where p is the pressure and R is the universal gas constant. The Reynolds number based on the battery cell diameter, D, is expressed using

$$Re = \frac{u_f \rho_f D}{\mu_f} \tag{3.10}$$

The Nusselt number, based on Newton's law of cooling, is obtained using

$$q'' = h\left(T_f - T_{f,ref}\right) \tag{3.11a}$$

$$Nu = \frac{q''D}{k_f\left(T_f - T_{f,ref}\right)} \tag{3.11b}$$

where q'' is the heat flux at the surface of the battery cell and $T_{f,ref}$ is the reference fluid temperature. Further, the importance of free convection (natural convection) is tested using the Richardson number (Ri) as defined in Eq. (3.12a), which describes the ratio of natural convection to forced convection. If the value of Ri is very low ($Ri < 0.1$), forced convection would dominate heat transfer, thus, natural convection can be ignored [92].

$$Ri = \frac{Gr}{Re^2} \tag{3.12a}$$

$$Gr = \frac{g\beta\left(T_{surf} - t_{f,ref}\right)D^3}{\nu^2} \tag{3.12b}$$

where Gr is the Grashof number, g is gravity, β is the coefficient of volume expansion, T_{surf} is the temperature at the surface, and ν is the kinematic viscosity.

3.3 *Discretisation schemes*

The spatial and energy derivatives are discretised using the second-order upwind scheme with a constant spatial step Δx as stated in Eq. (3.13).

$$\frac{\partial u^-}{\partial x} = \frac{3u_i^n - 4u_{i-1}^n + u_{i-2}^n}{2\Delta x} + O((\Delta x)^2) \tag{3.13a}$$

$$\frac{\partial u^+}{\partial x} = \frac{-u_{i+2}^n + 4u_{i+1}^n - 3u_i^n}{2\Delta x} + O((\Delta x)^2) \tag{3.13b}$$

Eq. (3.13a) and Eq. (3.13b) are for the backward and forward differences, respectively. Most commercial CFD packages compute the second-order upwind scheme using the following expression [98–100].

$$\phi_{f,SOU} = \phi + \nabla\phi \cdot \vec{r} \tag{3.14}$$

In which $\phi_{f,SOU}$ is the second-order upwind of the face value, ϕ is the cell-centred value, $\nabla\phi$ is the cell-centred gradient in the upstream cell, and $\vec{r}$ is the displacement vector from the upstream cell centroid to the face centroid. A visual representation of the second-order upwind scheme is shown in Figure 3-1. WW, W, E, and EE are the west-west, west, east, and east-east directions, respectively.

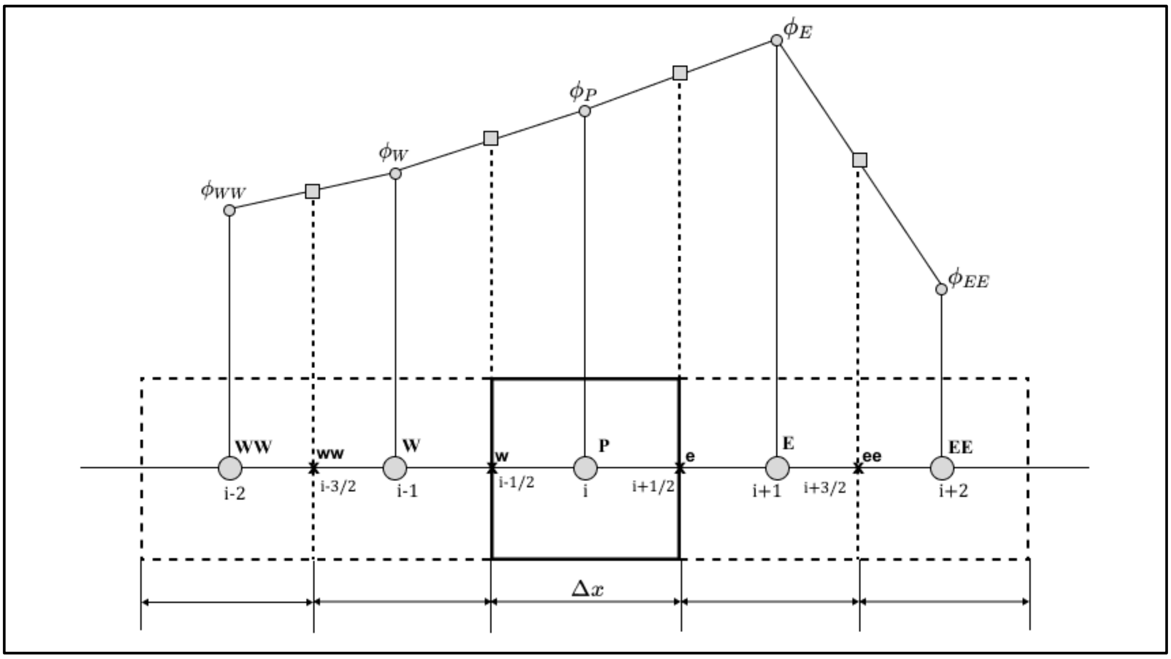

Figure 3-1 – Visual representation of the second-order upwind scheme [101].

The governing equations for transient simulations must be discretised in both space and time. Therefore, the temporal discretisation is achieved using the Courant-Friedrichs-Lewy (CFL) condition [102].

$$CFL = \frac{u\Delta t}{\Delta x} \leq 1 \tag{3.15}$$

where u is the inlet flow velocity, Δt is the user defined timestep, and Δx is the cell-to-cell length interval. The target CFL number throughout this thesis was 0.9 to achieve stability and reduce computational load.

3.4 *Pressure solver*

The pressure and velocity coupling is resolved using the PIMPLE pressure correction algorithm. The PIMPLE method combines the PISO (Pressure Implicit with Splitting of Operator) and the SIMPLE (Semi-Implicit Method for Pressure-Linked Equations) algorithms. Spalding first introduced the SIMPLE method in the 1970s as a numerical procedure to solve the Navier-Stokes equations for steady-state cases [103], whereas the PISO method was proposed by Issa in 1986 [104] for solving unsteady compressible flows. All of these algorithms use an iterative approach to solve the pressure and velocity fields. However, the PIMPLE algorithm obtains far better stability over PISO, especially when the nature of the solution is inherently unstable. The PIMPLE method works by iteratively solving the system of equations numerous times (set by the user) before moving on to the next timestep, which allows the numerical solution to achieve better stability [104, 105]. A simple flow chart of the PIMPLE algorithm is shown in Figure 3-2.

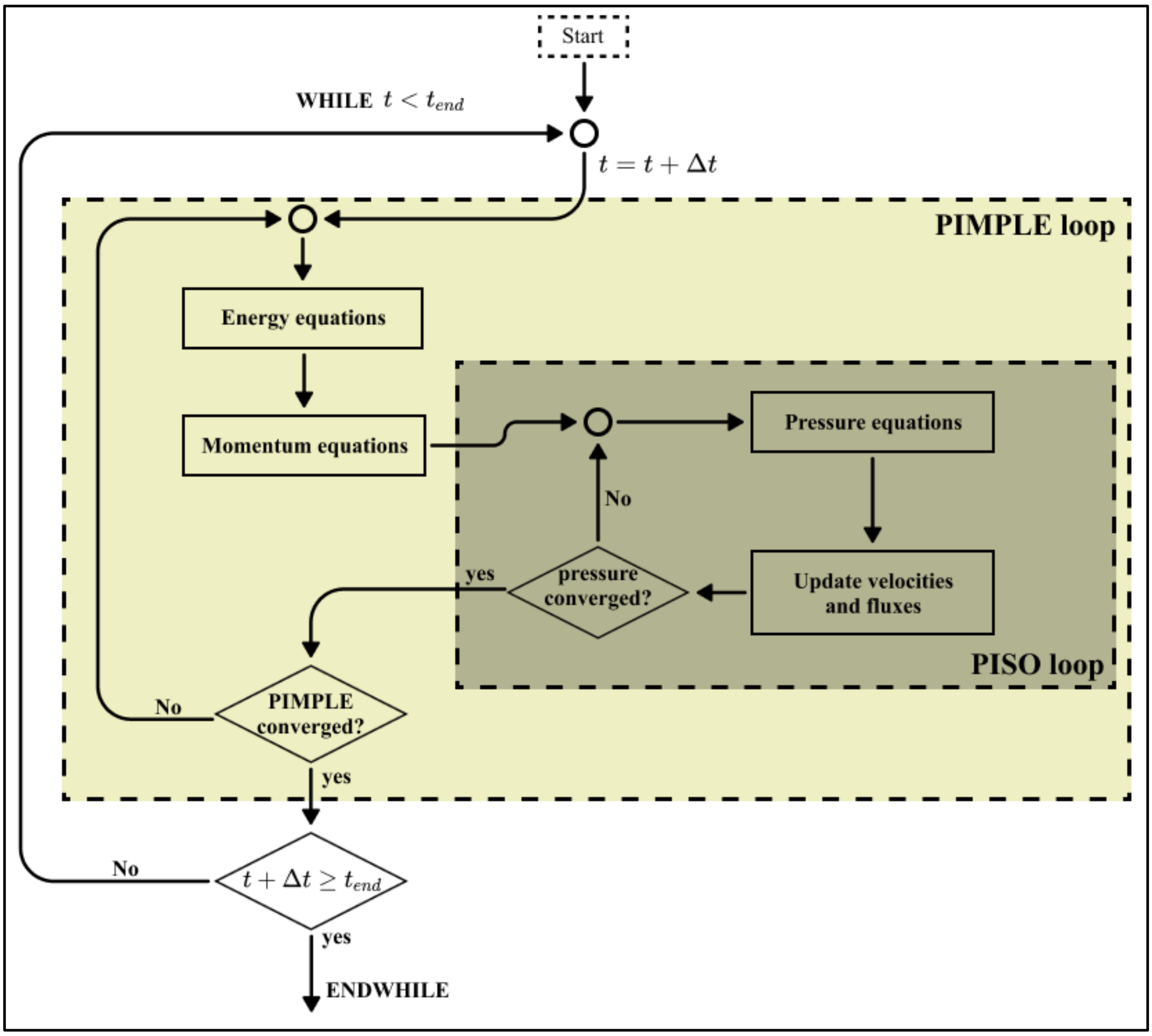

Figure 3-2 – Simplified flow chart of the PIMPLE algorithm.

Chapter 4. Surface heat flux modulation of battery cells in a Li-ion battery module

Comprehensive BTMSs capable of enhanced system efficiency and safety by predicting the thermal behaviour of the battery cells and adjusting the cooling system accordingly are a concerning issue for emerging electric vehicles. Not only is the ability to predict the battery cell's behaviour hard to detect, but the complexity and highly transient nature of an EV also make the investigation intractable. Thus, understanding the conditions under which the thermal system dynamics can be predicted is of utmost concern.

There are very few scenarios during which the battery cells of an EV will provide a constant load. Instead, the highly unpredictable nature of a driver continuously accelerating and decelerating the vehicle would lead to the battery cells being under a dynamic load. Therefore, this chapter presents the numerical analysis of a Li-ion battery module under unsteady loads imposed on the surface heat flux of the battery cells. The battery cells are modelled using real cell dimensions based on literature. Three different coolant fluids are used in this study: the choices being air, water, and nanofluids. A systematic approach to calculating the transfer functions is provided. The numerical results are compared against existing correlations and experimental data for validation. The Nusselt number output of the battery cells is analysed in the time and frequency domains before a rigorous approach of assessing the system linearity is discussed.

4.1 *Model configuration and assumptions*

The general configuration of the battery module used during this study was taken from Ref. [66]. The sketch of a typical battery module manufactured using the series-parallel approach, the simulated model, and a two-dimensional schematic of a single cell section are shown in Figures 4-1a, b, and c, respectively. The model uses a staggered cell arrangement with six primary cells. This number of cells was chosen based on previous studies, see Refs. [33, 40, 54]. Simulating an entire battery module would be computationally expensive and laborious; thus, only a section was simulated, outlined in green in Figure 4.1a. The battery cells have a radius, R, of 20mm [38, 40, 66]. The single cell section, shown in Figure 4.1c, has a height, H, of 50mm, length, L, of 100mm and depth of 100mm [66]. The proceeding analysis contains the following assumptions:

- The flow is thermally and hydrodynamically fully developed.

- The flow is fully turbulent with a steady inlet velocity.
- When air is used, the coolant fluid is treated as an ideal gas. Whereas for cases with water and nanofluids, the coolant fluid is simulated using a constant density model.
- Gravitational effects are ignored.
- The nanofluid is modelled as a single-phase liquid.

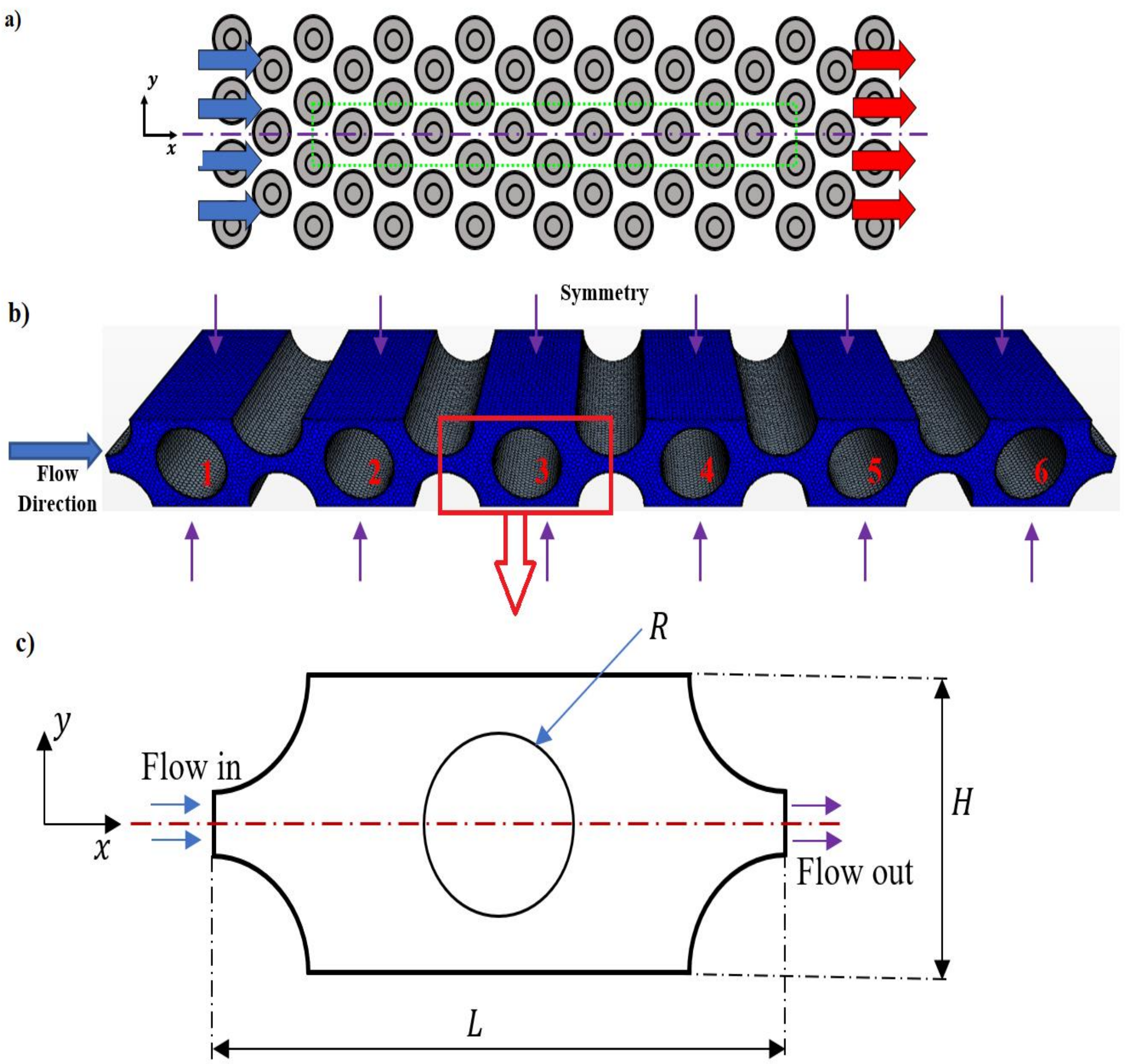

Figure 4-1 – Complete model. a) General sketch of a battery module with the simulated model outlined in green, b) simulated model, c) single cell section 2D schematic.

Additionally, the unsteady thermal heat flux was applied to the surface of each battery cell once the model achieved steady-state conditions. In justifying this approach, it is noted that heat generation in the battery cell can only be removed from the system once it reaches the surface of the battery cell [106, 107]. Consequently, the heat loss from each battery cell was modelled by a surface heat flux per Refs. [108–110]. The definition of each variable used in this or the following sections, along with the corresponding units, can be found in the nomenclature.

The boundary conditions applied to the numerical model include a no-slip boundary on the external surface of each battery cell. Further, the front, back, top, and bottom walls all have symmetry conditions since the battery cells can be packed in the y and z-directions. The ambient fluid temperature was set to 300K, and a pressure outlet condition was applied to the outlet. A general sketch of the numerical model with some of the boundary conditions can be seen in Figure 4-2.

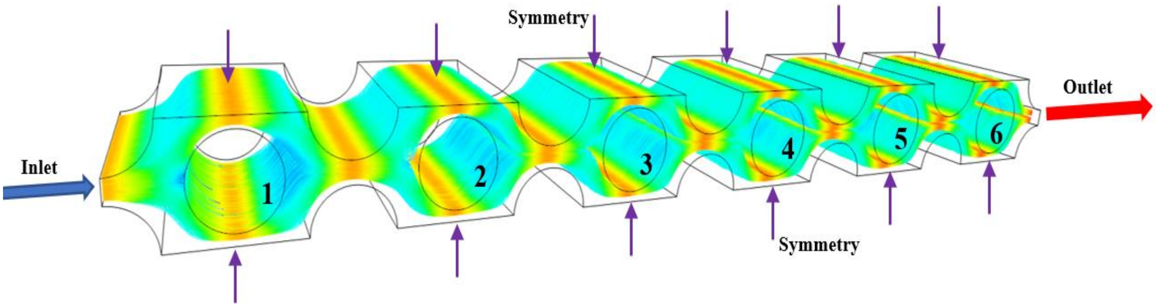

Figure 4-2 – General sketch of the numerical model.

The thermal boundary of each battery cell was modelled as a constant heat flux of 6500W/m^2 under steady-state conditions. This value for the heat flux was chosen based on the current model geometry, the 85kW battery specifications of the Tesla Model S [111], and an average battery cell efficiency of 85% [112]. An inlet velocity of 30m/s (Re = 75,000) was chosen for the air cases. It should be noted that the expected air velocity of a vehicle being driven on outer city roads is 30m/s. Further, this value also corresponds with literature on BTMS, see Ref. [113]. Due to its poor thermal conductivity and capacity, higher flow velocities are mandatory to sufficiently cool down battery cells for optimal operation when using air as the coolant fluid. Furthermore, the Reynolds number for water and nanofluids was chosen to be 2,300, corresponding with previous studies [114–116]. The values of Re for the three coolant fluids are kept constant throughout the study. As a Re of 75,000, the Richardson number was 1.05×10^{-4}, according to Eq. (3.12a). Therefore, gravitational effects were ignored since the calculated Ri is much lower than 0.1.

Once the model reached steady-state conditions, the battery cells' surface heat flux was modulated with time by superimposing a sinusoid with varying frequencies and amplitudes shown in Eq. (4.1),

$$q''(t) = q_s''(1 + a \cdot sin(2\pi \cdot f \cdot t)) \tag{4.1}$$

where $q''(t)$ is the heat flux at time t, q''_s is the steady-state heat flux (6500W/m^2), a is the amplitude of disturbance and is regarded as the modulation/excitation amplitude from henceforth, and f is the modulation frequency. Moreover, the frequency is non-dimensionalised using the Strouhal number, St, as stated in Eq. (4.2a) and is then normalised using Eq. (4.2b).

$$St = \frac{fD}{u} \tag{4.2a}$$

$$St = \frac{St}{MAX(St)} \tag{4.2b}$$

The changes of the single-phase nanofluids' dynamic viscosity, μ, and thermal conductivity, k, were calculated using the relations stated in Eq. (4.3a) and (4.3b) respectively. It is noted that the nanofluid mixture is comprised of Aluminium-oxide, Al_2O_3, and water. Eq. (4.3a) and (4.3b) are well-established models developed by Brinkman and Maxwell-Garnetts, respectively [117, 118],

$$\frac{\mu_{nf}}{\mu_f} = \frac{1}{(1-\phi)^{2.5}} \tag{4.3a}$$

$$\frac{k_{nf}}{k_f} = \frac{k_s + 2k_f - 2\phi\left(k_f - k_s\right)}{k_s + 2k_f + \phi\left(k_f - k_s\right)} \tag{4.3b}$$

where ϕ is the concentration of nanoparticles. During the nanofluid cases, nanoparticle concentrations of 2.5% and 5.0% were used. It is well-regarded that the nanoparticle concentration directly impacts their dispersion [119]. Nanoparticle concentrations higher than 5% begin to disrupt their dispersion due to higher surface tension. Eventually, the dispersion of the nanoparticles completely collapses, and the nanofluid becomes a base fluid with clumps of nanoparticles [120]. Therefore, a maximum nanoparticle concentration of 5.0% was chosen. The thermophysical properties of the three coolants used throughout this study are given in Table 4-1, with all properties evaluated at a temperature of 300K.

Table 4-1 – Thermophysical properties.

Material Type	Density, ρ $(\mathrm{kg/m^3})$	Dynamic viscoity, μ (m^2/s)	Thermal conductivity, k $(\mathrm{W/mK})$
Air	1.1614	1.846e-05	0.02624
Water	996.53	8.65e-04	0.597834
Aluminium Oxide (Al_2O_3)	–	–	30.0

A parametric study was subsequently conducted, where the coolant fluid, modulation amplitude, and frequency were systematically varied. The battery cell surface heat flux was modulated at low frequencies $(f \leq 2\ Hz)$ since thermofluid systems often respond to low frequencies only [121, 122].

The numerical analysis was conducted using a finite-volume-based CFD software called StarCCM+ v14.02-R8. The CFD software employed an unsteady, three-dimensional, turbulent flow solver coupled with the energy equation. The realisable $k - \epsilon$ turbulence model was utilised to simulate the flow field around the battery cells. An implicit unsteady model was also used. Further, as previously mentioned, the ideal gas and constant density models were used for air and water/nanofluid cases, respectively. The timestep was set to be three orders of magnitude smaller than the physical time-scale to model the vortex shedding precisely. The second-order discretisation scheme was applied to every model for enhanced accuracy. Due to the high-mesh density and complexity of the model, the computational models were run in a high-performance computing (HPC) unit using a single compute node of the Intel Xeon 4830 (24 cores). The numerical data was then post-processed in MATLAB 2019b.

4.2 *Calculation of Transfer functions*

Throughout this study, the heat transfer data produced by the numerical simulations is analysed by translating the data from the time domain into the frequency domain. This was done using MATLAB's inbuilt Fast Fourier Transform functions. However, before applying FFT, the Nusselt number was normalised using Eq. (4.4).

$$Norm\big(Nu(t)\big) = \frac{Nu(t)}{\overline{Nu}} \tag{4.4}$$

where $Nu(t)$ is the Nusselt number at time t and $\overline{Nu}$ is the time-averaged Nusselt number. Transfer functions were utilised to predict the dynamic thermal response of battery cells to perturbations in their surface heat flux. However, this would imply that the thermal characteristics of the dynamic system under investigation are linear. The amplitude of the transfer function was calculated using the following relation,

$$a(f) = \left| Norm\big(Nu(t)\big)_i \right| \tag{4.5}$$

where the subscript i refers to the battery cell. Further, cross-correlation was used to measure the time delay between the input signal and output response [122]. The non-dimensionalised time delay is defined in Eq. (4.6),

$$ndd = \frac{td}{dl_i/u} \tag{4.6}$$

where ndd is the non-dimensionalised delay, td is the cross-correlation time delay, dl_i is the length from the inlet to the battery cell, and u is the inlet velocity. Additionally, the cross-correlation time delay was used to calculate the phase of the transfer function in radians, as defined in Eq. (4.7).

$$phase = 2\pi f * td \tag{4.7}$$

However, throughout this study, the non-dimensionalised delay was used to represent the phase of the transfer function.

4.3 *Grid independency study*

Figure 4-1b shows the polyhedral staggered mesh used to capture the fluid flow and heat transfer in the model. The boundary was modelled using twelve prism layers around each battery cell to augment model accuracy. Multiple test cases were carried out at different mesh cell sizes to determine the mesh grid at which the highest accuracy and lowest computational costs could be achieved. The outcome of the results is shown in Table 4-2. Here, the cell size refers to the master control of all other values, such as surface cell size, volume cell size, and prism layer thickness. The grid independence was achieved once the Nu of each cell fell within a variation band of one percent. All tests were carried out at a constant Re of 5,100. From Table 4-2, as the cell size is decreased, the mesh density (the number of cells) increases, and the resultant maximum change of Nu converges. The model accuracy and computational requirement were balanced by selecting a cell size of 0.0025, which is kept constant throughout this study.

Table 4-2 – Grid Independency.

Test case	Cell size (m)	Number of cells	Maximum change in Nu (%)
1	0.01	116,051	----
2	0.009	131,032	8.2
3	0.008	167,373	6.5
4	0.007	188,558	6.2
5	0.006	199,886	5.9
6	0.005	211,293	7.2
7	0.004	232,619	4.1
8	0.003	277,973	1.0
9	0.002	637,396	0.4
10	0.001	3,081,209	0.1

4.4 *Validation study*

The numerical model was validated by comparing it against existing numerical and experimental data. First, the model configuration was changed so that the flow occurs over a single cell rather than a bundle of cells. The comparison of the results from the simulated model and the numerical/experimental data are shown in Tables 4-3 to 4-5.

Table 4-3 – Comparison of the numerical simulations with correlations and experimental data from literature – Single cylinder. $\boldsymbol{Fluid = Air}$.

Reynolds Number	50	125	3,900	4,950
Simulated Nusselt Number	3.67097	5.67048	38.19765	43.6583
Correlations				
Churchill and Bernstein [123]	3.74082	5.68934	32.44680	36.55737
Error (%)	1.9	0.33	15.06	16.26
Experimental Data				
Yogini Patel [124] C_d			0.93±0.005	
Simulated C_d (Error)			0.917 (1.4%)	

From Table 4-3, at low values of Re (laminar region), the simulated Nusselt number is in excellent agreement with the values obtained from the Churchill and Bernstein [123] empirical correlation. As the value of Re increases (turbulent region), the errors also increase, with the highest error being 16.26% at a Re of 4,950. Nevertheless, it should be noted that this error is still within the error limits of the correlations, which can reach over 20% [123]. Further, the fluid flow characteristics were compared to experimental data at a Re of 3,900. The simulated drag coefficient, C_d, was found to be 0.917, whereas the experimental C_d by Patel was 0.93, leading to an error of 1.4%.

Table 4-4 – Comparison of the numerical simulations with the correlations from literature– Single cylinder. $\boldsymbol{Fluid = Water}$.

Reynolds Number	50	235	10,700	18,900	26,500
Simulated Nusselt Number	4.8849	11.025	84.2621	117.016	148.494
Hilpert [125]	5.2459	10.8139	73.8475	105.1833	129.495
Error (%)	7.39	1.91	12.36	10.11	12.79
Churchill and Bernstein [123]	5.362	11.3654	81.450	112.5657	136.996
Error (%)	9.77	3.09	3.34	3.80	7.74

From Table 4-4, comparing the simulated Nu of the water simulations against correlations leads to a maximum error of 12.79% at a Re of 26,500 and the lowest error of 1.91% at a Re of 235. Comparing the simulated results against the Churchill and Bernstein correlation leads to all errors being less than 10%. Further, the water validation cases were repeated for different Re values and compared against experimental data by Whitaker [126]. At all values of Re, the error is less than five percent, as shown in Table 4-5, where the highest error of 4.7% is at a Re of 9,700 (turbulent region) and the lowest error of 1.68% at a Re of 18 (laminar region).

Table 4-5 – Comparison of the numerical simulations with the experimental data from literature – Single cylinder. $\boldsymbol{Fluid = Water}$.

Reynolds Number	18	86	103	9,700	12,500
Simulated Nusselt Number	4.8849	11.025	12.225	148.494	174.25
Stephen Whitaker [126]	4.9667	11.4174	12.5997	155.4665	179.3675
Error (%)	1.68	3.56	3.06	4.70	2.94

The heat transfer for airflow across a bundle of cells was compared against the Grimson [127] empirical correlation. At an inlet velocity of 30m/s, the simulated model produced an average Nusselt number of 215.056, whereas the previously mentioned correlation resulted in an average Nu of 233.053, leading to an error of 8.4%.

The excellent agreement between the numerical results, empirical correlations, and experimental data for both the air and water cases confirms the validity of the numerical analysis presented in this study.

4.5 *Post processing*

A flow chart illustrating the steps taken during the numerical analysis is shown in Figure 4-3. Once the numerical simulations were complete, their data was exported for post-processing as text files. During post-processing, the nonlinearity of the outputs was calculated using FFT and phase portraits. If the nonlinearity measure was found to be less than 10%, transfer function analysis can be conducted [122]. These methods are further discussed in the following sections. The developed post-processing tools were validated against synthetic data to ensure the robustness of the analysis.

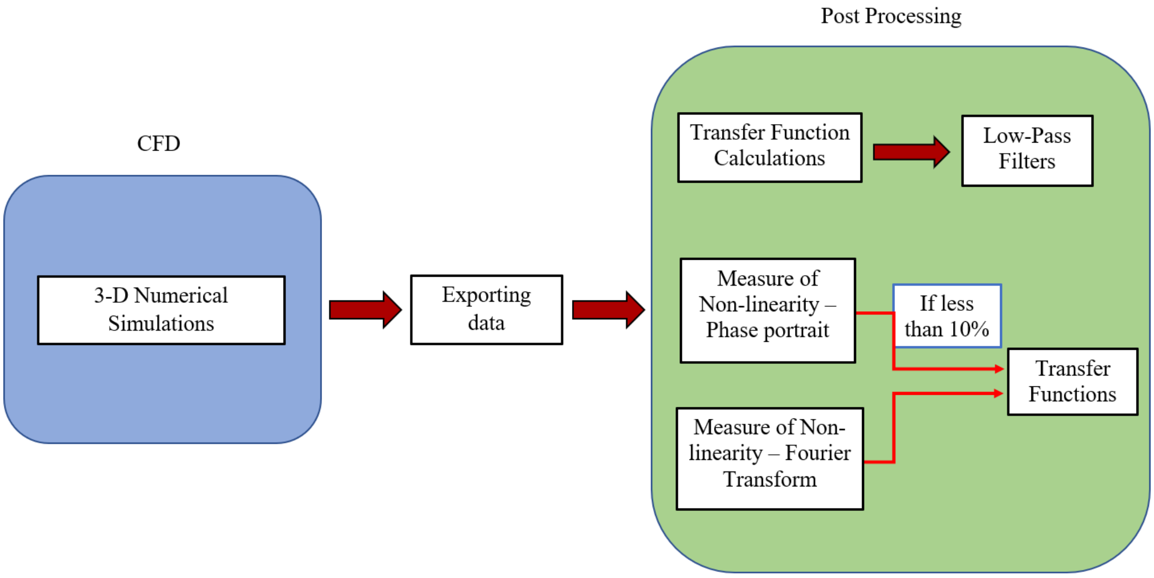

Figure 4-3 – Post processing flow chart.

4.6 *Results and discussion*

In this section, the battery cells are excited by sinusoidal disturbances imposed on the surface heat flux and the resultant dynamic response of analysed (see details in sections 4.1 and 4.2). It should be noted that Fourier transforms can be used to decompose any arbitrary temporal disturbance into a series of sinusoids [128]. Thus, understanding the system response to sinusoidal disturbances is paramount for predicting the battery cells' behaviour to all temporal fluctuations imposed on the battery heat release. However, for this to hold, the system must be linear, so it is essential to examine the deviation of linearity of the thermal system. This section focuses on addressing these two issues.

The steady-state values of the heat convection coefficient, h, for the different coolant fluids used throughout this study are shown in Figure 4-4. As expected, the poor thermal conductivity of air leads to shallow values of h, whereas water results in higher heat convection coefficients due to its superior thermal conductivity. As proven by numerous studies, adding nanoparticles to a base fluid enhances the fluid's ability to transfer heat, leading to higher values of heat convection coefficients, which is amplified by increasing the concentration of nanoparticles, as shown in Figure 4-4.

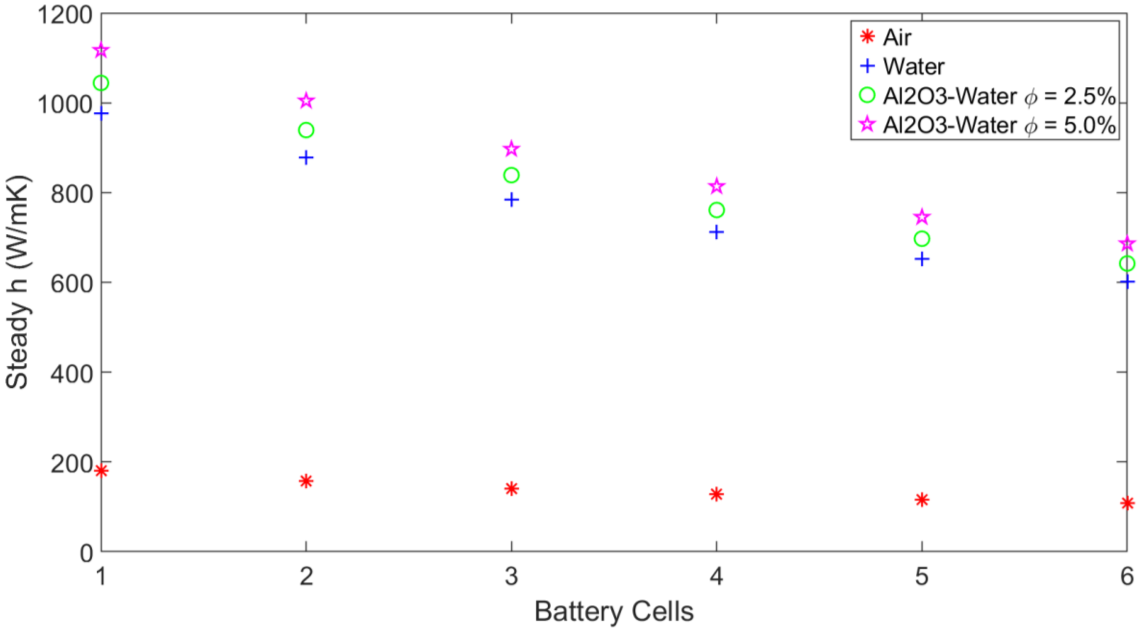

Figure 4-4 – Heat transfer coefficient, h, values for the different coolant fluids under steady-state conditions.

The spatiotemporal response of the fluid temperature to sinusoidal heat flux disturbances imposed on the surface of each battery cell is shown in Figure 4-5. The modulation amplitude and frequency for the case shown in Figure 4-5 are 30% and 1.00 Hz, respectively. This figure depicts a typical convective system in which the fluid temperature tends to approach that of the battery cell as it flows downstream. The temperature at the surface of the battery cells rises when the sinusoid reaches its peak value, which is evident by the cooling region near the inlet receding and the downstream temperature increasing. As the sinusoid continues and reaches 180°, the cooling region advances; however, it does not equally represent the temperature field shown at 0°. This dissimilarity is due to the forcing frequency being 1.00 Hz, which means that to process the sinusoidal change from 90° to 180°, only 0.25 seconds are utilised, which is insufficient time for the model to reset to its previous state completely. Moreover, as the sinusoid progresses to 270°, the cooling regions near the inlet gain further ground since the battery cells' surface temperature would be the lowest as this is the trough of the sinusoid. The decrease in temperature across the model allows the temperature field to reset as the sinusoid returns to its original position.

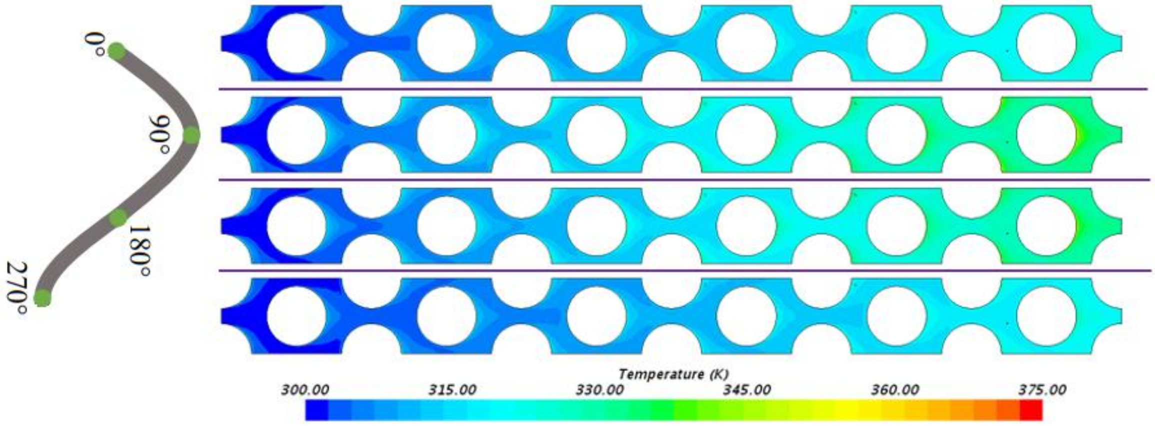

Figure 4-5 – Spatiotemporal evolution of the temperature field due to sinusoidal disturbance imposed on the battery cells' surface heat flux. $Fluid = Air$, $a = 30\%$, and $f = 1.00\ Hz$.

For brevity, figures for all eight frequencies are not shown. Instead, four frequencies are chosen – 0.25, 1.00, 1.50, and 2.00 Hz – to show the evolution of the FFT response as the forcing frequency is increased.

4.6.1 *Linear cases*

The temporal response of the normalised Nusselt number and the corresponding response in the frequency domain is shown in Figure 4-6. This figure corresponds to a case with air as the coolant fluid, a modulation amplitude of 10%, and a forcing frequency of 0.25 Hz. In Figure 4-6a, the Nusselt number of the three examined battery cells very closely represents a sinewave with an increase in amplitude for cells located further downstream. This increase is due to the increase in the fluid temperature as the coolant travels downstream, requiring a larger convective heat transfer coefficient to continue extracting heat flux produced on the surface of each battery cell. This phenomenon causes a more significant variation in Nu for downstream battery cells than those near the inlet, producing larger amplitudes. This behaviour is further confirmed in Figure 4-6b, which shows the spectral response of the time trace of Nu. The classical sign of a linear system is the equality of the response frequency and the excitation frequency [128–130]. Although the spectral response contains two spikes, the second is insignificant. Thus, the modelled battery module’s heat transfer is linear. A rigorous method of assessing the nonlinearity will be put forward in a later section.

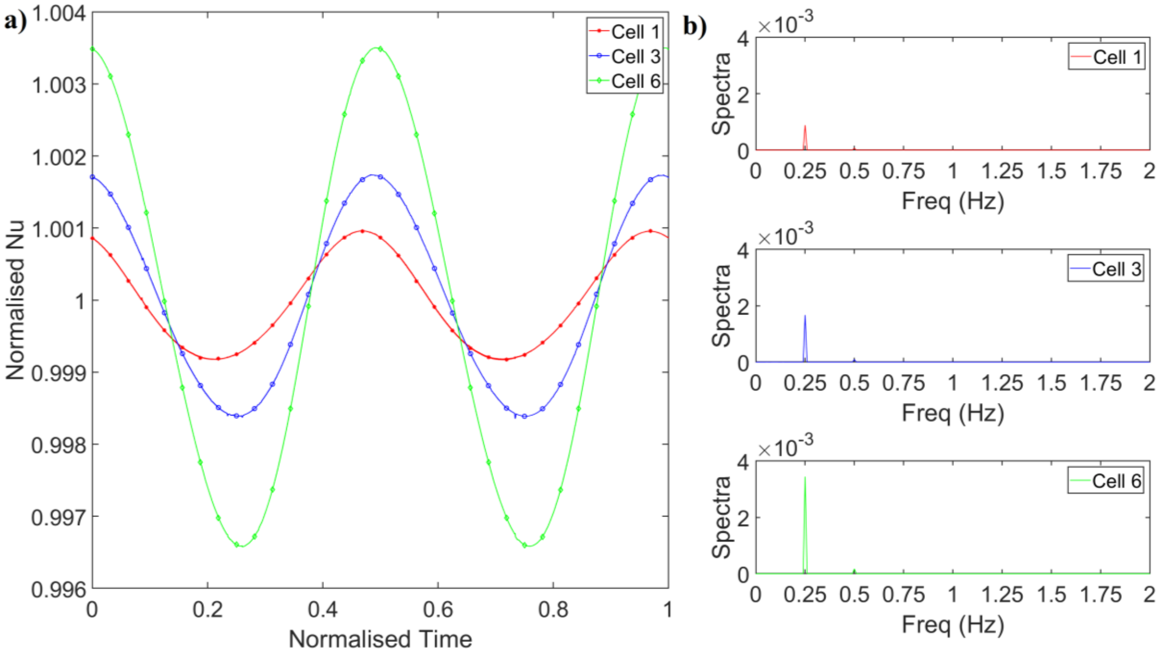

Figure 4-6 – a) Temporal evolution of Nu over battery cells’ 1, 3, and 6, b) Spectral response of Nu. $Fluid = Air$, $a = 10\%$, and $f = 0.25\ Hz$.

Increasing the forcing frequency from 0.25 Hz to 1.00 Hz while maintaining the same modulation amplitude and fluid type of 10% and air, respectively, the corresponding temporal evolution of Nu and spectral response is shown in Figure 4-7. Increasing the forcing frequency did not impact the shape of the Nu response or the number of spikes in the Fourier response. However, Nu's amplitude increased by as much as ten times. This increase can be attributed to the significant changes in the surface heat flux of the battery cells in a short period, leading to higher convective heat transfer coefficient values, which, consequently, increases the value of Nu. Figure 4-7 continues to show an equal value for the forcing frequency and the excitation frequency, thus making the system dynamics of this case linear. This is further supported by increasing the forcing frequency to 1.50 Hz and 2.00 Hz. The figures for the increase in the forcing frequency to 1.50 and 2.00 Hz can be seen in Figures 4-8 and 4-9, respectively. The response in these two figures also equals their respective forcing frequencies, making them linear.

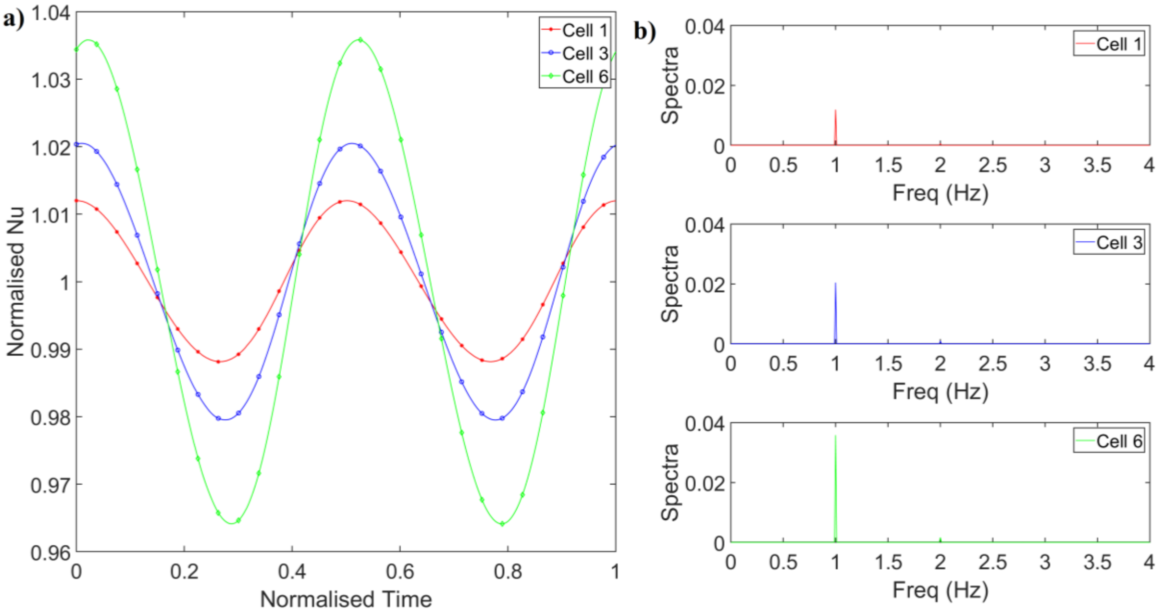

Figure 4-7 – a) Temporal evolution of Nu over battery cells' 1, 3, and 6, b) Spectral response of Nu. $Fluid = Air$, $a = 10\%$, and $f = 1.00\ Hz$.

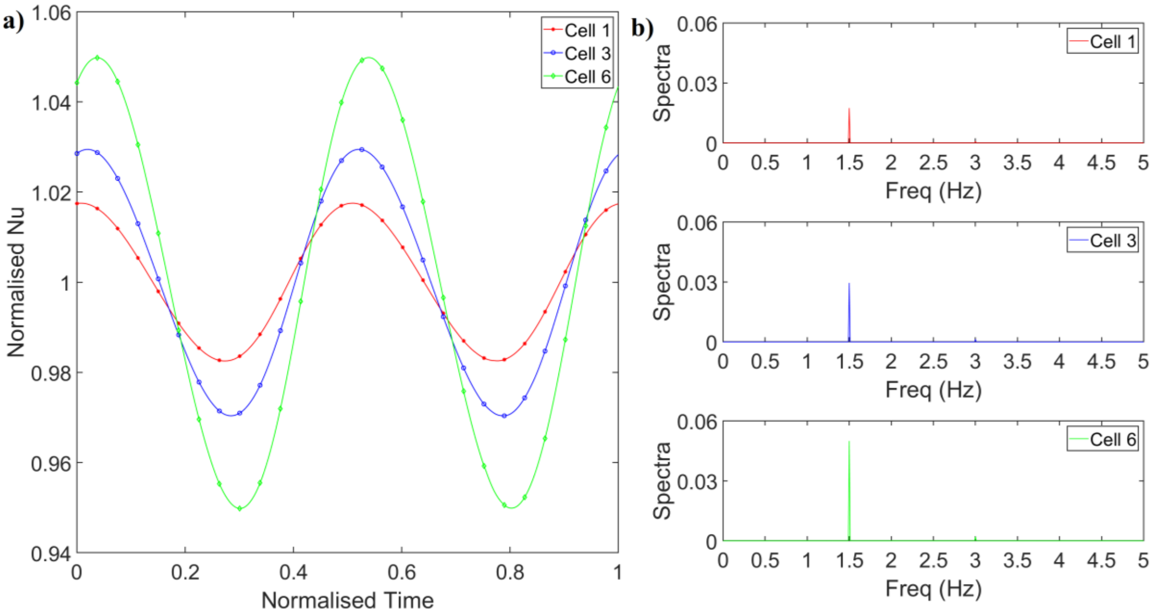

Figure 4-8 – a) Temporal evolution of Nu over battery cells' 1, 3, and 6, b) Spectral response of Nu. $Fluid = Air$, $a = 10\%$, and $f = 1.50\ Hz$.

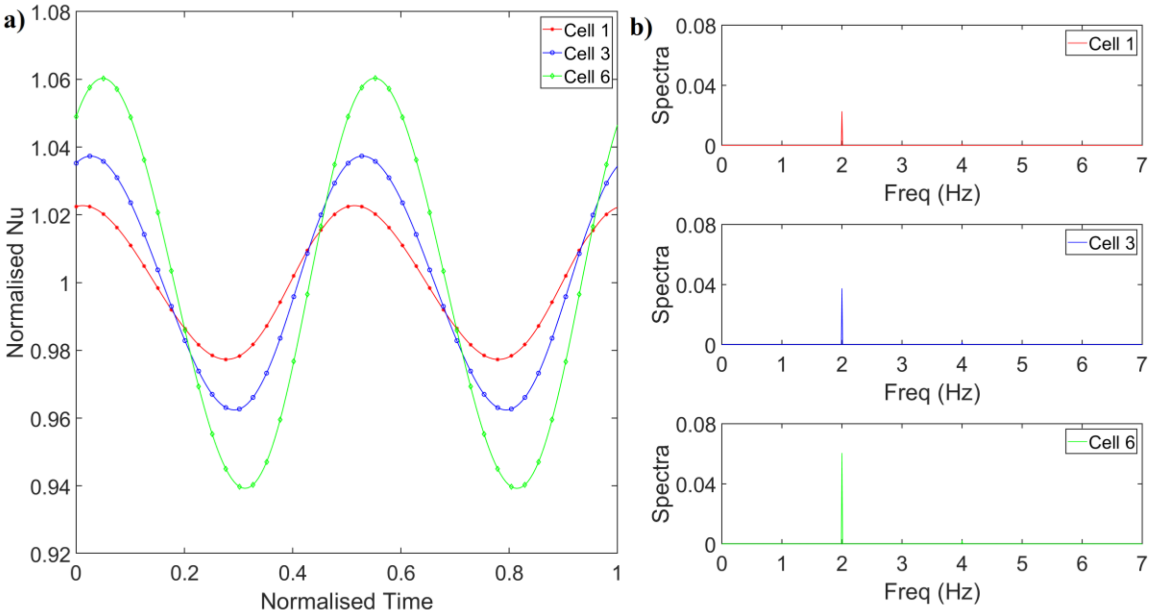

Figure 4-9 – a) Temporal evolution of Nu over battery cells' 1, 3, and 6, b) Spectral response of Nu. $Fluid = Air$, $a = 10\%$, and $f = 2.00\ Hz$.

Figure 4-10 shows the Nusselt number temporal and spectral response, where the coolant fluid is water, and the modulation amplitude and frequency are 10% and 0.25 Hz, respectively. The temporal responses shown in Figures 4-6a and 4-10a differ significantly due to the significant difference in the thermophysical properties of the two fluids. The general trend observed in Figures 4-6 and 4-10 is the increase in the Nu amplitude for cells located further downstream. Figure 4-5 showed that the average coolant fluid temperature increases as the coolant reaches the outlet, and the cells are set to lose a fixed heat flux value from each battery cell's surface. Therefore, the battery cells located downstream surrounded by the hotter fluid should feature larger Nu amplitudes fluctuations. The extent of this behaviour in the Nu amplitude is more significant in Figure 4-6 than in Figure 4-10. This can be attributed to the significant difference in the specific heat capacity of the two fluids. Unlike air, water can retain a far higher amount of heat energy before experiencing a temperature rise, resulting in a much more significant temperature increase in air. Unlike the temporal response from Figures 4-6 and 4-10, the spectra are quite similar, with a single prominent peak occurring at the forcing frequency and an insignificantly smaller second harmonic. Thus, as with the previous air cases, the water case can also be approximated as a dynamically linear system.

Increasing the forcing frequency for cases with water as the coolant produced similar results to those shown for air in Figures 4-7, 4-8, and 4-9. The only observable difference was the increase in the Nu amplitude and the FFT response. Thus, for the sake of brevity, the figures for cases with water, modulation amplitude of 10%, and forcing frequencies of 1.00, 1.50, and 2.00 Hz are not shown.

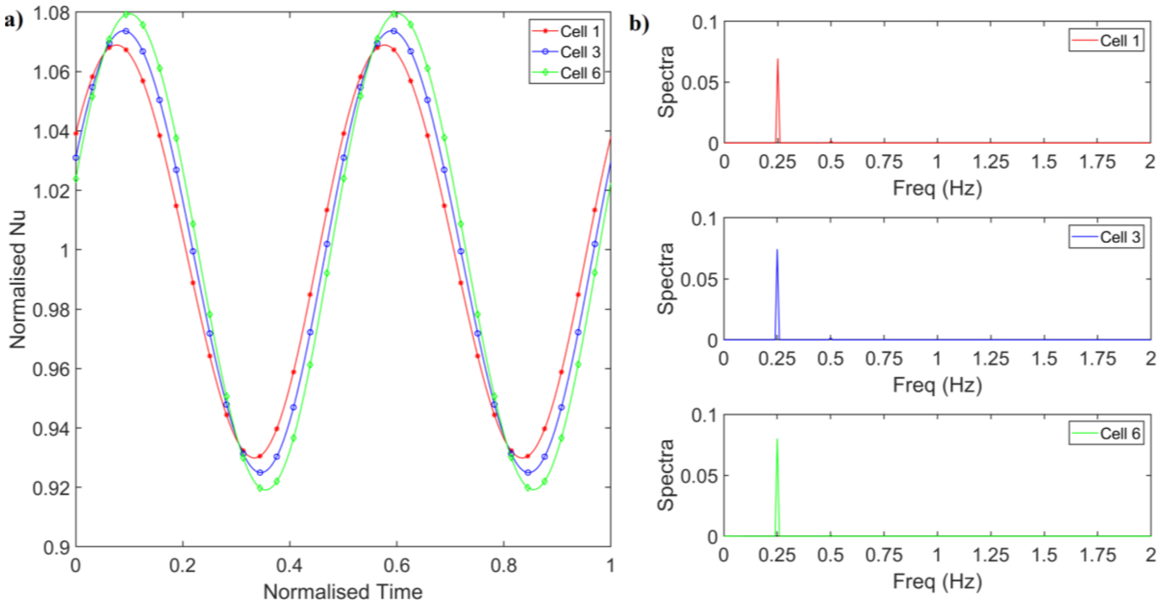

Figure 4-10 – a) Temporal evolution of Nu over battery cells' 1, 3, and 6, b) Spectral response of Nu. $Fluid = Water$, $a = 10\%$, and $f = 0.25\ Hz$.

Further, the temporal and spectral response of Nu, where the coolant fluid is Al_2O_3-Water nanofluid with a nanoparticle concentration of 2.5%, and the modulation amplitude is 10% with an excitation frequency of 0.25 Hz, is shown in Figure 4-11. The responses in this figure very closely represent those shown for water with the same modulation amplitude and frequency, as shown in Figure 4-10. Thus, this case can also be approximated as a linear dynamic system. Further increasing the nanoparticle concentration to 5.0% led to results similar to those shown in Figure 4-11, with the most significant change being an increase in the normalised Nu amplitude. Due to the similarity among the cases of water and Al_2O_3-Water nanofluids, no further nanofluid results are shown.

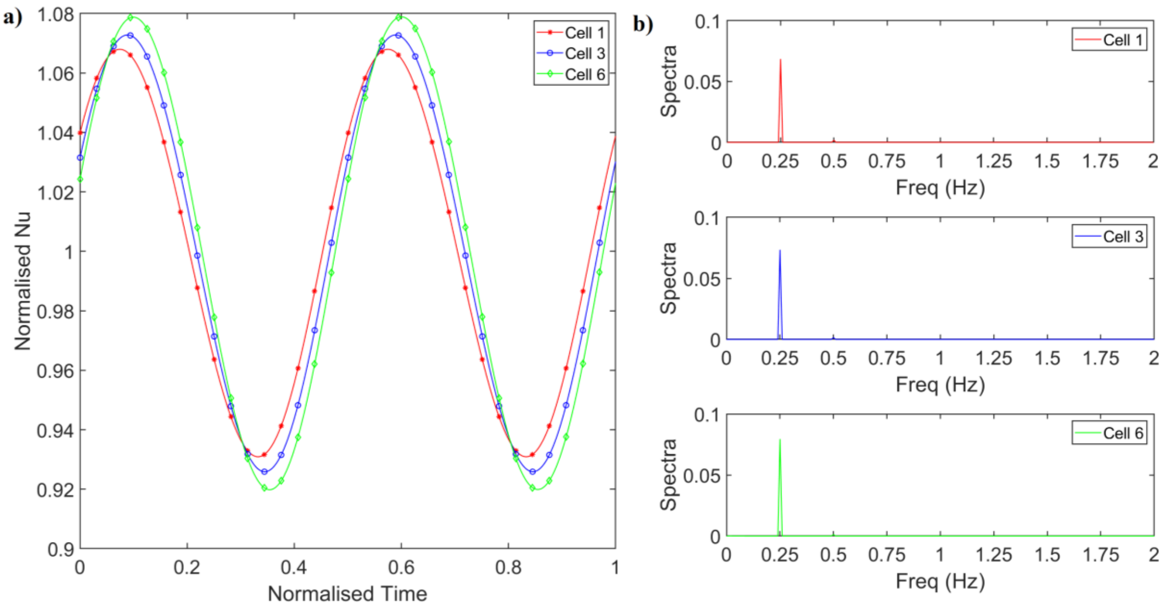

Figure 4-11 – a) Temporal evolution of Nu over battery cells' 1, 3, and 6, b) Spectral response of Nu. $Fluid = Al_2O_3 - Water$ $(\phi = 2.5\%)$, $a = 10\%$, and $f = 0.25\ Hz$.

Given information on the amplitude and phase of the dynamic response, a transfer function can be used to predict the dynamics of a linear system [128]. The classical concept of transfer functions is often used for linear systems, which are considered SISO (single input, single output). In this study, the surface heat flux imposed on the battery cell is considered the single input, and each battery cell's corresponding normalised Nu is a single output. Consequently, six transfer functions are produced – one for each primary battery cell in the battery module. The amplitude and the non-dimensional delay of the transfer functions were calculated using the method outlined in Section 4.2 for air and water and are presented in Figures 4-12 and 4-13, respectively.

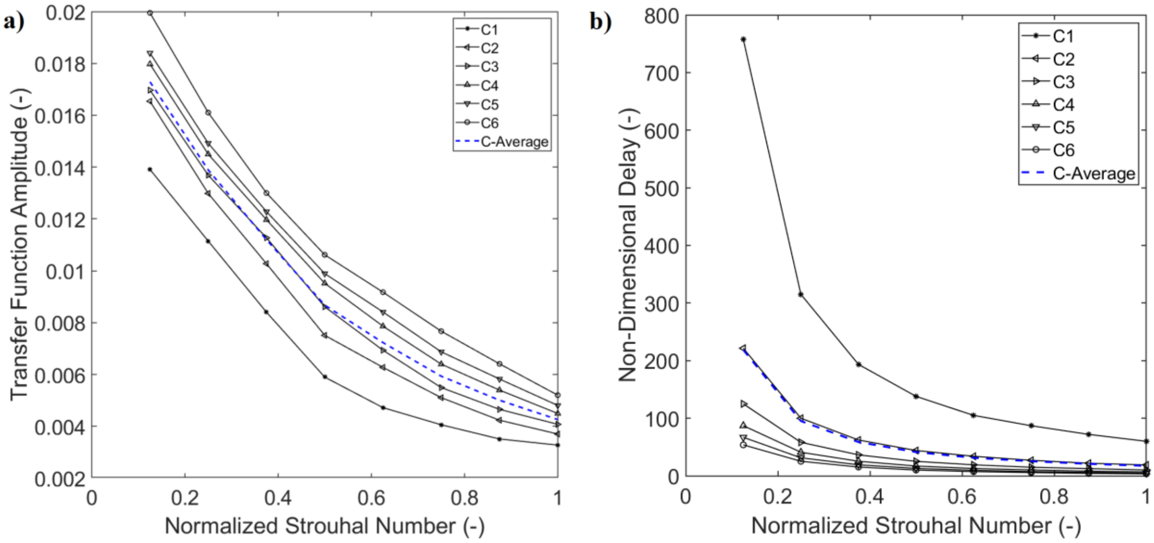

Figure 4-12 – Transfer functions of heat convection over the six primary battery cells. a) Transfer function amplitude, and b) non-dimensional delay of the transfer function. $Fluid = Air$ and $a = 10\%$.

Figure 4-12 clearly shows that the transfer function's amplitude decreases as the excitation frequency increases, suggesting that the system is more responsive to lower excitation frequencies. Former studies in which the inlet fluid velocity was excited rather than the thermal load have also exhibited a more substantial response at low frequencies [122, 131, 132]. In general, low frequencies tend to give the system more time to respond to the disturbances, leading to larger transfer function amplitudes due to the large wavelength of the excitation frequency. Additionally, as the modulation frequency is increased, the non-dimensional delay decreases, which is also in line with findings from other studies [131, 132]. This is again due to the available time between the disturbance and the heat convection becoming significant; thus, as the modulation frequency is increased, the non-dimensional delay decreases. As predicted, the transfer function amplitude of the cells located further downstream is greater than those nearer the inlet. This phenomenon can be explained by noting that the bulk temperature of the fluid flow increases as it travels towards the outlet. Therefore, as the fluid passes by each cell, the temperature difference between the surface of the battery cells and the fluid diminishes, which requires the convection coefficient magnitude to grow. Thus, larger amplitudes of the Nusselt number are produced, as evident by the temporals of the normalised Nusselt number in which the battery cells nearer the outlet produce significantly larger amplitudes than those near the inlet.

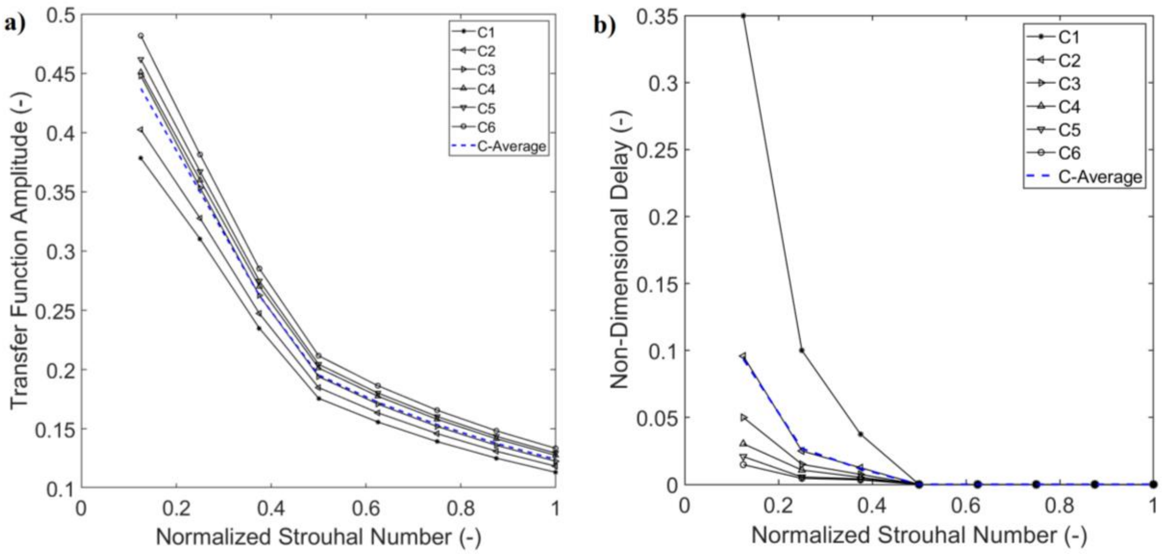

Figure 4-13 – Transfer functions of heat convection over the six primary battery cells. a) Transfer function amplitude, and b) non-dimensional delay of the transfer function. $Fluid = Water$ and $a = 10\%$.

The transfer function amplitudes and the non-dimensional delay for the six primary battery cells with water as the coolant fluid is shown in Figure 4-13a and 4-13b, respectively. Through observation, Figures 4-12 and 4-13 show the same trend of decrease in the transfer function amplitude and non-dimensional delay as the forcing frequency increases. However, the transfer function amplitude is significantly larger for the water cases than the air cases. This can be explained as follows. As shown in Figure 4-4, the steady-state convection coefficients for water are significantly larger than those of air due to the significant difference in thermophysical properties. Hence, under steady-state conditions, the surface temperature of the battery cells would be significantly smaller when water is used as the coolant fluid. This implies that for a given disturbance in the surface heat flux, the water cases experience more significant fluctuations in the convection coefficient and, consequently, the Nusselt number, resulting in larger transfer function amplitudes.

4.6.2 *Mildly nonlinear cases*

The forgoing transfer function findings were primarily based on the assumption that the system is dynamically linear, as confirmed by the spectral responses shown throughout section 4.6.1, where an insignificant second peak is observed. However, increasing the modulation amplitude leads to some cases becoming either mildly nonlinear – a small second peak appears, or strongly nonlinear – where multiple large peaks occur. An example of a mildly nonlinear case can be seen in Figure 4-14, where the modulation amplitude is 30%, the forcing frequency is 0.25 Hz, and the coolant fluid is air. It is clearly observed that the

Nu response of batter cell one no longer represents a sinewave, and the response of cells three and six are starting to deviate from a regular sinewave, a clear indication of nonlinearity. This observation is further confirmed by the spectral response of Nu, where a small second peak and an insignificant third peak can be seen.

Nevertheless, increasing the forcing frequency from 0.25 Hz to 1.00 Hz leads to a decrease in the nonlinear response of the system. Figure 4-15 shows the Nusselt number temporals and spectral response at a modulation amplitude of 30% and forcing frequency of 1.00 Hz for air. Comparing Figures 4-14a and 4-15a, through observation, the Nu response of cell one has changed from nonlinear to linear. However, the spectral response of Nu still shows multiple harmonics. Although the strength of the second peak is lower than that shown in Figure 4-14b, it is still not insignificant. Thus, the case shown in Figure 4-15 is still mildly nonlinear. Furthermore, the general trend of increase in the normalised Nu amplitude is still observed as the forcing frequency increases, as shown in Figures 4-6, 4-7, 4-8, and 4-9. Figures 4-16 and 4-17 show air cases with a modulation amplitude of 30% with forcing frequencies of 1.50 and 2.00 Hz, respectively. Increasing the modulation frequency gives the same trend of the system's nonlinearity decreasing. However, the spectral response of Nu still implicates the dynamics of these systems being mildly nonlinear.

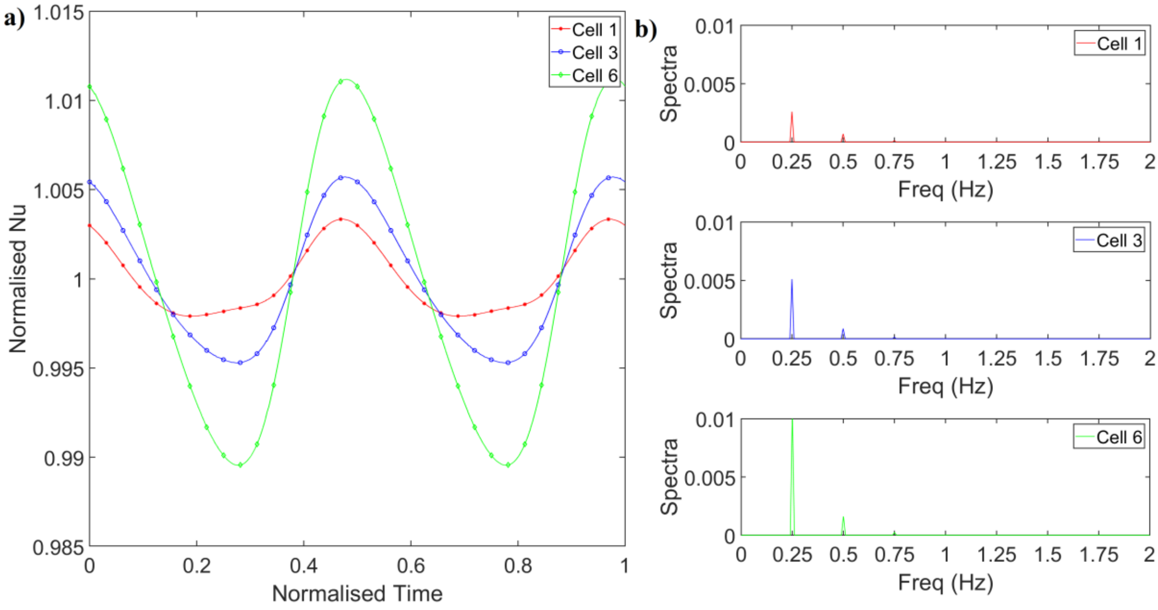

Figure 4-14 – a) Temporal evolution of Nu over battery cells' 1, 3, and 6, b) Spectral response of Nu. $Fluid = Air$, $a = 30\%$, and $f = 0.25\ Hz$.

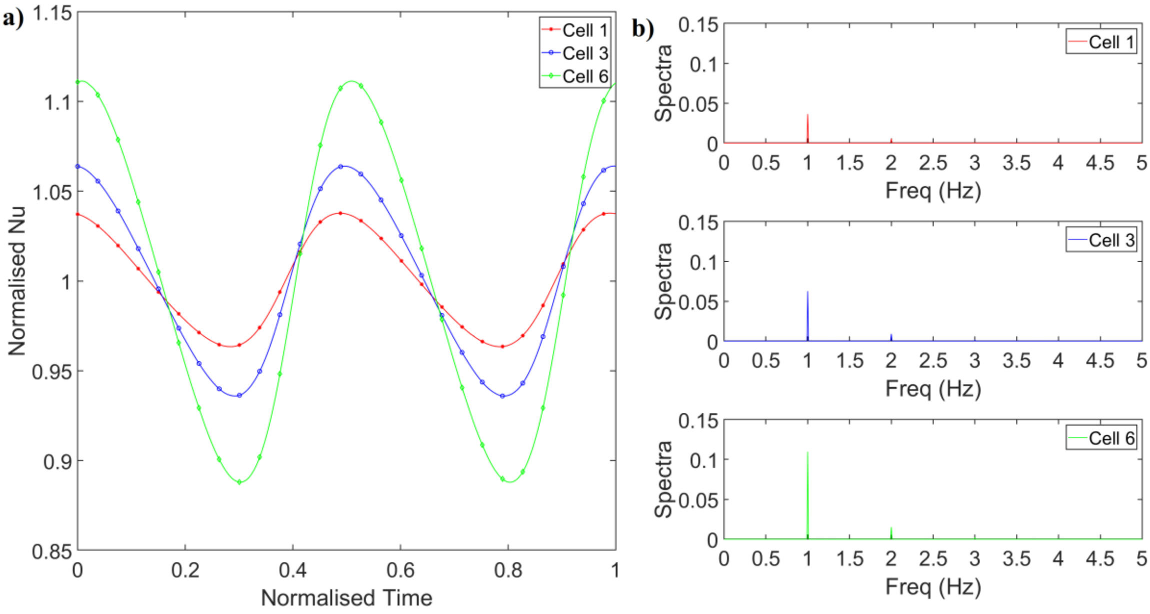

Figure 4-15 – a) Temporal evolution of Nu over battery cells' 1, 3, and 6, b) Spectral response of Nu. $Fluid = Air$, $a = 30\%$, and $f = 1.00\ Hz$.

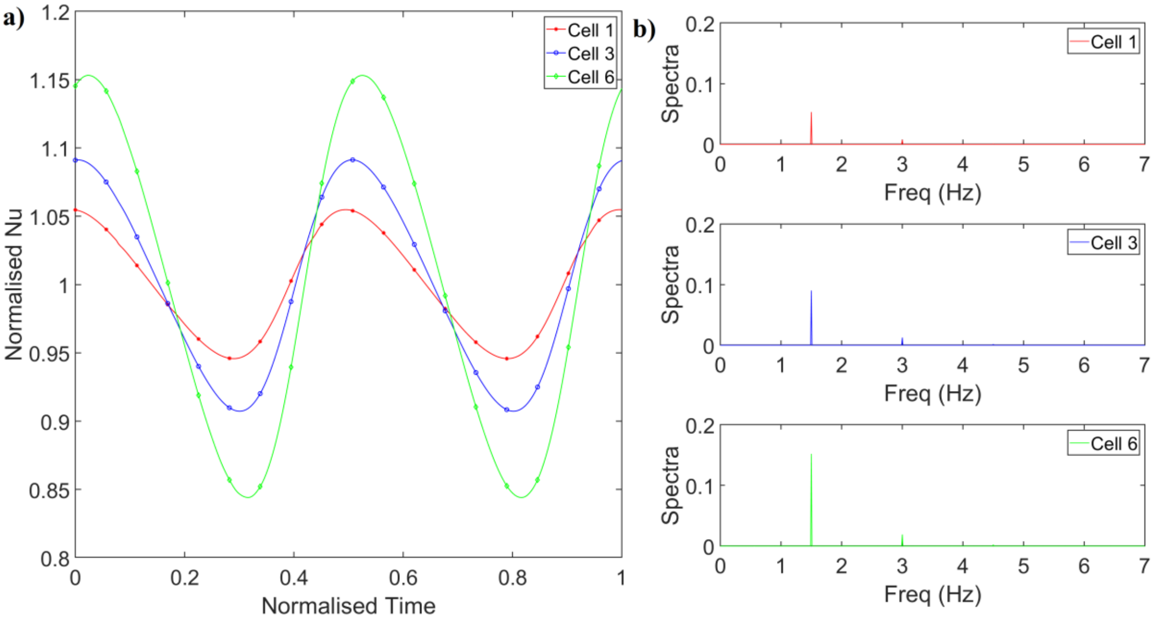

Figure 4-16 – a) Temporal evolution of Nu over battery cells' 1, 3, and 6, b) Spectral response of Nu. $Fluid = Air$, $a = 30\%$, and $f = 1.50\ Hz$.

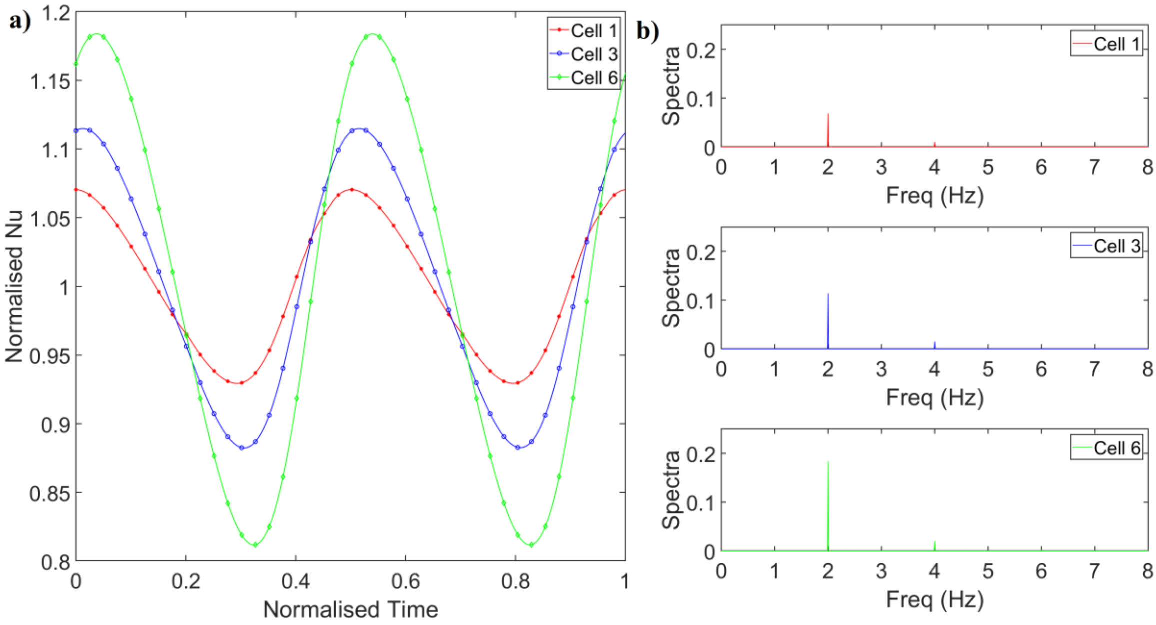

Figure 4-17 – a) Temporal evolution of Nu over battery cells' 1, 3, and 6, b) Spectral response of Nu. $Fluid = Air$, $a = 30\%$, and $f = 2.00\ Hz$.

Increasing the modulation amplitude to 30% for water and the nanofluid cases led to results like those shown in Figures 4-10 and 4-11, where Nu's temporal evolution and the spectral response show no signs of nonlinearity, making them dynamically linear. Thus, for brevity, they are not shown.

However, increasing the modulation amplitude of the water cases to 60% leads to the appearance of nonlinearity. The time trace and spectral response of the Nusselt number for water with the modulation amplitude of 60% and forcing frequency of 0.25 Hz is shown in Figure 4-18a and 4-18b, respectively. From visual observation, the normalised Nu response in Figure 4-18a represents a regular sinewave. However, the FFT gives a multi-harmonic response – a significant spike at the excitation frequency and a minor spike at double the excitation frequency.

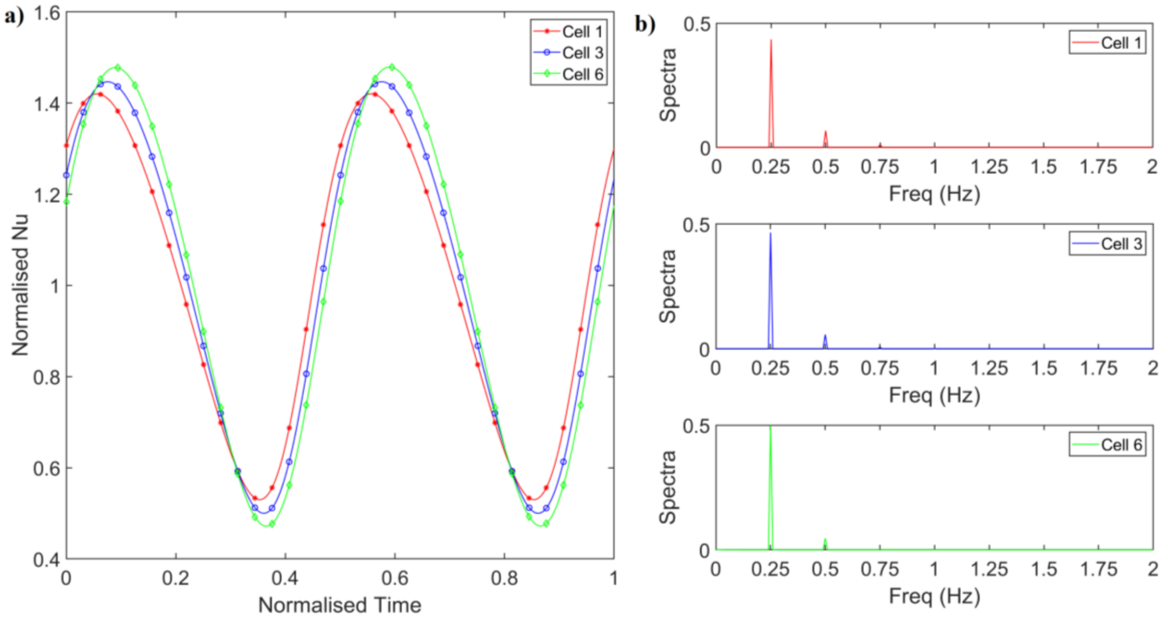

Figure 4-18 – a) Temporal evolution of Nu over battery cells' 1, 3, and 6, b) Spectral response of Nu. $Fluid = Water$, $a = 60\%$, and $f = 0.25\ Hz$.

4.6.3 *Strongly nonlinear cases*

An example of a completely nonlinear case can be found in Figure 4-19, where the coolant fluid is air, the amplitude of modulation is 60%, and the forcing frequency is 0.25 Hz. As seen in Figure 4-19a, the temporal response of the normalised Nu for battery cell one has wholly deviated from a sinewave along with the response of cells three and six. This is further supported by the spectral analysis of Nu, shown in Figure 4-19b, where multiple prominent secondary peaks are observed. For the same case with a 30% amplitude modulation, three total peaks were observed in the spectral response for cell one; however, increasing the amplitude modulation to 60% leads to five total peaks occurring for the same cell, with the most significant peak being at the excitation frequency. This provides a clear indication that the system dynamics have become strongly nonlinear.

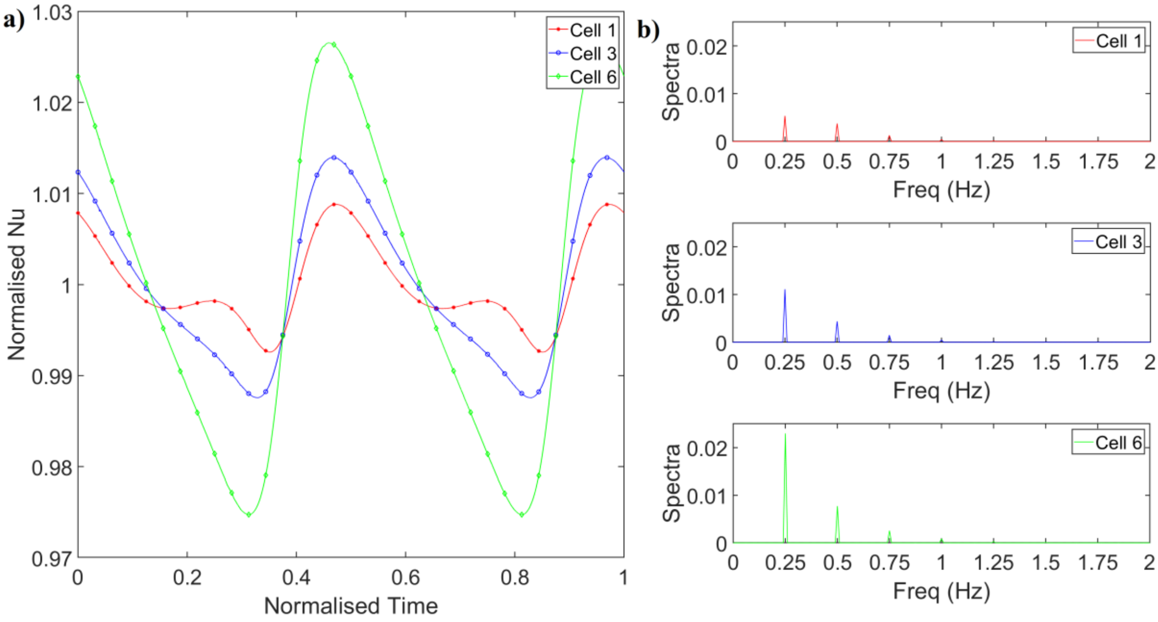

Figure 4-19 – a) Temporal evolution of Nu over battery cells' 1, 3, and 6, b) Spectral response of Nu. $Fluid = Air$, $a = 60\%$, and $f = 0.25\ Hz$.

Furthermore, as expected, keeping the same coolant fluid and modulation amplitude but increasing the forcing frequency decreases the nonlinearity. Figures 4-20, 4-21, and 4-22 show the Nusselt number's temporal and spectral response with a forcing frequency of 1.00, 1.50, and 2.00 Hz, respectively. Comparing Figures 4-19a and 4-20a shows that although the normalised Nu for cell one does not conform to a regular sinewave, cell one from Figure 4-20a is far closer to a sinewave than Figure 4-19a. Additionally, comparing Figures 4-19b and 4-20b shows that the spectral response of cell one from Figure 3-19b has five peaks, whereas cell one from Figure 4-20b only has four, indicating a reduction in the system's nonlinearity. Regardless, the system remains strongly nonlinear due to the ratio of the harmonics.

Increasing the forcing frequency to 1.50 Hz leads to another reduction in the harmonics appearing in the spectral response. As observed from Figure 4-21b, the spectral response of Nu for cell one only shows three peaks, whereas, in Figure 4-20b, the spectral response has four peaks. Although the number of harmonics has reduced with increasing modulation frequency, the strength of the harmonics has remained. Thus, increasing the forcing frequency still renders these cases strongly nonlinear. Moreover, just like in previous cases, the trend of an increase in the normalised Nu amplitude with increasing modulating frequency is still present in the cases where the modulation amplitude is 60%.

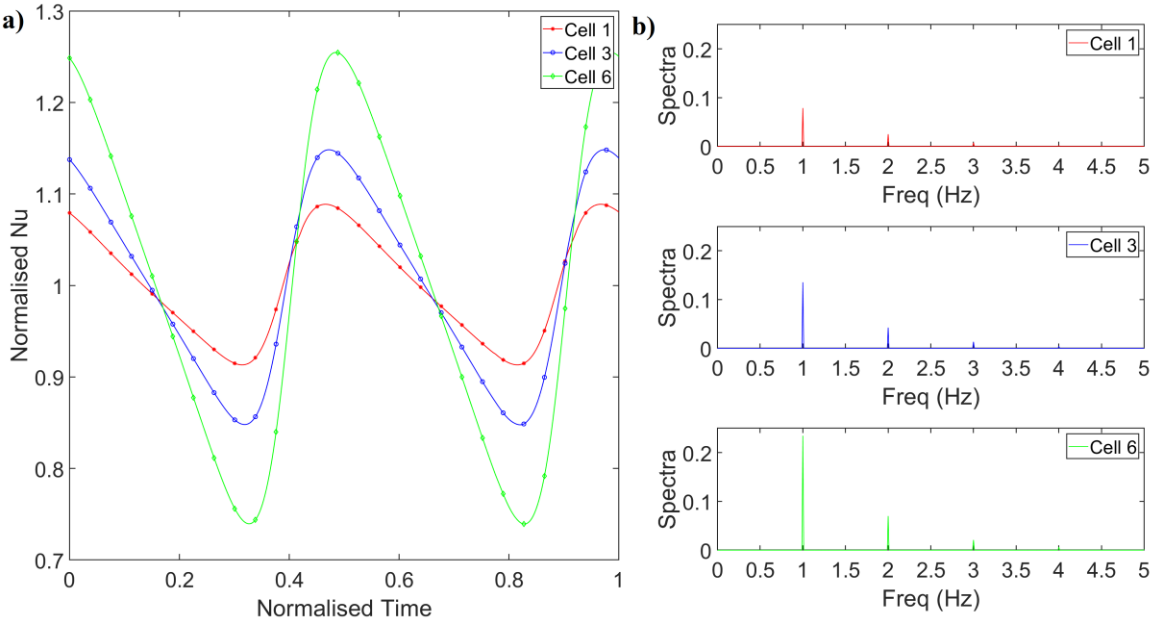

Figure 4-20 – a) Temporal evolution of Nu over battery cells' 1, 3, and 6, b) Spectral response of Nu. $Fluid = Air$, $a = 60\%$, and $f = 1.00\ Hz$.

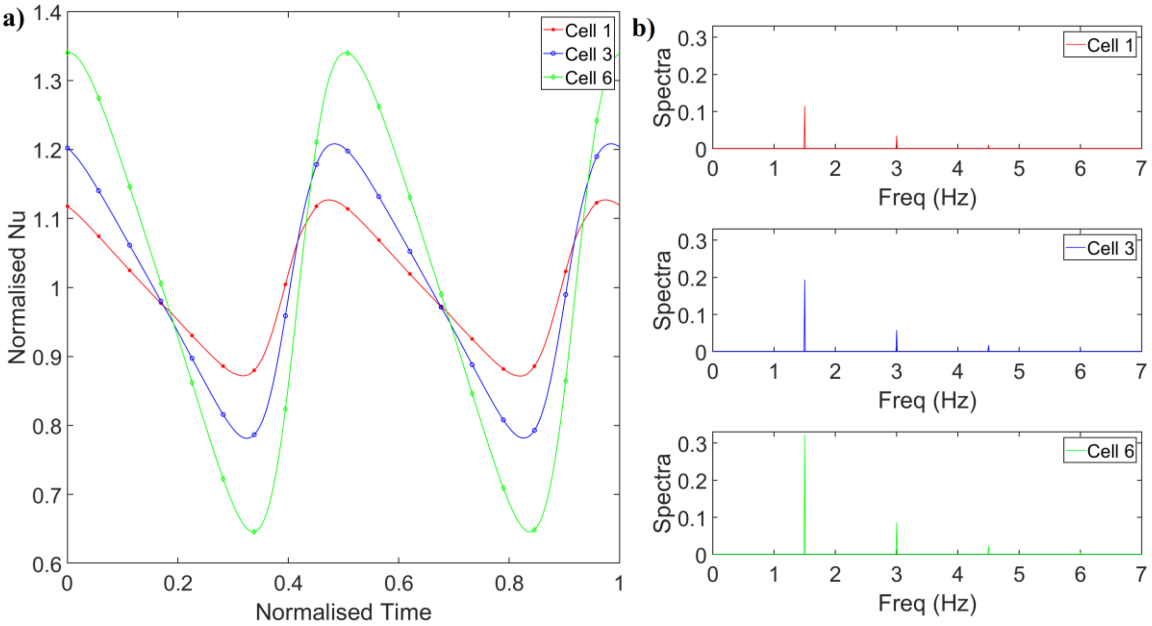

Figure 4-21 – a) Temporal evolution of Nu over battery cells' 1, 3, and 6, b) Spectral response of Nu. $Fluid = Air$, $a = 60\%$, and $f = 1.50\ Hz$.

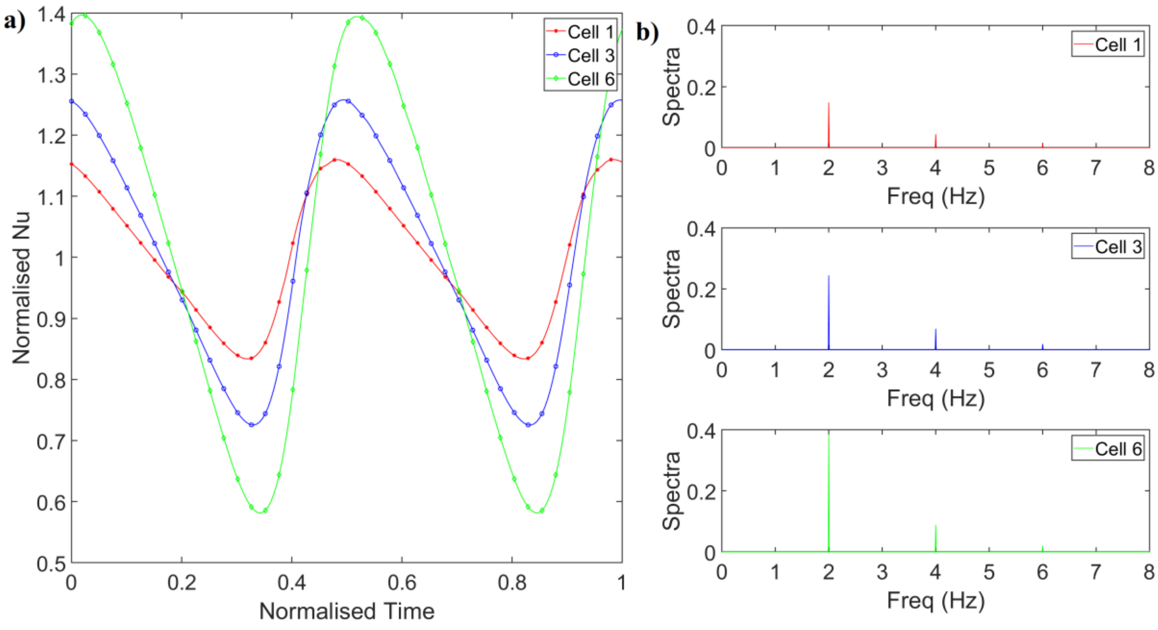

Figure 4-22 – a) Temporal evolution of Nu over battery cells' 1, 3, and 6, b) Spectral response of Nu. $Fluid = Air$, $a = 60\%$, and $f = 2.00\ Hz$.

4.6.4 *Measure of nonlinearity*

The findings presented throughout Sections 4.6.1, 4.6.2, and 4.6.3 are further supported by Figures 4-23, 4-24, 4-25, and 4-26, which show the Lissajous patterns (phase portraits) of the normalised Nusselt number vs normalised input signal. Figures 4-23 and 4-24 are for the air cases at all three modulation amplitudes and forcing frequencies of 0.25 Hz and 2.00 Hz, respectively. Figures 4-25 and 4-26 are for the cases of water at all three modulation amplitudes and forcing frequencies of 0.25 Hz and 2.00 Hz, respectively. Previous studies have used phase portraits as another method of analysing the linearity of a dynamic system [122, 133]. If a phase portrait of a dynamic system is perfectly axisymmetric, the system is considered a linear system [134]. However, if the dynamic system exhibits any signs of non-linearity, the phase portraits would deviate from symmetry. Thus, phase portraits are an effective method of assessing the linearity of a dynamic system.

In Figures 4-23a and 4-24a, the oval shapes of the phase portraits are axisymmetric; therefore, these two cases can be considered linear, as suggested by their spectral responses. However, observing Figures 4-23b and 4-24b, the oval shapes have begun to deviate from symmetry and can no longer be considered linear, corresponding to mildly nonlinear cases. The symmetrical feature is no longer present for the cases shown in Figures 4-23c and 4-24c, indicating a clear departure from any signs of linearity. Thus, the Lissajous patterns shown in Figures 4-23 and 4-24 confirm the analysis presented in Figures 4-6, 4-14, 4-19, and Figures 4-9, 4-17, and 4-22, respectively.

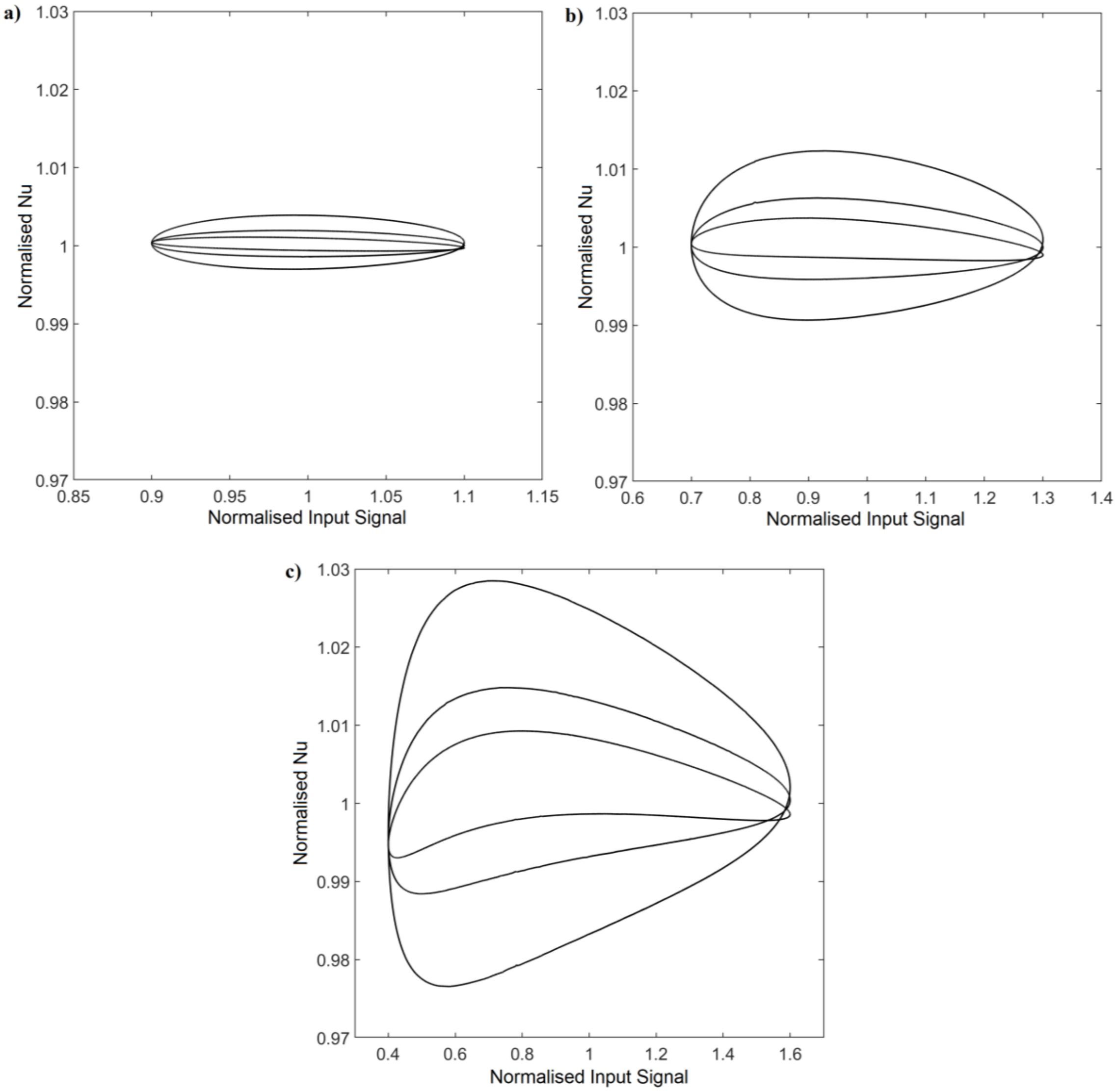

Figure 4-23 – Lissajous patterns (phase portraits). a) linear case, $a = 10\%$, b) mildly nonlinear case, $a = 30\%$, c) strongly nonlinear case, $a = 60\%$. $Fluid = Air$, and $f = 0.25\ Hz$.

Further, the Lissajous patterns for the water cases confirm the validity of the FFT responses shown in previous sections. Comparing Figures 4-25a and 4-26a shows that as the forcing frequency increases, the system’s nonlinearity diminishes. As previously stated, this phenomenon can be described by the interaction time of the fluid and the battery cell’s surface heat flux. As the frequency of modulation increases, the time allowed for these complex interactions decreases, not allowing the disturbance to interact with the fluid around the battery cell fully. This trend continues throughout Figures 4-25b and 4-26b. A departure from symmetry can be observed in Figure 4-25c; however, this deviation is not as significant as in Figures 4-23c and 4-24c. Therefore, the case presented in Figure 4-25c can be considered mildly nonlinear. Unlike the linear cases shown in section 4.6.1, predicting the dynamics of nonlinear systems is cumbersome and cannot be easily predicted using the classical transfer function approach. On many occasions, the dynamics of nonlinear systems can only be predicted using high-order modelling, which is time-consuming and computationally expensive. Therefore, it is essential to identify scenarios where the system dynamics are nonlinear.

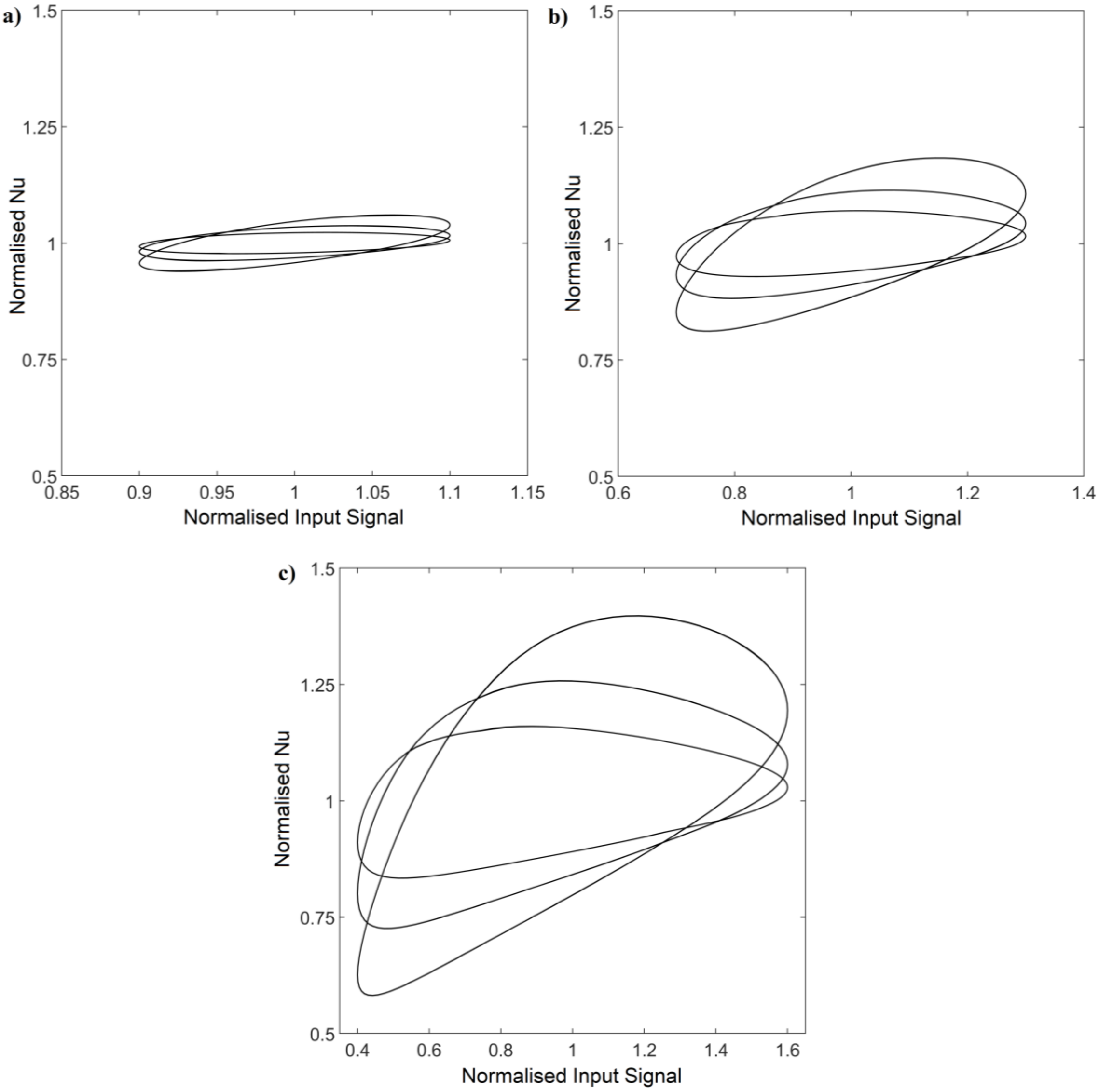

Figure 4-24 – Lissajous patterns (phase portraits). a) linear case, $a = 10\%$, b) mildly nonlinear case, $a = 30\%$, c) strongly nonlinear case, $a = 60\%$. $Fluid = Air$, and $f = 2.00\ Hz$.

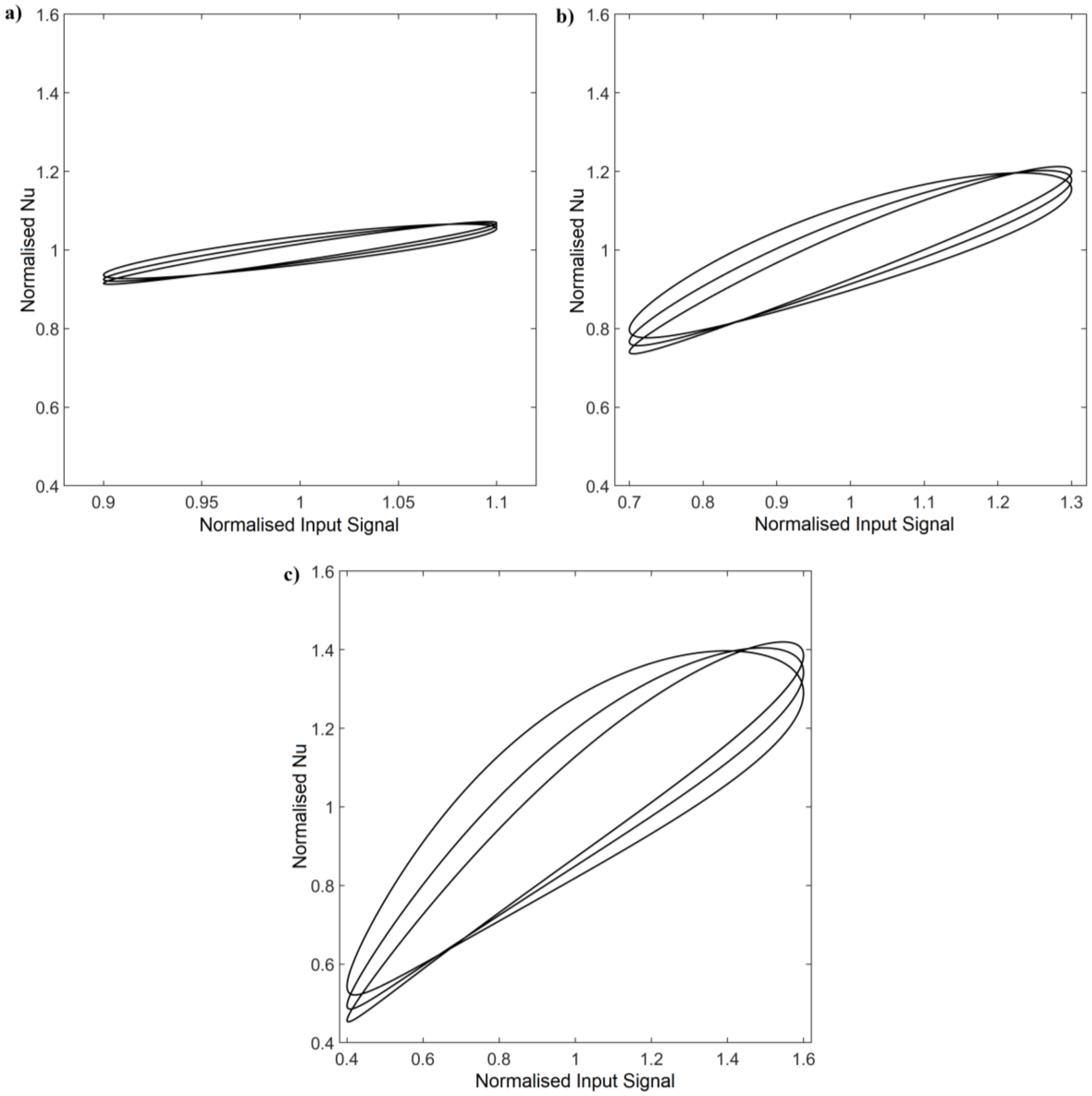

Figure 4-25 – Lissajous patterns (phase portraits). a) linear case, $a = 10\%$, b) linear case, $a = 30\%$, c) mildly nonlinear case, $a = 60\%$. $Fluid = Water$, and $f = 0.25\ Hz$.

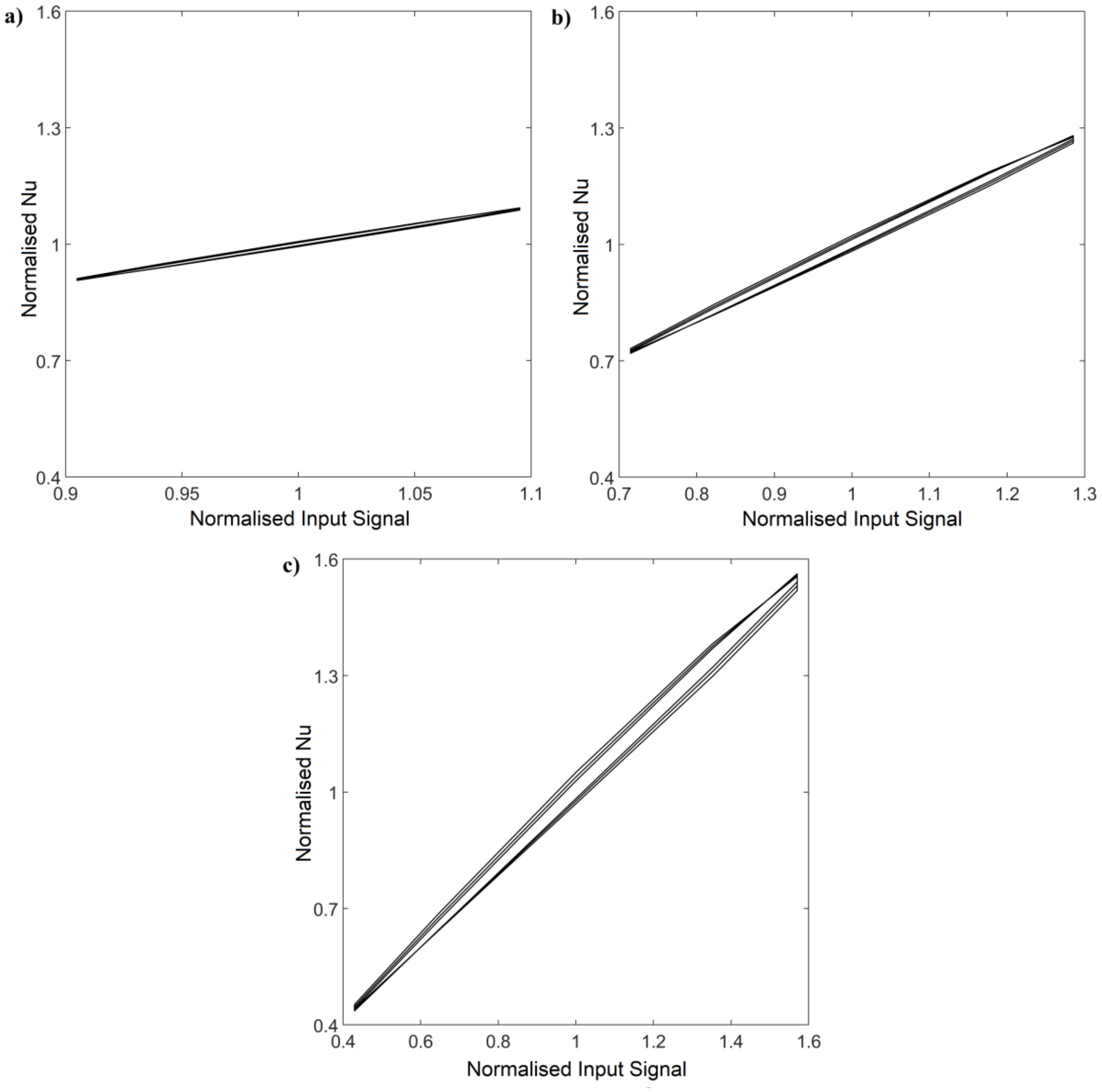

Figure 4-26 – Lissajous patterns (phase portraits). a) linear case, $a = 10\%$, b) linear case, $a = 30\%$, c) mildly nonlinear case, $a = 60\%$. $Fluid = Water$, and $f = 2.00\ Hz$.

For any dynamic system that exhibits a perfectly linear behaviour, the output will have the same spectral content as the excitation. Therefore, it is necessary to develop appropriate methods for assessing the non-linearity of any given system. Once such method is by taking the discrete Fourier transform and the inverse discrete Fourier transform and then isolating the response of the thermal system at the forcing frequency. The difference between the actual output and the response at the forcing frequency can be used as a measure of nonlinearity.

The measure of nonlinearity used to assess the divergence of the system dynamics from linearity, described in Ref. [135], are calculated using the relation described in Eq. (4.8).

$$\delta_{nL} = \frac{n_e - F_d}{n_e} \tag{4.8}$$

where δ_{nL} is the measure of nonlinearity, n_e is the Euclidean norm of the normalised Nusselt number of each battery cell, and F_d is the discrete Fourier transform at the forcing frequency of the normalised Nusselt number of each battery cell. Eq. (4.8) collapses and equals zero for a completely linear system, whereas, for a strongly nonlinear system, the δ_{nL} is equal to one. Thus, the system can only have a value between zero and one. The maximum measure of nonlinearity, δ_{nL}, at varying amplitudes of modulation and excitation frequencies for air and water are shown in Figure 4-27. The measure of nonlinearity for nanofluids at a concentration of 2.5 and 5.0% are similar to that of water, shown in Figure 3-27b, with minor differences; thus, they are not shown.

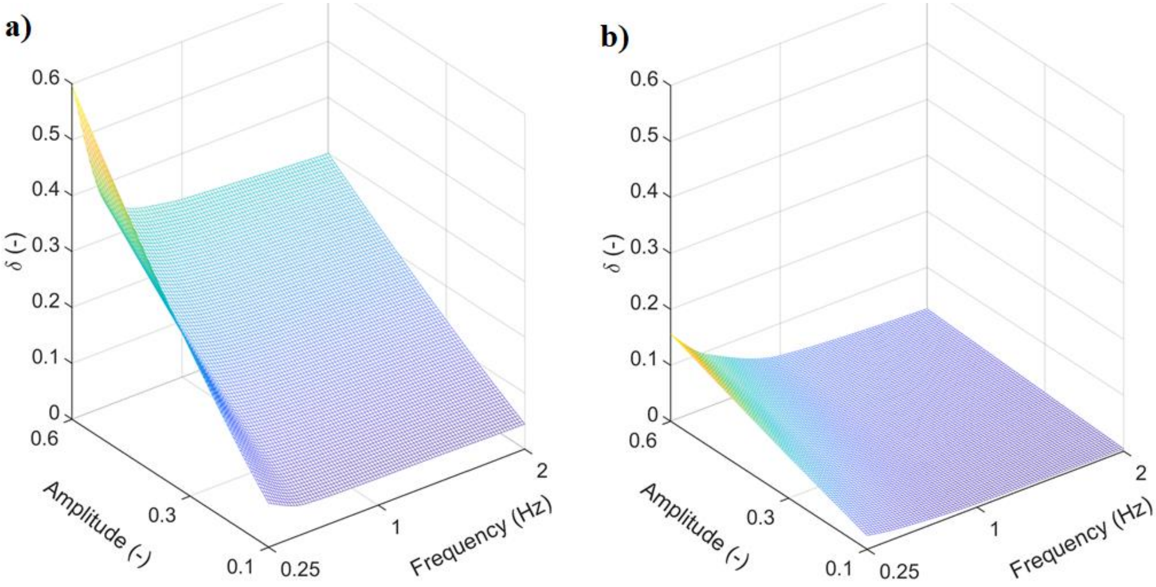

Figure 4-27 – Maximum value of measure of nonlinearity in Nusselt number at different amplitudes of modulation and excitation frequencies. a) $Fluid = Air$, b) $Fluid = Water$.

From Figure 4-27a, as the modulation amplitude is increased from 10 to 30%, there is a sharp increase in the measure of nonlinearity. This increase is further intensified as modulation amplitude is further increased to 60%, confirming the strongly nonlinear dynamic response of the system given in the spectral response and the Lissajous patterns.

However, doubling the forcing frequency from 0.25 Hz to 0.50 Hz drastically decreases the measure of nonlinearity irrespective of the modulation amplitude. This decrease continues as the forcing frequency is further increased; however, the decrease is less substantial than the decrease noticed at the beginning. A similar trend can also be observed in Figure 4-27b. However, the maximum measure of nonlinearity is far smaller for the cases of water than that of air. Therefore, as expected from the spectral response, the system dynamics behave linearly at low amplitudes and higher forcing frequencies tend to force the system to behave linearly. Most importantly, the tendency of air to feature highly nonlinear behaviour at high modulation amplitudes and low forcing frequencies is significantly stronger than that of water and nanofluids.

The origin of nonlinear system behaviour in the present study is the interaction of the cooling fluid with the boundary layers around and the wake region behind each battery cell. It is well established that such interactions are rather complex [136, 137]. The current results of the measure of nonlinearity indicate that long-duration (low frequencies) disturbances have enough time to interact with the system, producing a nonlinear response. Conversely, low-duration disturbances (high frequencies) do not have enough time for the fluid-dynamic interactions and, hence, present dynamically linear systems at low modulation amplitudes. Furthermore, short-term disturbances, particularly at low amplitudes, generate linear dynamics. Thus, the classical transfer function approach can be a computationally inexpensive tool to predict thermal dynamics. However, this approach becomes inapplicable as the modulation amplitude increases; extensive high-order modelling is required to accurately evaluate the heat transfer dynamics. The significant difference between the measure of nonlinearity of air and water/nanofluid-cooled systems is probably due to the significant differences in their thermophysical properties and, in particular, the Prandtl number. Lower values of Prandtl number for air in comparison to water hinder convective heat transfer at fixed values of Re. This renders a stronger nonlinear response of Nu at any given amplitude for air. However, it should be noted that the current study does not consider the battery cell’s electrochemistry. Although it is speculated that electrochemistry does not considerably influence the results, this issue should still be noted during any generalisation of the results presented throughout this chapter.

4.7 *Conclusions*

One of the biggest issues facing the popularity of EVs is their battery performance which is heavily influenced by their operational temperature. Due to numerous vehicle manoeuvres and driving patterns, battery cells within EVs are exposed to a wide range of temporal scenarios in heat generation and transfer. Therefore, effective thermal control of batteries is essential. One such method is the use of predictive tools to understand battery behaviour. However, such predictions are conventional for linear systems using the classical transfer function approach. However, this method becomes cumbersome and complicated for any real system with signs of nonlinearity. Hence, it is crucial to determine the conditions in which the battery thermal management system features linear and nonlinear dynamics due to disturbances imposed on the battery cell's surface heat flux. This was achieved by utilising the principle of Fourier transforms – noting that any temporal disturbance can be broken down into a series of sinusoids with varying amplitudes and frequencies. Therefore, the system response was examined by numerically simulating a battery module with six primary cells, where each battery cell was imposed to sinusoidal fluctuations in the surface heat flux. The resultant Nusselt number was then analysed in the time and frequency domains. Further, a rigorous method of measuring the nonlinearity was applied to the computational data to determine conditions in which the system response could be dynamically nonlinear. The key findings of this study can be summarised as follows.

- The dynamic response of the convective heat transfer from the battery module remains linear at low modulation amplitudes ($a = 10\%$).
- Under linear conditions, using the amplitude and phase delay, a transfer function can be developed to represent the surface-average Nusselt number which features characteristics of a conventional low-pass filter. This approach is only viable for disturbances at a low modulation amplitude and short duration.
- As the modulation amplitude increases, the average Nusselt number becomes mildly nonlinear or strongly nonlinear.
- Long-duration temporal disturbances (low frequency) of the battery cell's surface heat flux tend to generate strongly nonlinear responses. This can be attributed to the long time available to complete the fluid dynamic and heat transport interactions.
- Increasing the forcing frequency decreases the signs of nonlinearity.

Chapter 5. Transient loads on a Li-ion battery module

Another primary concern for battery thermal management systems is the lack of ability to adequately manage the temperature of battery cells within a battery module due to significant power draws [138, 139]. The highly unpredictable nature of an automobile drive to harshly accelerate or decelerate the vehicle would lead to drastic strain on a battery pack. Thus, this chapter aims to understand the behaviour of a Li-ion battery module to power discharge in a short period. This is done by analysing the transient thermal response of said battery module due to temporal changes in the internal heat generation [140]. The battery module is designed based on real cell dimensions. Two coolant fluids are used throughout this chapter: air and water. The power surges are based on driving data taken from standard drive cycles, where large accelerations occur in short periods. The numerical results are compared against existing correlations, direct numerical simulation (DNS) data, and experimental data for validation. The average battery cell surface temperature is analysed, and a systematic approach to understand the delay of cooling, the time taken to reach the peak temperature, and the time taken to cool down the battery cells is provided.

5.1 *Model configuration and assumptions*

The general sketch of a battery module, the simulated module, and a three-dimensional schematic of a single cell section is given in Figure 5-1. The battery module was arranged using a staggered series-parallel configuration with six primary battery cells [33, 40, 54]. A single cell section has a length, L, of 100 mm, height, H, of 50 mm, and a depth, D, of 100 mm [66], as shown in Figure 5-1c. The battery cells have a radius, R, of 20 mm [66]. The subsequent assumptions were made throughout this study:

- The fluid flow is fully turbulent with a steady inlet velocity.
- The ideal gas model is used for cases where the coolant is air. For cases with water, a constant density model is utilised.
- The fluid is thermally and hydrodynamically fully developed.
- Gravitational effects and heat generation due to viscous resistance are ignored.

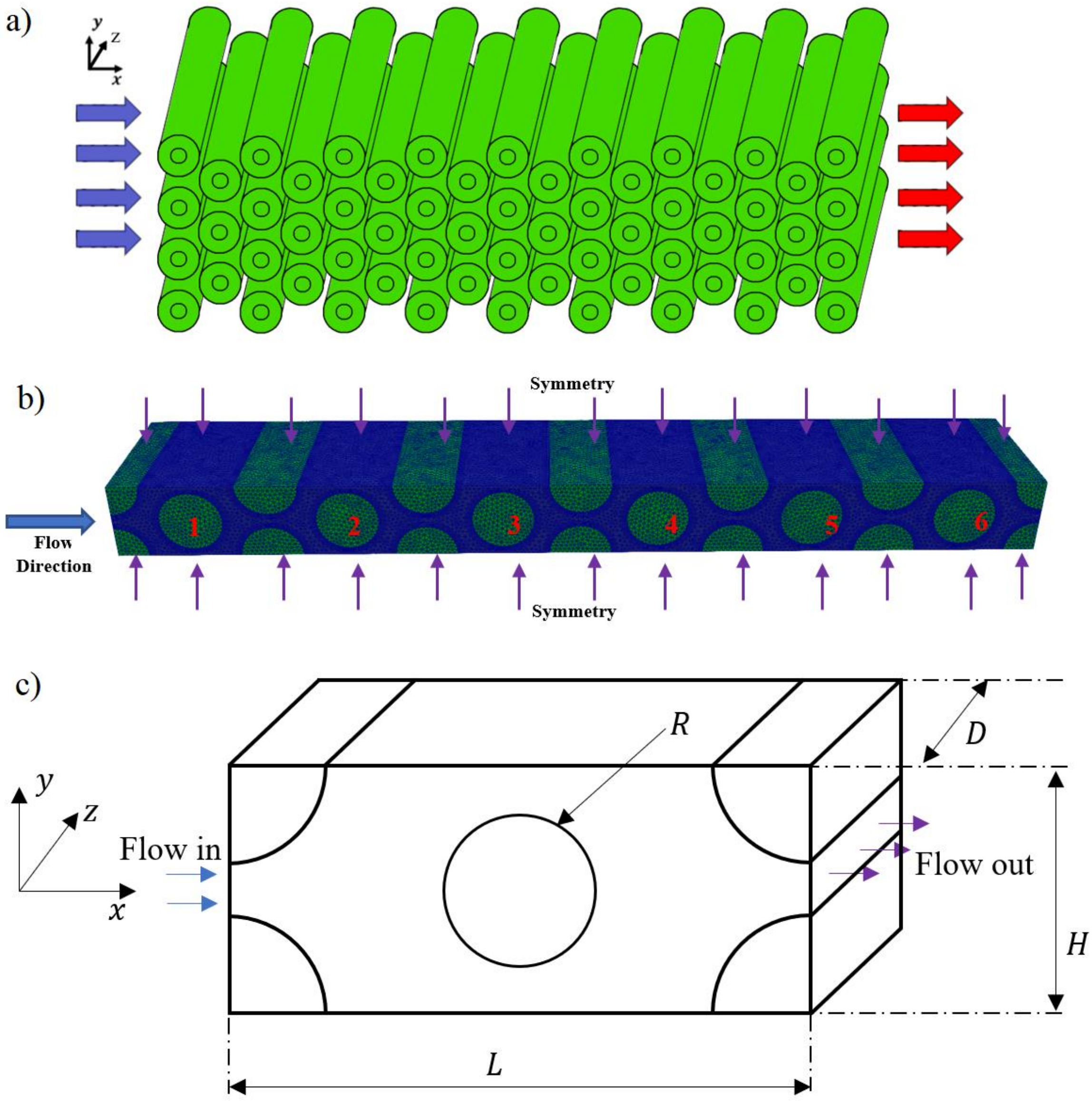

Figure 5-1 – a) General battery module design, b) Simulated model – blue region is the fluid, green regions are the battery cells, c) Schematic of a single cell section.

Moreover, the unsteady internal heat generation was applied to each battery cell once the model reached steady-state conditions. When an EV is used, the current withdrawal from the battery cells causes heat generation inside each cell. The heat produced would need to travel to the surface of the battery cell before being convected by the fluid flow. Thus, the heat generation inside the battery cells was modelled using a volumetric heat source, S_c – see Refs. [110, 141, 142]. The relationship between the volumetric heat source and current withdrawal from the battery cell is explained in section 5.3.

A symmetry boundary condition was applied to the model's top, bottom, front, and back regions since the battery module can be extended in the y and z-directions. The external surface of each battery cell is subject to a no-slip, boundary condition. Further, at the interface of the battery cells' surface, s, and the fluid, f, the temperature is set to be the same, $T_s = T_f$. The flux entering the fluid domain is set to be equal to but opposite to the battery cells; this is to say that the heat flux leading each battery cell is equal to the heat flux entering the coolant fluid, $q_s'' = -q_f''$. Finally, the ambient temperature of the fluid is set to 300 K, and the outlet is given an atmospheric pressure boundary condition.

The volumetric heat source, S_c, within each battery cell was modelled using a constant value of 2,000 W/m^3 under steady-state conditions. This value was chosen to mimic a running electric vehicle's battery and the fluid temperature prior to a sharp acceleration. Moreover, the internal heat generation value was calculated based on the current model geometry, shown in Figure 5-1, an average Li-ion energy conversion efficiency of 85% [112], and the 85 kW Tesla model S battery specifications [111]. The air's poor thermal conductivity and heat capacity demands high inlet velocities for adequate operation and to avoid damaging the battery cells [113]. Thus, the inlet velocity for air was chosen to be 17.5 m/s (Re = 44,000) based on the literature [113, 143]. For water, the Reynolds number was chosen to be 2,300 based on other studies [114–116]. The chosen Reynold numbers were kept constant throughout the study. The gravitational effects were safely ignored by calculating the Richardson number as described in Eq. (3.12a). At a Re of 44,000, the resultant Ri was equal to 0.000305. Forced convection would dominate the heat transfer if Ri < 0.1; therefore, the effects of natural convection were ignored.

The numerical simulations were conducted using OpenFOAM v2006, an open-source finite-volume method-based CFD software. A conjugate heat transfer (CHT) model named chtMultiRegionFoam was utilised to simulate the conduction within the solid regions (battery cells) due to the internal heat generation and convection from the surface of each battery cell due to the fluid flow. The latter was modelled using a three-dimensional, unsteady, turbulent flow solver coupled with the energy equation. The $k - \epsilon$ model mentioned in Chapter 3 was used to model the fluid flow accurately. The aforementioned ideal gas and constant density models were used to model air and water, respectively. The timestep was set to be five orders of magnitude smaller than the full-time scale to ensure accurate capture of the wake region and vortex shedding [144]. The second-order discretisation scheme was applied to every model and solver for enhanced accuracy. The study was conducted on an HPC called Cirrus using Intel Xeon E5-2695 Broadwell series processors, consisting of 36 cores. The resultant data was exported to MATLAB 2022a for post-processing.

5.2 *Drive cycles*

A range of atmospheric pollutants are emitted by internal combustion engine vehicles; thus, these vehicles need to be regulated worldwide. However, exhaust emissions are inherently variable and can be influenced by the slightest change in driving conditions. Therefore, the best method is to ensure repeatable test procedures for all experiments under standardised laboratory conditions known as dynamometer drive cycles [145]. There are a plethora of drive cycles available for a wide array of conditions around the world; however, for the current study, three drive cycles were chosen to represent distinct methods of driving passenger vehicles. These three drive cycles are shown in Figure 5-2. The first is the New York City cycle (NYCC), low-speed stop-and-go traffic conditions representing inner-city/central business district (CBD) driving. The second cycle is the SC03 drive cycle, also known as the Supplemental Federal Test Procedure (FTP) driving schedule. Finally, the first drive cycle is the Urban Dynamometer Driving Schedule (UDDS), also known as the city test. The US Environmental Protection Agency (US-EPA) uses the mentioned drive cycles are part of its standard vehicle and fuel emissions testing kit [146].

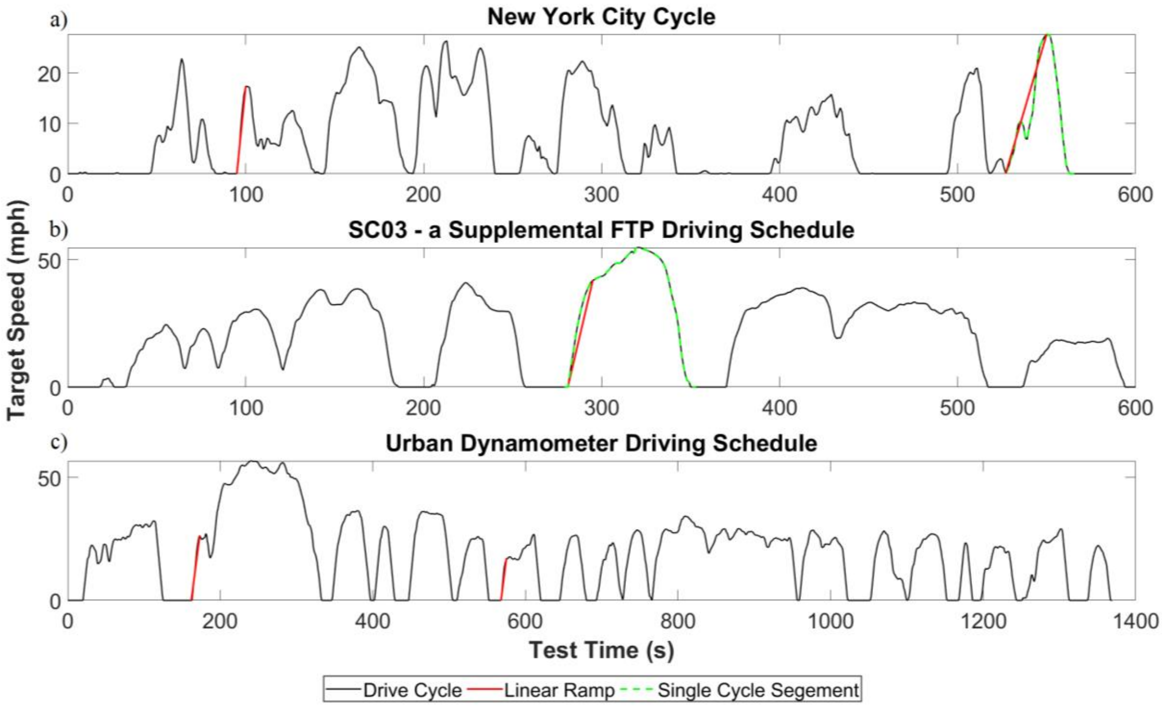

Figure 5-2 – Standard drive cycles. a) New York City cycle, b) SC03 drive cycle, c) Urban Dynamometer drive cycle. The solid-red lines represent the linear ramps and the dashed-green lines are for the single segments.

The conditions under which the batteries in an electric vehicle would be under high loads can be approximated using the drive cycles shown in Figure 5-2. For example, the EVs battery pack would be under extreme load each time the car is required to quickly accelerate to a high target speed. Therefore, two cases were chosen from the NYC cycle (NYCC1 and NYCC2), one from the SC03 cycle, and two from the UDDS cycle (UDDS1 and UDDS2). These cases are shown in Figure 5-2 as linear red lines. Furthermore, single-cycle segments were also chosen to simulate the battery module's thermal response and analyse the coolant's responsiveness to loading and offloading the internal heat generation – outlined using dashed-green lines in Figure 5-2.

5.3 *Internal heat generation*

The target speeds shown in Figure 5-2 were also used to calculate the approximate mechanical power required to achieve said target speed using Newton’s second law of motion as described in Eq. (5.1). This can then be used to form an equation for mechanical power by multiplying both sides by the change in velocity,

$$F = ma \tag{5.1a}$$

$$F \cdot du = ma \cdot du \tag{5.1b}$$

where the left-hand side of Eq. (5.1b) is the mechanical power of the vehicle. Integrating both sides leads to an equation describing the mechanical power using a vehicle’s mass, acceleration, and velocity:

$$P = ma\Delta u \tag{5.2}$$

where P is the mechanical power, m is the mass of a Tesla Model S – 2,250 kg, a is the vehicle's acceleration – calculated from Figure 5-2, and Δu is the change in velocity – also calculated from Figure 5-2. The battery standard used within the Tesla Model S is based on the specifications of the 18650 Lithium-ion cell format [111], the most commonly studied Li-ion cell – see Refs. [147–149] and Refs. [150, 151]. The battery cell current draw, I, can be calculated using the mechanical power equation and the 18650 cell specifications, which have an average nominal voltage of 3.5 V.

$$I = \frac{P}{V} \tag{5.3}$$

Moreover, it was found that the internal resistance of a Li-ion cell is inherently wavering depending on its manufacturing quality, storage, usage, life cycle, and operational temperatures [25, 29, 148]. Therefore, the internal resistance of a battery cell can be drastically inconsistent, from 2.83 mΩ [148, 152] to 81.6 mΩ [153, 154] and as high as 140 mΩ [155] and 190 mΩ [156]. Since the current study is interested in extreme case scenarios, the highest internal resistance of 190 mΩ was chosen to simulate the worst-case scenario. Using this value of internal resistance, the current cell geometry shown in Figure 5-1, and a battery cell energy efficiency of 85%, linear ramps of the volumetric heat generation, S_c, were calculated to represent the five ramp and the two single-segment cases,

$$S_c = \frac{I^2 R_i}{V_s} \tag{5.4}$$

where I is the battery cell current draw, R_i is the battery cell internal resistance, and V_s is the cell volume.

5.4 *Grid independency study*

As shown in Figure 5-1b, an unstructured tetrahedral mesh for the fluid and solid domains was produced. The fluid domain also contained prism cells to capture the boundary layer around each battery cell accurately. This type of mesh was chosen to reduce the mesh cell skewness while also reducing the overall cell count, as the cell count is directly linked to the computational demand of the model. Eight tests were conducted with varying cell sizes to determine the grid at which the highest accuracy could be achieved without overburdening the computational model. Here, cell size determines the values of all other mesh parameters, such as the surface and volumetric cell size and prism layer thickness. Once the Nusselt number of each battery cell fell within an error band of one percent, the grid independency would be achieved. All tests were carried out at a Re value of 4,000. The results of the grid independency can be seen in Table 5-1. As the cell size is decreased, the mesh density increases and the solution converges to within an error margin of one percent. To further balance the model accuracy and computational demand, a cell size of 0.00175 was chosen.

Table 5-1 – Grid Independency.

	Cell size (m)	Number of cells	Maximum change in Nu (%)
Test 1	0.008	150,517	----
Test 2	0.006	171,952	5.12
Test 3	0.005	259,783	7.01
Test 4	0.004	457,927	4.28
Test 5	0.003	973,331	3.21
Test 6	0.002	2,830,531	1.13
Test 7	0.0015	5,978,251	0.62
Test 8	0.001	16,754,751	0.10

5.5 *Validation study*

The present study was validated by comparing against existing numerical and experimental data. These comparisons are given in Figure 5-3. Firstly, the model parameters were modified so that the flow occurs over a single battery cell rather than a fleet and the top and bottom walls of the model were extended. The comparison of the simulated results against the empirical correlations by Churchill and Bernstein [123] and Hilpert [125] are shown in Figure 5-3a. The simulated results are in exceptional agreement with correlations at low values of Re (laminar region) and, as expected, as the value of Re is increased, the error also increases. The max error in Figure 5-3a is 6.96% at a Reynolds number of 10,000. It should be noted that the empirical correlations contain errors as high as 20% [123]. Thus, the simulated data is still within the acceptable error margins. Therefore, the current model can be said to have an excellent agreement against the two empirical correlations.

The unsteady behaviour of the solver, chtMultiRegionFoam, was also evaluated by configuring the current model to become a simple channel flow without any battery cells. The inlet flow is exposed to ramped disturbances in its temperature, and the corresponding changes in the flow temperature at different locations along the domain were examined against DNS data by Christodoulou et al. [157]. The results of the comparison are shown in Figure 5-3b. Further, at a Re value of 3,900, the simulated drag coefficient, C_d, was compared against experimental data by Yogini Patel [124]. The current model resulted in a drag coefficient of 0.9105, whereas the experimental results found it to be 0.93 ± 0.005, an error of approximately 2.1%. Air flow across a bundle of cylinders was also compared against the correlation provided by Grimson [127]. At a Reynolds number of 20,000, the average Nusselt number of the model shown in Figure 5-1b was found to be 141.72, whereas the Grimson correlation found it to be 130.06, revealing an error of 8.97%.

The comparison of the single cylinder simulated results against the Churchill and Bernstein [123] correlation and against experimental data by Stephen Whitaker [126] is shown in Figure 5-3c and 5-3d, respectively. As anticipated, the numerical and experimental data in the laminar region are in excellent agreement with the simulated data. As the value of Re is increased, the error also increases. For comparison against the numerical data, the maximum error is found to be 7.89% at a Re of 8,000, with the lowest error being 0.74% at a Re of 150. However, comparing the experimental data, all errors are below 4%.

The favourable agreement among the simulated results, DNS data, empirical correlations and experimental data for air and water confirm the validity of the numerical analysis presented in the following section.

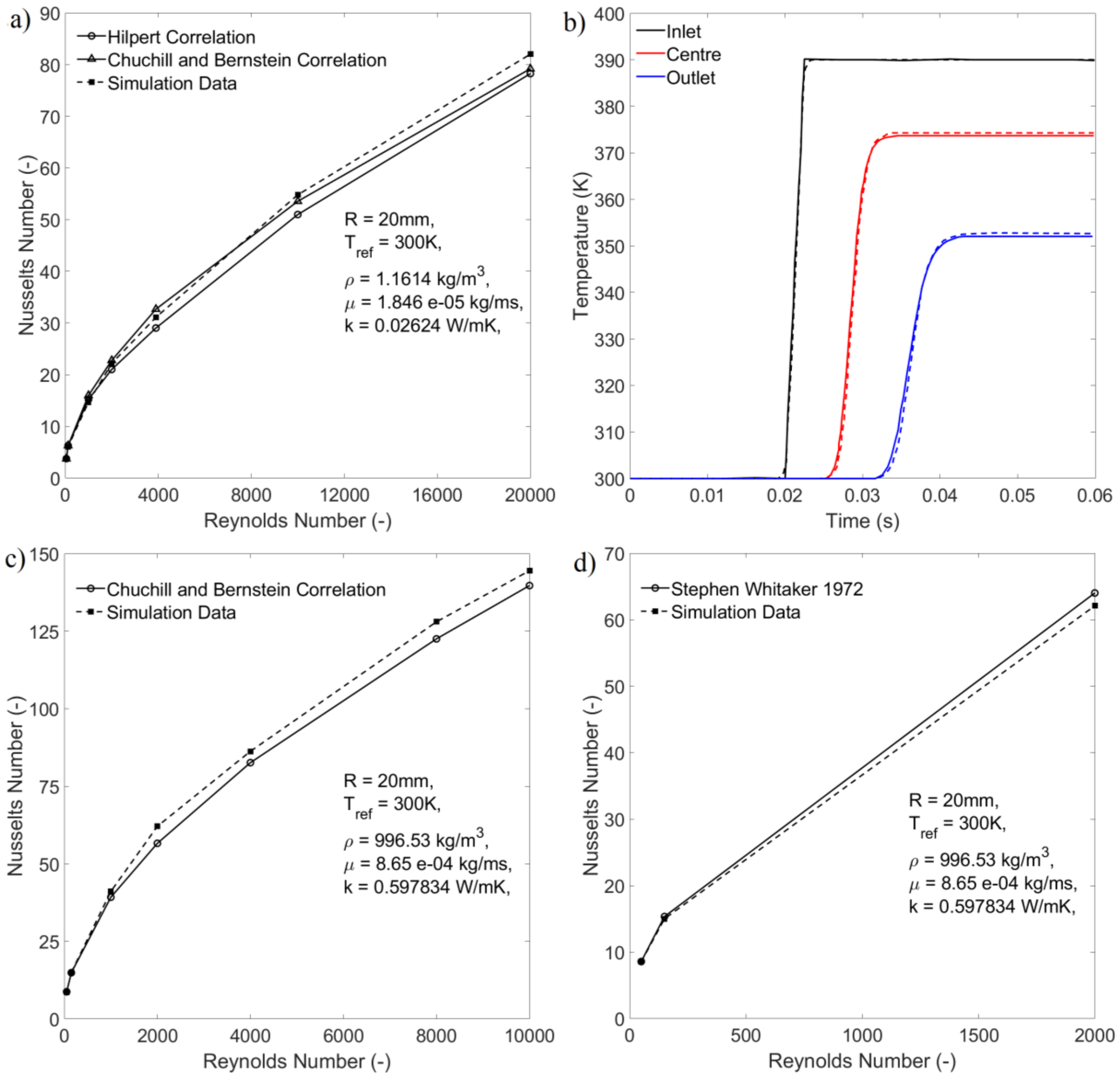

Figure 5-3 – Validation study. a) Single cylinder and Refs. [123, 125], $Fluid = Air$, b) Comparison of temporal variations at the inlet, centre, and outlet for unsteady response, $Fluid = Air; Re = 180$, where the solid lines is the DNS data and the dashed lines are the current model, c) Single cylinder vs numerical data [123], $Fluid = Water$, and d) Single cylinder vs experimental data [126], $Fluid = Water$.

5.6 *Results and discussion*

This section presents the battery cells' response to volumetric internal heat generation disturbances due to liner ramps and single-cycle segments. It should be noted that the inlet flow velocity of the fluids is kept constant; thus, the Reynolds number is also constant. Nusselt number is primarily a function of the Prandtl number, and Reynolds number in single-phase forced convection flows [158]; during cooling, variations in the coolant fluids' Prandtl number can be considered insignificant. As long as Re is kept constant, any modulation imposed on the internal heat generation would result in minor changes in the convective cooling. Therefore, the Nusselt number is not analysed; instead, the average surface temperature of the battery cells is considered. This allows for a thorough comparison between the effects of the different coolant fluids and the drive cycles and whether the individual battery cells' temperature and the cell-to-cell temperature difference remain within the optimal range. The transient thermal response of each battery cell is characterised by calculating the settling time of the average battery cell surface temperature and the maximum overshoot. Further, the classical system dynamic definitions are utilised. Tay et al. [159] describe the settling time as the time needed for a system to reach and stay within a two percent range of the final equilibrium value. Whereas Ogata [160] defines the maximum overshoot as the ratio of the peak value of the system response to the desired value of the system response.

The spatiotemporal response of the temperature field to a linear ramp using the SC03 drive cycle in the internal heat generation is shown in Figure 5-4. Figure 5-4a shows the temperature field during steady-state conditions before introducing the SC03 ramp. It should be noted that the simulations were allowed to run for 15 seconds under steady-state conditions before introducing the ramps, which can also be seen in the figures showing the average battery cell surface temperatures, such as Figure 5-5. From Figure 5.4a, it can be seen that the temperature of the fluid and solid (battery cells) is nearly indistinguishable due to the small internal heat generation. However, as the simulation reaches a time of 50 seconds, the temperature difference between the two regions is far more apparent, as observed in Figure 5-4b. Figures 5-4c and 5-4d show the temperature field after 100 seconds and at the end of the simulation – once the model has reached its' new steady-state condition – at 300 seconds. Figure 5-4 depicts a conventional convective system; as the fluid travels further downstream, the fluid temperature begins to approach that of the battery cells. This phenomenon can be clearly seen in Figure 5-4d, where cells closer to the outlet exhibit larger temperatures than those at the inlet.

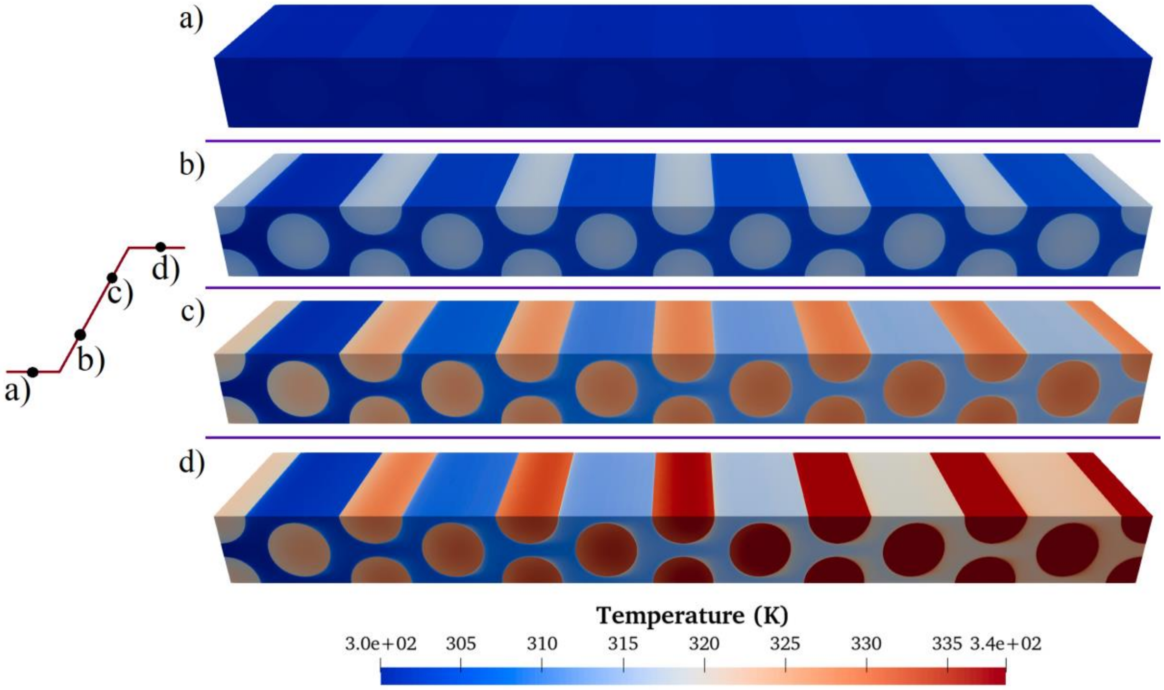

Figure 5-4 – 3D Spatiotemporals of the temperature field due to linear ramp using the SC03 drive cycle. Different stages of the temperature field a) 15 s – prior to ramp, b) 50 s, c) 100 s, and d) final steady state condition (300s). $Fluid = Water$.

5.6.1 *Linear ramps*

Figures 5-5a and 5-5c depict the transient response of the battery cell’s average surface temperature to internal heat generation ramps based on the NYCC1 and NYCC2 with air as the coolant fluid, respectively. As previously stated in Section 5.1, the lower limit of each internal heat generation ramp was set to 2,000 W/m^3 and using the speed-time data from Figure 5-2a, the upper limit of the NYCC1 ramp was calculated to be 47,400 W/m^3 with a duration of five seconds. It can be clearly seen that the temperature of the battery cells continues to increase even after the ramp has finished due to the time taken for the heat to conduct to the battery cells’ surface. Further, each battery cell’s overall temperature increase after reaching the new steady-state condition differs from the starting temperature differences. This can be attributed to the behaviour of a typical convective system. As the fluid flows towards the outlet, its’ temperature begins to reach that of the battery cells surface, diminishing the amount of heat being transferred to the fluid and increasing the time for the battery cells to cool down. The increase in the settling time is also due to the fluid heating up as it flows further downstream. A detailed analysis of each battery cell’s setting, heating, and cooling time is given later.

The temporal average surface temperature response of each primary battery cell to the NYCC1 and NYCC2 ramps in the internal heat generation on each battery with water as the coolant fluid are given in Figures 5-5b and 5-5d, respectively. The observed differences between the two fluids are due to the significant differences in their thermophysical properties. Unlike air, the water temperature responses contain no overshoot. The significant difference in the specific heat capacity of the two fluids allows water to retain a far higher amount of energy before an increase in temperature can be recorded. This allows water to remove larger quantities of heat from the surface of each battery cell. This also explains each battery cell's far lower and tighter starting temperatures in the water cases.

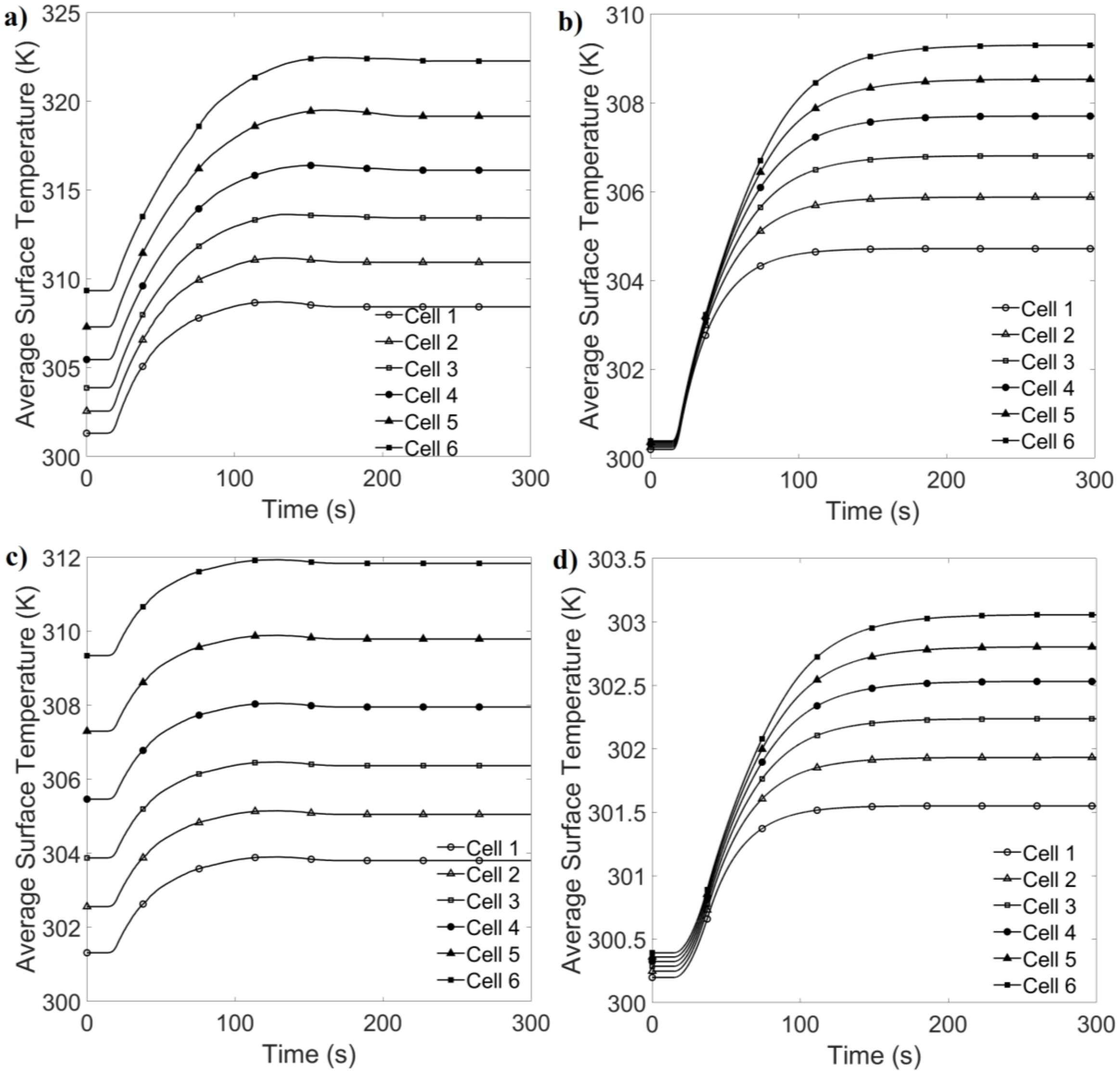

Figure 5-5 – Average battery cell surface temperature due to internal heat generation with air (left) and water (right) as the coolant fluids. a) and b) NYCC1, c) and d) NYCC2.

Furthermore, a much larger and steeper ramp was found using the data shown in Figure 5-2b – the SC03 drive cycle. The upper limit for this drive cycle was calculated to be 196,750 W/m^3 with a total ramp duration of 14 seconds. This results in the SC03 internal heat generation being amplified by over four times as compared to NYCC1 in less than three times the duration and almost 13 times compared to NYCC2. Thus, the SC03 ramp generates higher battery temperatures, as shown in Figure 5-6. As expected with any convective system, as the fluid flows downstream, the battery cells at the outlet experience higher temperatures than those at the inlet. Although the general trend of Figure 5-6 is the same as those shown in Figure 5-5, due to the significant increase in internal heat generation, the average surface battery cell temperatures are also higher. Comparing the temperature differences for the NYCC1 and SC03 ramps leads to no apparent correlation between the two data sets. This is to say that increasing the upper ramp limit by four does not produce a temperature difference of the same magnitude. The trend of increasing settling time for the battery cells at the outlet between the two drive cycles can be seen. However, due to the significant differences between the ramps, battery cells influenced by the SC03 ramp require a longer settling time.

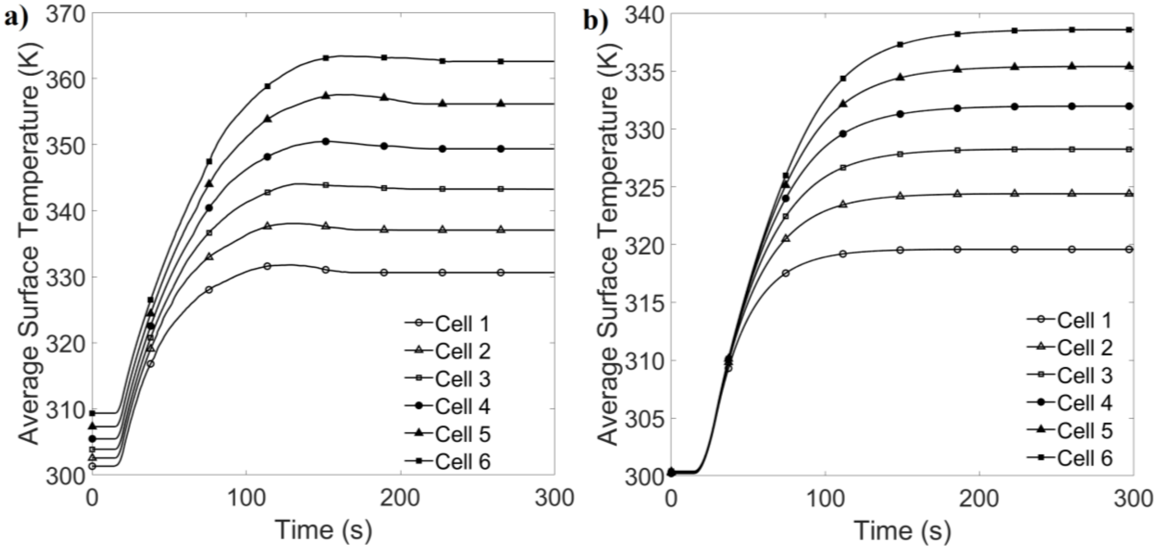

Figure 5-6 – Average battery cell surface temperature due to internal heat generation with a) air and b) water using the SC03 drive cycle ramp.

Figure 5-7 shows each battery cell's average surface temperature temporals to ramps in the internal heat generation using the UDDS drive cycle. The left column is for air, and the right is for water. The UDDS1 ramp leads to results almost identical to the NYCC1 ramp. This is due to the upper limit of the UDDS1 ramp being 51,700 W/m^3. However, the ramp duration for the UDDS1 ramp is 11 seconds – more than double that of NYCC1. In comparison, the upper ramp limit for UDDS2 is 37,800 W/m^3 with a ramp duration of seven seconds. The larger internal heat generation limit for the UDDS1 ramp leads to higher overall temperatures and more prominent peaks; however, the settling time of each battery cell decreases due to the more considerable ramp duration. This indicates that a longer ramp duration for an almost identical upper ramp limit leads the thermal system to react faster to achieve stability. This can be attributed to the thermal system's ability to manage heat release through convection as the internal heat generation increases. Conversely, cases with a significantly large heat release in short periods would cause a sharp increase in the average battery cell surface temperature, resulting in considerable time required to reach the new equilibrium state, matching the behaviour observed in Figures 5-5a, 5-5c, 5-6a, 5-7a, and 5-7c.

Comparing the results of the two coolant fluids for any drive cycle ramp leads to the expected outcome; water is far more effective at achieving lower temperatures and a tighter spread. The two responses are shown in Figures 5-5a and 5-5b, where the NYCC1 ramp is used, water as the inlet coolant leads to the hottest battery cell being over 30% cooler without any correction due to overshooting and reaching this state over 25% faster than air. Furthermore, the recommended battery cell operation temperature is between 298 K and 318 K [161], and the maximum cell-to-cell temperature difference should be 5 K [27]. The case of NYCC1 with water achieves both conditions, whereas air fails to sustain the safe operating parameters. However, changing the ramp to the SC03 drive cycle, both fluids fail to achieve the safe operating parameters for the battery cells. Comparing Figures 5-6a and 5-6b, a decrease of 33.8% for cell one and 28.2% for cell six can be observed when changing the coolant fluid from air to water. Further, changing the ramp case from NYCC1 to SC03 increases the settling time of the battery cells due to a significant increase in internal heat generation.

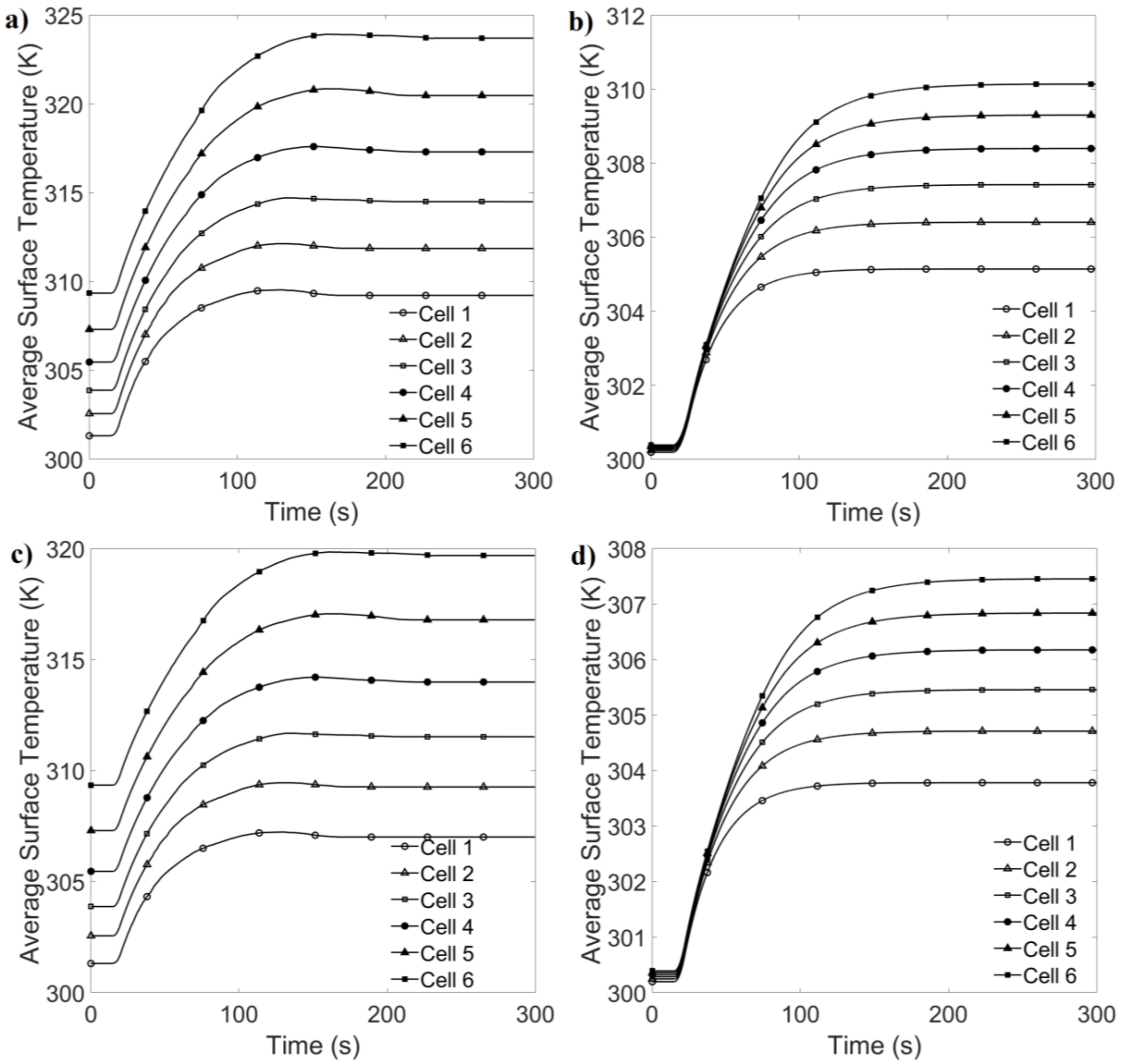

Figure 5-7 – Average battery cell surface temperature due to internal heat generation with air (left) and water (right) as the coolant fluids. a) and b) UDDS1, c) and d) UDDS2.

Figure 5-8 shows the values of the dimensionless setline time for all primary cells. The dimensionless setline time is calculated using the following equation:

$$dimensionless\ settling\ time\ (DST) = \frac{settling\ time}{ramp\ duration} \tag{5.5}$$

where the settling time is the time taken to reach two percent of the final value [159]. Figure 5-8 shows downstream battery cells experience a higher DST value than those near the inlet. This is expected since the fluid temperature increases as it travels downstream, necessitating a longer time to extract heat from the battery cells. Additionally, the simulations in which air was used as the coolant fluid always produced a higher value of DST than water. The air simulations are observed to have a steady increase in their value of DST, whereas DST for the water simulations jumps from cell two to three before having a general increase. Figure 5-8 shows that the transient response of the battery module to long durations always produces lower values of DST. Conversely, shorter ramp periods tend to produce more significant values of DST. The physical origin of the delay in response to heating in the present study is heat conduction due to ramps being imposed on the internal heat generation inside the solid battery cells. It is well acknowledged that conduction is the slowest form of heat transfer compared to other forms of heat transfer – convection and radiation [158]. The results in Figure 5-8 indicate that short ramp durations, such as the NYCC1 case, release significant amounts of heat within the system very quickly, not permitting enough time for the heat to be conducted from the body of the battery cells to their surfaces effectively. As a result, higher values of DST are produced. Conversely, long ramp durations, such as the NYCC2 case, have sufficient time to conduct the heat to the battery cell’s surfaces before convecting, producing smaller values of DST. This implies that fluctuations in the battery cell’s internal heat generation over long periods will allow enough time for the system to react to these changes far quicker. However, short-term disturbances will require far longer for the system to stabilise.

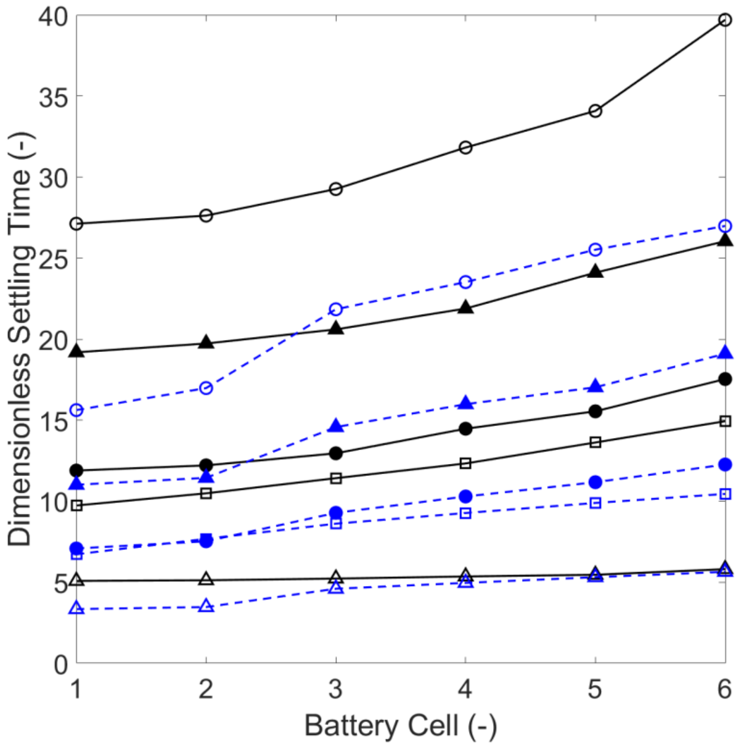

Figure 5-8 – Dimensionless Settling time of each battery cell using different drive cycle ramps: NYCC1 (○), NYCC2 (Δ), SC03 (□), UDDS1 (●), and UDDS2 (▲). $Fluid = Air\ (black)\ and\ water\ (blue)$.

Moreover, Figures 5-9a and 5-9b show the maximum battery cell temperature against the dimensionless settling and heating time, respectively, where the latter is defined in Eq. (5.6).

$$\begin{aligned} &\mathit{dimensionless\ heating\ time}\ (DHT) \\ &\qquad = \frac{\mathit{time\ taken\ to\ reach}\max \mathit{temperature}}{\mathit{ramp\ duration}} \end{aligned} \tag{5.6}$$

It should be noted that the water simulations produce no overshoot. Thus, these simulations take longer to reach the maximum temperature than the air simulations, as shown in the average surface temperature graphs. Air simulations produce higher maximum temperatures due to their inferior thermophysical properties than water, which is also why air simulations have a higher temperature spread between each cell. As discussed in Figure 5-8, the air-cooled models take longer to stabilise than water; therefore, their values of DST are higher. An observation from Figure 5-9 is that the air simulations produce results with a steep gradient, whereas the water simulations results have a far smaller gradient. This can be explained by the significant difference in thermophysical properties of the two fluids, which impact the degree of the reported DST and DHT. Air having far lower thermal conductivity and capacity, each battery cell would rise to its maximum temperature far quicker, producing an almost vertical line in the maximum battery cell temperature vs DST or DHT. Whereas water's large specific heat capacity allows it to retain more heat energy before experiencing a temperature rise.

Moreover, since the water results produce no overshoot, the maximum temperature reported by these results is the final steady-state temperature. Therefore, the water simulations generate a primarily horizontal trend line for the battery cell's maximum temperature vs DST or DHT. The only exception is the SC03 ramp case due to its significantly massive internal heat generation. Two horizontal temperature lines are used to infer the safe operating temperatures. Li-ion battery cells' maximum safe operating temperature is between 308 K and 318 K, depending on the literature [55, 161]. Therefore, it can be safely stated that battery cells below 308 K are always safe – such as those cooled using water. Battery cells between 308 K and 318 K can be considered safe – such as the first four cells in the NYCC1, UDDS1, and UDDS2 while using air as the coolant. Battery cells above 318 K will always operate outside the optimal range, such as the SC03 case with either coolant fluid.

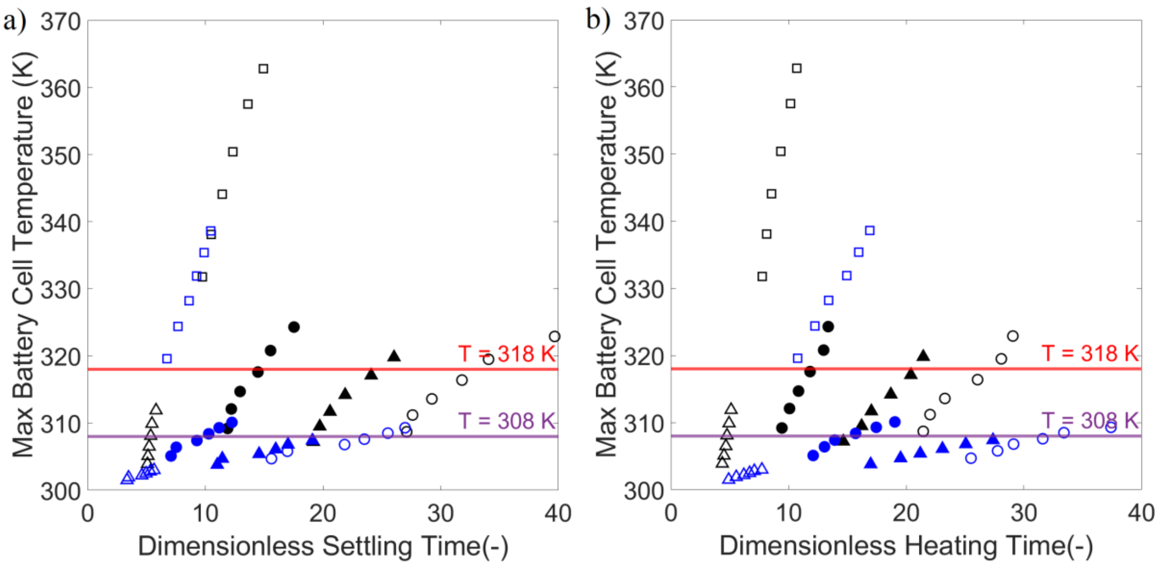

Figure 5-9 – Maximum battery cell surface temperature vs a) Dimensionless settling time and b) Dimensionless heating time of each battery cell using different drive cycle ramps: NYCC1 (○), NYCC2 (Δ), SC03 (□), UDDS1 (●), and UDDS2 (▲). $Fluid = Air\ (black)\ and\ water\ (blue)$.

5.6.2 *Single cycle segments*

The temporal response of the average battery cell surface temperatures to modulation in the internal heat generation ramps using the SC03 single-cycle segment is shown in Figures 5-10a and 5-10b for air and water, respectively. The total duration of this segment is 40 seconds. It can be seen that even after this segment is finished, the average surface temperature continues to increase, reaching a peak before decreasing and reaching a temperature similar to that prior to the segment. The steady-state condition for these figures was set so that if the overall temperature change over 10 seconds were less than one percent, the temperature would be considered stable, and the simulation would end. Therefore, even though the final temperatures are not equal to the starting temperatures, they are considered steady. The water single-segment case is far quicker to react to the change in the internal heat generation; as a result, the peak temperature of each battery cell occurs earlier and at a lower temperature than for the air case. The change in temperature for cells one and six – with air as the coolant – is 22.58 K and 31.33 K, respectively. Whereas changing to water as the coolant, the temperature difference for the same cells is 15.27 K and 21.49 K. Thus, water is far better at maintaining an overall cooler temperature of the battery cells; in particular, the average surface temperature of battery cells one and six is 32.3% and 31.5% lower, respectively. The superior thermophysical properties of water allow it to react 34% faster for cell one and 9.8% faster for cell six.

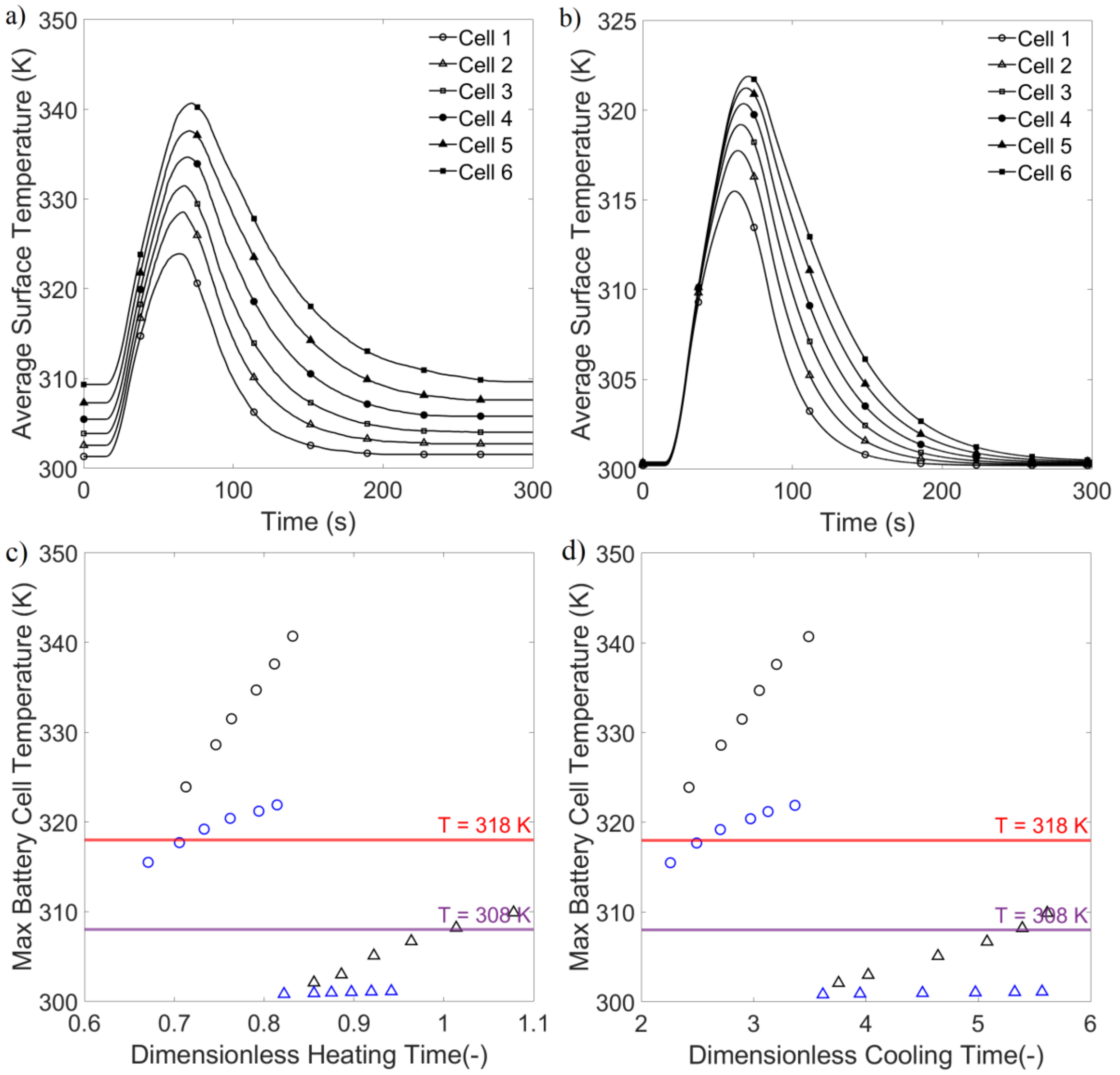

Figure 5-10 – Average battery cell surface temperature using the SC03 single segment internal heat generation ramp with a) air and b) water as the coolant fluids. Maximum battery cell surface temperature vs c) Dimensionless settling time and d) Dimensionless heating time of each battery cell using different single cycle segments: NYCC (Δ); SC03 (○), $Fluid = Air\ (black)\ and\ water\ (blue)$.

Furthermore, the maximum battery cell surface temperature vs dimensionless heating and cooling time are given in Figures 5-10c and 5-10d. Here, the dimensionless cooling time (DCT) is defined as the ratio of the time the battery cell takes to reach the final steady-state condition after peaking and the ramp duration. As anticipated, the results of the dimensionless heating time for water are far more compact than that of air. In Figures 5-10c and 5-10d, the NYCC single-cycle segment with water as the coolant fluid produces an almost horizontal trend line. This is due to the slight increase in internal heat generation over a prolonged period allowing the thermal system to accommodate variations in the average surface temperature. Figures 5-10a and 5-10b show that the heating phase of the SC03 segment is far smaller than the cooling phase, which can be attributed to the delay in responding to changes in the internal heat generation. As the positive gradient in the internal heat generation ends, and the negative gradient ramp begins, the surface temperature of the battery cells continues to increase until all excess heat is washed away. This causes the DHT to have a graph scale of 0.6 to 1.1, whereas the DCT axes range from 2 to 6. Further, similar to Figure 5-9, two horizontal temperature lines indicate the safe operating range of the battery cells. As expected, the substantial amount of internal heat generated by the SC03 drive cycle results in the battery module being outside the safe operating range. However, the first two battery cells can be considered safe when using water as the coolant fluid. Further, the minor increase in the internal heat generation from the NYCC single-cycle segment causes all battery cells to remain within the safe operating temperature range regardless of the coolant type.

5.7 *Conclusions*

The operating temperature of the battery cells is directly impacted by the range of temporal scenarios caused by the vast array of driving patterns and vehicle manoeuvres. Therefore, effective battery thermal management systems must be able to predict the battery cell's temperature during these driving scenarios. Such predictions are trivial for simple systems with steady parameters. However, such predictions become intractable when real-time driving data is utilised, during which the battery cells are rarely in steady-state scenarios. In this chapter, three different drive cycles were numerically analysed to find the points at which the battery cells experience extreme thermal loads – such as very high acceleration in a short period. The system response was modulated using linear ramps and single-cycle segments of internal heat generation. The consequent response was examined by analysing the battery cell's average surface temperature. The simulation results of the two different fluids, air and water, were compared in the time domain. The key findings of this study can be summarised as follows.

- Using air as the coolant fluid resulted in all ramp cases producing a delayed system response and was far slower at reaching the new steady-state condition. However, smaller DST values were produced using the same ramps for cases with water. Therefore, it is essential to analyse the battery cell response to understand each battery cell's transient thermal behaviour.

- The ramp duration directly impacts the response of each case. Cases with a large ramp in a short period (NYCC1 – 2000 to 47,400 W/m^3 in five seconds) produce high values of DST and create a sharper rise in DST per battery cell.
- In most cases, using water as the coolant fluid leaves the battery cells within their safe operating range.
- Water simulations tend to produce results with a small gradient. In contrast, air produces results with a steeper gradient for the maximum battery cell temperature vs DST or DHT.
- The fluid properties of water allow it to maintain a minimum overall battery cell temperature change and reduce the cell-to-cell temperature differences.
- The water single-cycle segment cases react as much as 34% faster to temporal changes in the internal heat generation than air.

Chapter 6. Harmonic axial vibrations of a Li-ion battery cell

The most effective mode for a battery thermal management system is active cooling. This means the BTMS can predict the behaviour of the battery module/cell and regulate the coolant system for enhanced system performance and safety [162, 163]. However, predicting the transient behaviour of a battery cell is easier said than done; the complex and erratic driving behaviour of EVs makes the problem burdensome.

The battery cells and the thermal management system are inherently exposed to vibrational excitations due to acceleration, deceleration, and road roughness. Although the vibrations are fundamentally random, they are influenced by the vehicle's suspension system and settings. Therefore, this study aims to further our understanding of Li-ion battery cells' behaviour to mechanical vibrations. This is done by numerically evaluating the unsteady thermal response of a battery cell to forced vibrations at numerous modulation frequencies and amplitudes. The battery cell is modelled using cell dimensions from other studies. The impact of different coolants – air and water – on the battery cell thermal output is also considered. Although the vibrational properties of the battery cell vary radically depending on the vehicle type, driving and environmental conditions, and road roughness, the vibrational frequencies are typically situated within 10 to 30 Hz [68]. The numerical results are compared against existing correlations and numerical and experimental data from the literature for rigorous validation. The Nusselt number output is analysed in the time and frequency domains to better understand a battery cell's thermal behaviour to transient inputs. A visual representation of an EV driving on an uneven surface, vibrating the battery cells inside a battery module, is shown in Figure 6-1.

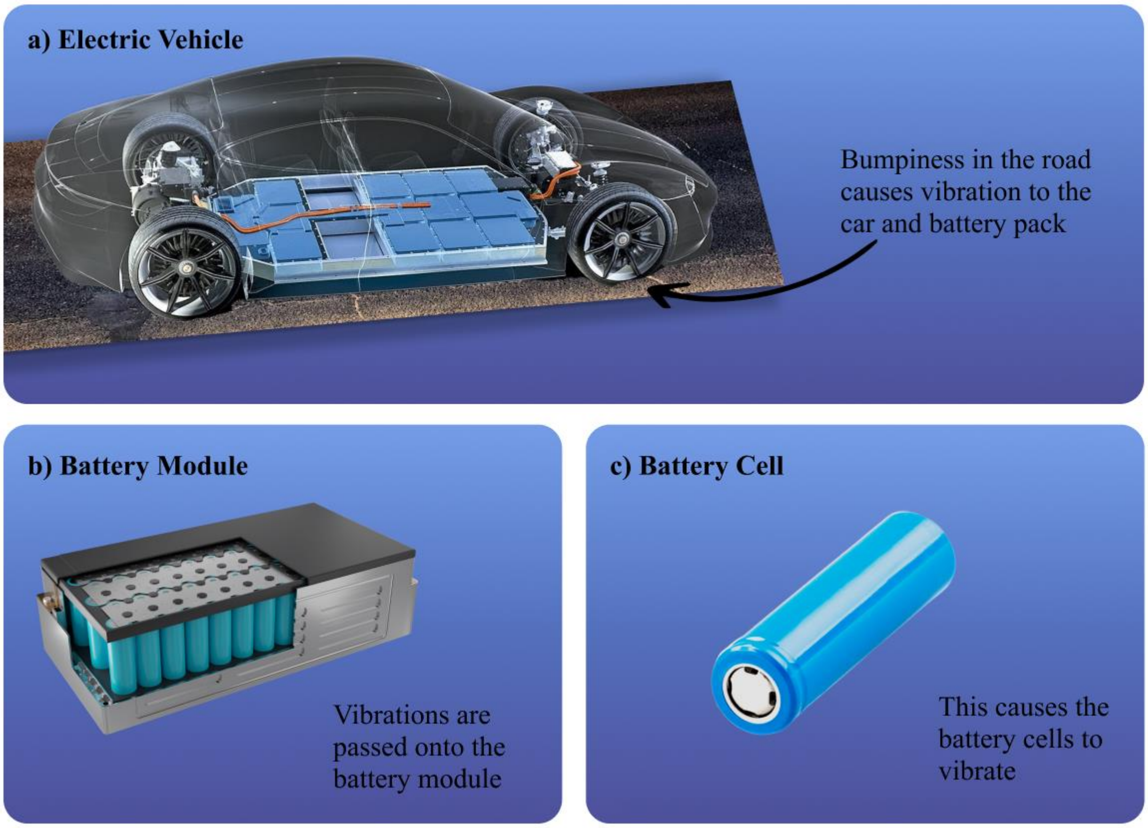

Figure 6-1 – Visual representation of a battery cells vibration source.

6.1 *Model configuration and assumptions*

Figures 6-2a and 6-2b show the battery cell model schematic and the numerical model used during simulations. The numerical model has a total length, L, of 50D, where the inlet and outlet are 10D upstream and 40D downstream from the centre of the battery cell [164, 165]. The model's total height, H, is 12D, with the top and bottom boundaries equidistant from the centre. Moreover, a wake region of height 5D is generated around the battery cell leading to the outlet to capture the Karman street vortex accurately [166]. The battery cell has a radius of 20 mm [66]. The following assumptions are made throughout the analysis.

- The fluid flow is fully turbulent with a steady inlet velocity.
- The ideal gas and constant density models are used for cases with air and water, respectively.
- The fluid is thermally and hydrodynamically fully developed.
- Gravitational effects are ignored.

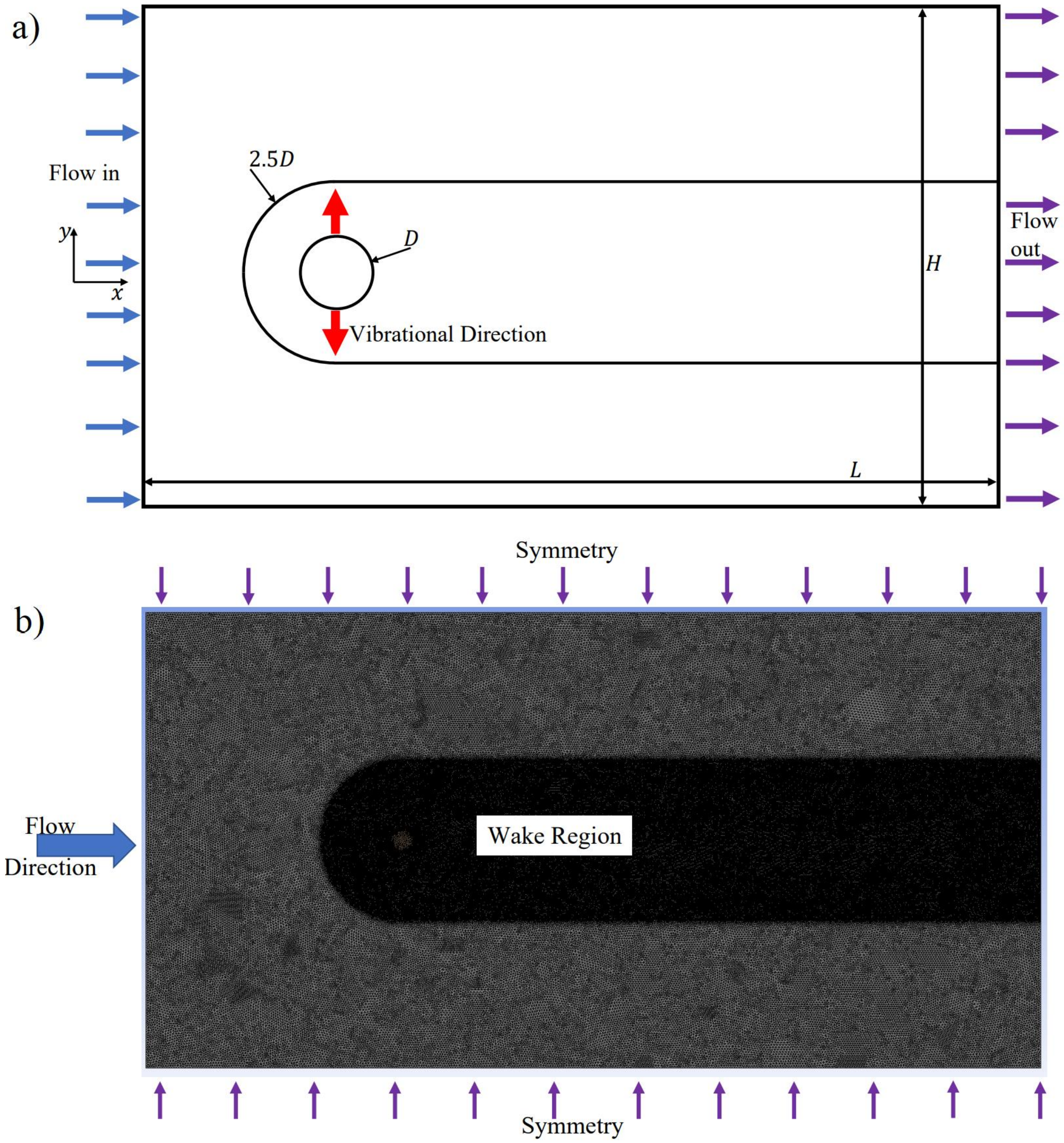

Figure 6-2 – a) Battery cell model schematic, b) Numerical model.

The battery cell modulations are applied to the numerical model once it has reached steady-state conditions. Heat generated inside each battery due to current withdrawal travels to the surface of the battery cell prior to being washed away by the cooling fluid. Thus, the heat generated inside the battery cell is modelled using a volumetric heat source, S_c, [110, 141, 142] as defined in chapter 3. The primary sources of this heat generation are defined later in section 6.2.

The following set of boundary conditions were applied to the numerical model. Since the numerical model can be expanded into the y-direction, the top and bottom walls are under a symmetry condition. A no-slip condition is given to the surface of the battery cell. The fluid-solid (battery cell) interface contains two boundary conditions. First, the temperature of the fluid, f, and the solid, s, are equal, $T_f = T_s$. Second, the heat flux leading the battery cell and entering the fluid domain is equal but opposite, $q_f'' = -q_s''$. Finally, the inlet fluid temperature is set to 300 K, and the outlet is treated as an atmospheric pressure outlet.

The steady-state conditions were achieved by setting the vibration frequency and amplitude to zero. The battery cells' internal heat generation was set to 48,000 W/m^3, extracted from the Multi-Scale-Multi-Domain (MSMD) battery simulation – see Section 6.2 for more detail. The air's poor thermal conductivity and capacity demands high fluid velocities for ideal operation [167]. Therefore, the inlet fluid velocity for air was 2.5 m/s (Re = 6,300) based on Refs. [36, 54]. The Reynold number for water was found to be 2,300 based on previous studies [114–116]. The Reynolds numbers are kept constant throughout the study. At a Re value of 6,300, the Gr was calculated to be 337,457.67. Using Eq. (3.12a), this results in a Ri of 0.0085. Sine the calculated value of $Ri < 0.1$, gravitational effects were safely ignored. A total of three vibrational frequencies and three amplitudes of modulation are applied to the numerical model, leading to a total of nine cases for each coolant fluid. The vibration frequencies of 10, 20, and 30 Hz were chosen based on previous studies [69, 70, 72] and per the UN ECE R100 standard, a European standard for testing EV Li-ion batteries for road safety [71]. The modulation amplitudes of 30, 40, and 50 mm/s were selected based on Refs. [68, 70, 72].

Ansys Fluent 2020-R2, a finite-volume-based CFD software, was used for numerical analysis. A conjugate heat transfer (CHT) model was utilised to simulate the conductive and convective heat transfer. A two-dimensional, unsteady, turbulent flow solver coupled with the energy equation and the realisable $k - \epsilon$ turbulence model was used. The MSMD battery model was employed to simulate the realistic response of a battery cell to a given load, and the consequent thermal characteristics were exported and imported into the CHT model. The timestep was set to be six orders of magnitude smaller than the full-time scale to satisfy the CFL condition and accurately model vortex shedding [144]. Due to this study's complex and computationally demanding nature, it was conducted on an HPC called ARCHIE-WeSt using an Intel Xeon Gold 6138 Skylake series processor. The single node of this processor consisted of 40 cores. The numerical data was exported to ParaView 5.10.1 for visualisation and MATLAB 2022a for post-processing.

6.2 *MSMD battery model*

The multi-domain and multi-physics nature of Li-ion battery cells makes accurate modelling extremely challenging – the unique physics of batteries due to different length scales makes the problem convoluted [168]. During the thermal analysis of Li-ion batteries, the objective was to determine the heat generation, heat dissipation, and temperature distribution at the battery length scale. Moreover, the transport of ions occurs at the anode, cathode and separator layers, whereas transport in the active material occurs at the atomic level [169, 170]. Therefore, the MSMD battery model was utilised to simulate the physics throughout each domain of a battery cell. The MSMD battery model, in conjunction with Newman's pseudo-two-dimensional (P2D) model, is an electrochemical-thermal model coupled with mass, charge, energy conservation, and electrochemical kinetics. This results in a comprehensive model for accurately evaluating the thermal behaviour of a battery cell [84].

The Butler-Volmer equation is used to define the local charge due to current density [169]

$$j_n = j_0 \left\{ exp\left(\frac{\alpha_a F}{RT}\eta\right) - exp\left(\frac{\alpha_c F}{RT}\eta\right) \right\} \tag{6.1a}$$

where j_o and η are defined by

$$j_0 = F k_0 c_1^{\alpha_a} \left(c_{s,max} - c_{s,surf}\right)^{\alpha_a} c_{s,surf}^{\alpha_c} \tag{6.1b}$$

$$\eta = \phi_s - \phi_e - U_{eq} \tag{6.1c}$$

Ohm's law as a function of current and potential gradients describes the charge conversation. Therefore, the transfer of ions in the electrolyte can be expressed using the Nernst-Planck equation [169].

$$\frac{\partial}{\partial x}\left(k_e^{eff}\frac{\partial}{\partial x}\phi_e\right) + \frac{\partial}{\partial x}\left(k_{D,e}^{eff}\frac{\partial}{\partial x}ln(c_e)\right) + j^{Li} = 0 \tag{6.2}$$

whereas the change in the solid domains is restricted to Ohm's law.

$$\frac{\partial}{\partial x}\left(k_s^{eff}\frac{\partial}{\partial x}\phi_s\right) = j^{Li} \tag{6.3}$$

Finally, heat generation due to electrochemical reactions within Li-ion batteries can be summarised into three primary sources [84]: an electronic-ohmic heat source, S_e, a reaction current heat source, S_r, and an ion-ohmic heat source, S_i. These three sources are defined in Eq. (6.4).

$$S_e = I^2 \frac{R_c}{A}, \tag{6.4a}$$

$$S_r = A \int_x^{x+dx} j^{Li}\left(\phi_s - \phi_e - U_{eq}\right) dx, \tag{6.4b}$$

$$S_i = A \int_x^{x+dx} \left[\sigma_s^{eff}\left(\frac{\partial \phi_s}{\partial x}\right)^2 + k_s^{eff}\left(\frac{\partial \phi_e}{\partial x}\right)^2 + k_{D,e}^{eff}\left(\frac{\partial ln(c_e)}{\partial x}\right)\left(\frac{\partial \phi_e}{\partial x}\right)\right] dx. \tag{6.4c}$$

The battery cell parameters used during analysis are shown in Table 6-1, which can be found in Refs. [171, 172] or are based on the 85 kW Tesla Model S battery specifications [111].

Table 6-1 – Battery cell parameters.

Battery type	Samsung 26FM-PCB 18650 Li-ion battery
Nominal battery cell capacity	2600 mAh
Nominal supply voltage	3.6V
Maximum charge voltage	4.2V
Minimum discharge voltage	2.2V
C-Rate	1C

6.3 *Comparison at the forcing frequency*

The numerical data is analysed in the frequency domain using the FFT function in MATLAB 2022a. The dynamic thermal response of the battery cell is predicted by comparing the amplitude of the output signal and the forcing frequency. This comparison is conducted by first normalising the Nusselt number temporals using Eq. (6.5).

$$Normalised\left(Nu(t)\right) = \frac{Nu(t)}{\overline{Nu}} \tag{6.5}$$

where $Nu(t)$ is the Nusselt number at the current time and $\overline{Nu}$ is the time-averaged Nusselt number. The amplitude at the forcing frequency was found using the following relation.

$$amp(f) = \left|Normalised\left(Nu(t)\right)\right| \tag{6.6}$$

Moreover, cross-correlation was used measure the time delay between the output and the input signal. The time delay was then non-dimensionalised [122],

$$ndd = \frac{t_d}{L_c/u} \tag{6.7}$$

where ndd is the non-dimensional delay, and t_d and L_c are the cross-correlation time delay and the length from the fluid inlet to the battery cell, respectively. The phase difference of the signal at the forcing frequency (in radians) was found using t_d.

$$phase = 2\pi f t_d \tag{6.8}$$

However, during analysis, the non-dimensional delay was used to show the phase.

6.4 *Grid independency study*

The mesh on the entire model is made using an unstructured triangular method. Figure 6-2 shows that the fluid domain is split into two zones – a far field zone and a wake region – for greater mesh control. A larger cell size of 0.004m is used in the far field to reduce the overall number of cells, thus, saving computational resources without impacting the accuracy of the numerical model. In the wake region, a finer mesh was used to model fluid flow accurately and the formation of vorticities, improving the numerical analysis. Eight tests were performed at a fixed Re of 4,000, as shown in Table 6-2. The cell size was systematically varied to determine the overall grid with the best accuracy and minimal computational impact. Once the Nu of the battery cell's surface fell within a band of one percent, the grid independency would be achieved. As evident from Table 6-2, as the cell size is decreased, the absolute change in Nu decreases. As a result, a cell size of 0.0015 was chosen to optimise the numerical performance of the model further.

Table 6-2 – Grid Independency Tests.

	Cell size (m)	Number of cells	Absolute change in Nu (%)
Test 1	0.01	107,525	---
Test 2	0.008	178,881	8.98
Test 3	0.006	232,937	8.21
Test 4	0.004	411,117	4.99
Test 5	0.003	693,852	1.89
Test 6	0.002	903,522	1.05
Test 7	0.0015	1,978,946	0.88
Test 8	0.001	6,803,577	0.20

6.5 *Validation study*

The validation study was conducted by comparing against existing numerical and experimental data. Three types of validation studies were carried out: steady validation, unsteady validation, and battery model validation. For the first study, the battery cell was fixed, and the coolant fluid and fluid velocity were systematically varied. Vibration was introduced on the battery cell in the second study. The MSMD battery model was activated during the final study. The outcomes of the three validation studies can be seen in Figures 6-3, 6-4, and 6-5, respectively. A comparison of the numerical model against the empirical correlations by Churchill and Bernstein [123] and Hilpert [125] with the fluid type being air, is shown in Figure 6-3a. When the value of Re is in the laminar range, the numerical model yields excellent agreement with the correlations. As the value of Re increased, the error also increased, with the highest error being 8.18% at a Re of 20,000. However, the highest error from Figure 6-3a is still within acceptable error margins since the correlations have errors as high as 20% [123]. Additionally, the simulated drag coefficient, C_d, was compared against the experimental data by Patel [124]. At a Re of 3,900 and the fluid being air, the simulation produced a value of 0.9115, whereas the experimental data reached 0.93 ± 0.005, an error of less than two percent.

The comparison of the water numerical model against the empirical correlation by Churchill and Bernstein [123] and the experimental data by Whitaker [126] are shown in

Figure 6-3b and 6-3c, respectively. As anticipated, at low values of Re, the current simulation model and the numerical/experimental data yield similar values. In Figure 6-3b, the most significant error of 7.62% was found at a Re of 8,000 and 10,000. The experimental comparison found the most significant error of 3.72% at a Re of 2,000. Additionally, in Figure 6-3c, all errors were below four percent.

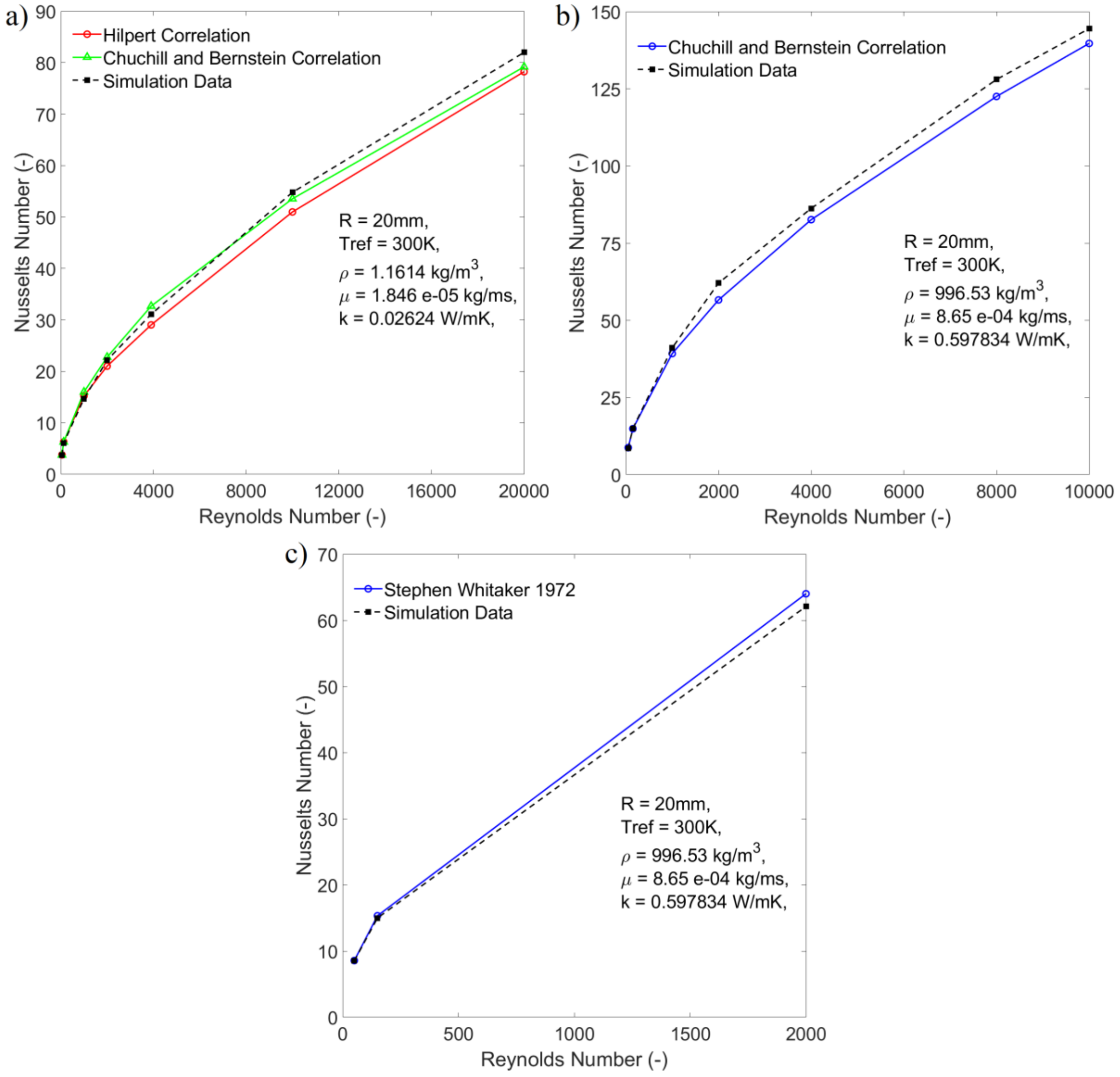

Figure 6-3 – Steady validation study. a) air model vs Refs. [123, 125], b) water model vs numerical data [123], and c) water model vs experimental data [126].

The unsteady validation study is shown in Figure 6-4, where Fiure 5-4a and 5-4b compare the mean drag coefficient, C_d, against the frequency ratio and the mean Nu against the vibrational amplitude, respectively. The movement of the cylinders are captured using a re-mesher – during each timestep, the cylinder moves according to the set modulation amplitude and frequency. During each movement, the mesh is regenerated around the cylinder using the controls mentioned in Section 6.4. This allows for enhanced accuracy by ensuring that the mesh cells stay the same. Here, the frequency ratio, F, is the ratio of the forced oscillation frequency, F_0, and the Strouhal frequency, $F_s – F = F_0/F_s$. At $F = 0$, the vibration is zero, Placzek et al. [173] provide an C_d value of 1.37, whereas the simulated C_d was found to be 1.35, leading to an error of 1.45%. At an $F = 0.9$, $F = 1.0$, and $F = 1.1$, the most significant error of 4.85% is found at a frequency ratio of 1.0. In Figure 6-4b, the dimensionless vibrational amplitude is defined as the vibrational amplitude divided by the inlet velocity. At $V_{amp} = 0$, no vibration, Karanth et al. [174] state a Nusselt number of 8.47, where the numerical model achieves 8.44, leading to an error of just 0.35%. The minute error at no vibration is expected due to the low value of Re, as evident from the steady validation in Figure 6-3a. Once the vibration is activated, the error increases but remains small, with the highest error being 0.45% at $V_{amp} = 0.5$ against Fu and Tong [175].

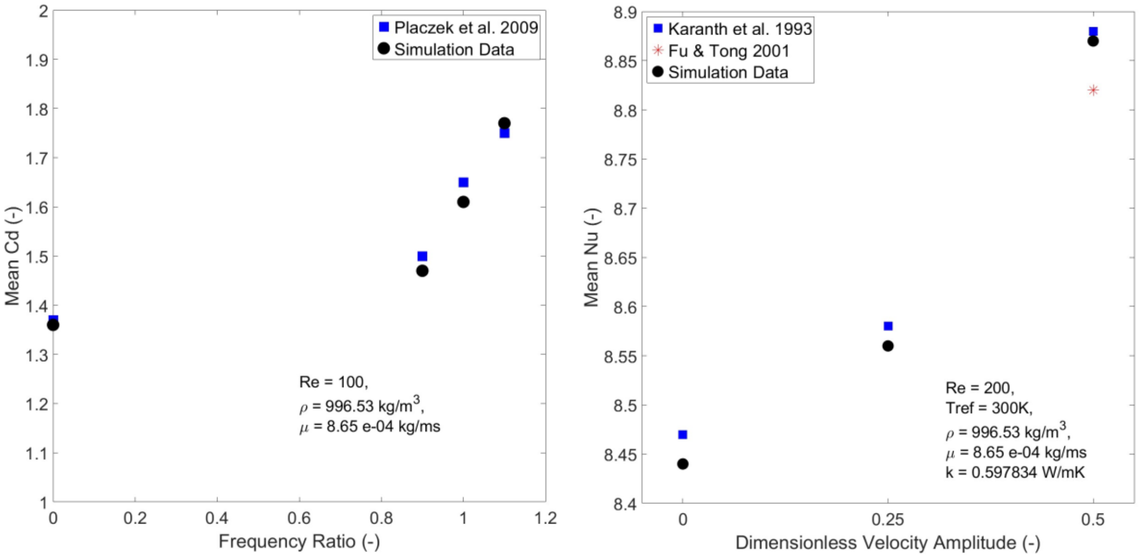

Figure 6-4 – Unsteady validation study. a) mean drag coefficient vs Ref. [173], b) mean Nusselt number vs Refs. [174, 175].

The MSMD and the Newman P2D battery model validation is shown in Figure 6-5. Comparing the average battery surface temperature at two different discharge rates of the simulated model and the data presented by Shukla et al. [69] are in close agreement. The most significant error of 2.9% is found in the 2C comparison; however, this error is reduced as the simulation progresses to a full battery discharge.

The rigorous validation studies and the excellent agreement amongst the simulated results and the empirical correlations, numerical and experimental data of the two fluids confirm the validity of analysis in this study.

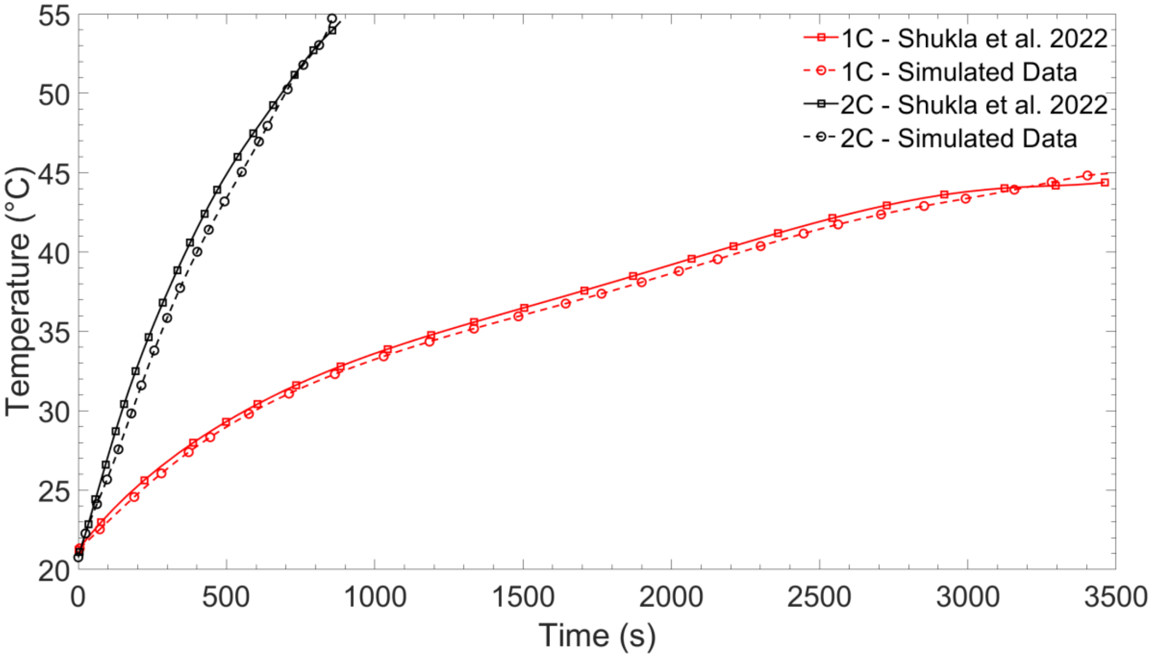

Figure 6-5 – Battery model validation. Cylindrical battery surface temperature at discharge rates of 1C and 2C vs Ref [69].

6.6 *Computational optimisation*

Numerical simulations of a turbulence model with a refined mesh can be a computationally expensive task. Further, including the MSMD and the Newman P2D models with vibrational loads makes the simulations exceptionally computationally demanding. This might be the reason for a lack of CFD investigations on this problem. Hence, computational optimisations are of utmost importance. Therefore, the MSMD and the Newman P2D battery models were run alone, and the consequent temperature and heat generation data was exported into a CHT model. Furthermore, three-dimensional and two-dimensional simulations were conducted and compared. The former results are shown in Figure 6-6a, where both simulations were run at a Re of 2,300, with water as the coolant fluid, a vibrational amplitude of 30 mm/s, and a vibrational frequency of 10 Hz. It can be clearly observed that importing the thermal data from the battery model simulations has an insignificant impact on the Nusselt number. However, the computational resources are significantly improved by eliminating the battery models. In Figure 6-6a, an error of 0.7% was found at the peaks and troughs of each modulation. Furthermore, comparing the amplitudes of the battery model on vs off simulations leads to an error of 16.7%. However, removing the battery models from the simulation always underestimates the Nusselt number, making the errors acceptable at the gain of significantly improving the computational costs. The comparison of the three and two-dimensional models is shown in Figure 6-6b, where it can be seen that there is little to no difference between the two models. Therefore, a two-dimensional CHT model was used to optimise the computational resources during the numerical analysis.

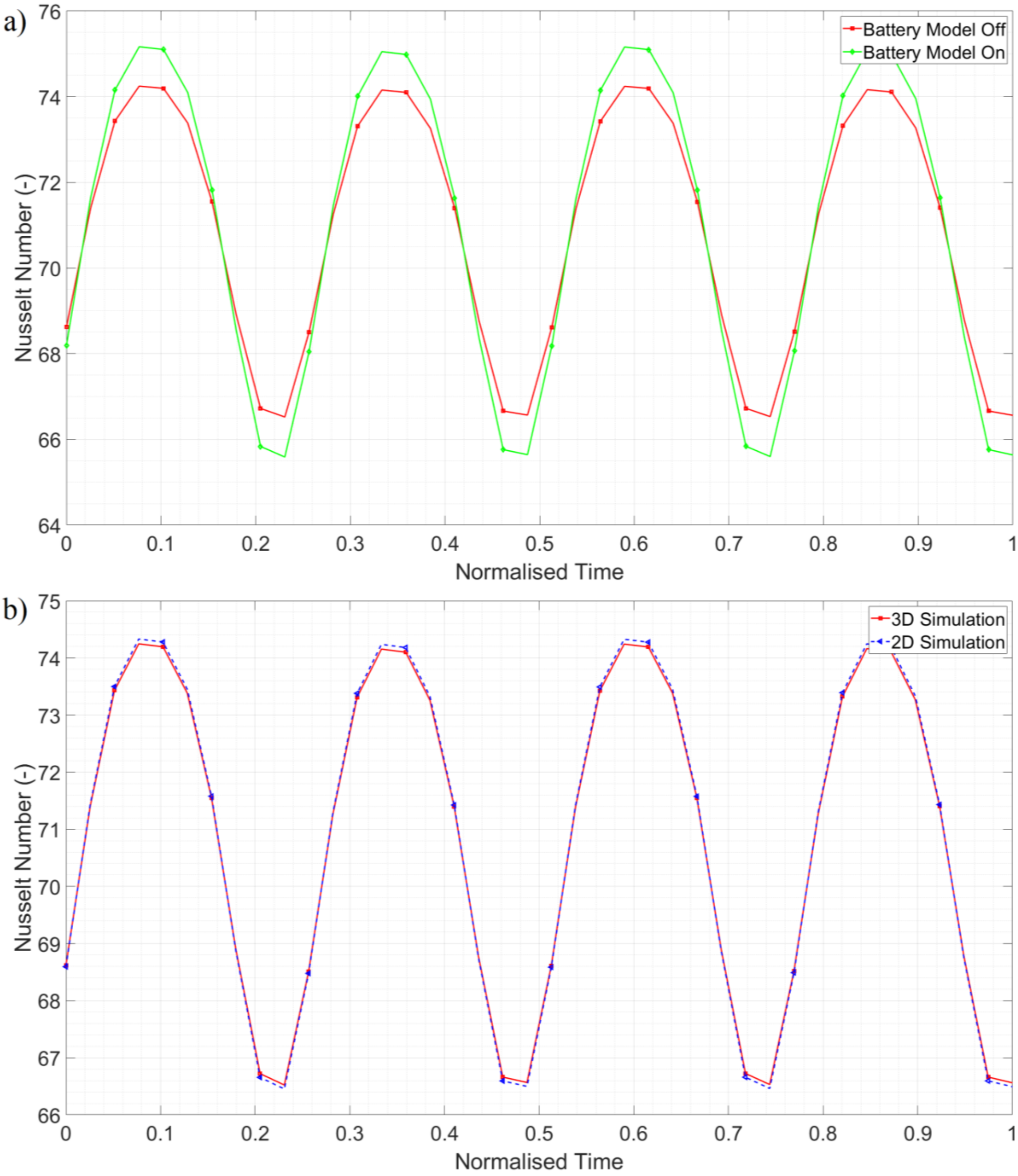

Figure 6-6 – Computational optimisation. a) MSMD battery model on vs internal heat generation, b) 3D vs 2D simulation. Fluid Type: Water, $a = 30mm/s$, $f = 10Hz$.

6.7 *Results and discussion*

This section discusses the dynamic thermal response of a battery cell to sinusoidal vibrations (see section 6.1). Here, we consider the cooling of a vibration battery cell as a single-input, single-output (SISO) dynamic model, where the input is the vibration (represented by its' frequency and amplitude) and the average Nusselt number around the battery cell is the output. The Nusselt number is computationally calculated, and the linearity of the thermal dynamic model is then evaluated. This determines if the system dynamics can be predicted using the classical frequency response approach as a cost-effective method. In general, Fourier Transforms can decompose any capricious temporal disturbances into a sequence of sinusoidal components. Given a linear system, the dynamic output of the system can be easily determined by adding the sinusoids together [128]. Therefore, understanding the system response to temporal disturbances is vital to predicting the system response to any fluctuation imposed on the battery cell due to mechanical vibration.

The spatiotemporal response of the flow temperature to a sinusoid vibration on the battery model is shown in Figure 6-7. This figure corresponds to an air flow with a Re of 6,300, with a forcing vibration frequency of 10 Hz and amplitude of 50 mm/s. Figure 6-7 depicts a typical flow-over-cylinder scenario as high-velocity air flows over the battery cell, generating a Karman Street vortex behind it. Due to the chosen model parameters shown in Figure 6-2b, vortex shedding occurs without introducing vibration into the model. However, the vortex shedding becomes stronger once vibration is activated. The positional changes of the battery cell are not visually observable in Figure 6-7 due to the minuscule vibrational amplitudes. Therefore, for further clarification, Figure 6-8 shows the temporal evolution of the flow streamlines.

In Figure 6-8, the black cross represents the centre of the battery cell, whereas the red cross is a fixed point in the domain with (x, y) coordinates of (0, 0). Figure 6-8 shows an apparent positional change of the battery cell due to vibration. The battery cell travels a maximum distance of 2.7 mm in this figure, as expected from the literature [70]. Further, changes in the flow field can be clearly observed with the evolution of the sinusoid. At 0^o, large recirculation zones in the wake of the battery cell can be clearly seen. As the sinusoid progresses to 90^o, the battery cell travels upwards. During this movement, the cell's surface presses the fluid at the top of the battery cell. As a result, the fluid at the bottom of the cell replenishes the vacant space caused by the movement. At 180^o, a mirror image of the 0^o streamline snapshot can be observed due to the batter cell's downward action before reaching the sinusoid's trough. From 90^o to 180^o, the pressing of the fluid by the battery cell is relaxed, and the oncoming flow replenishes the vacant space left behind by the downward movement of the battery cell. As the sinusoid progresses to 270^{o} from 180^{o}, the recirculation zone behind the battery cell is shed. The vortex shedding continuously occurs, forming a wave-like motion in the wake, as evident from Figure 6-7. The state of the wake is dominated by the behaviour of the battery cell due to vibration and vortex shedding.

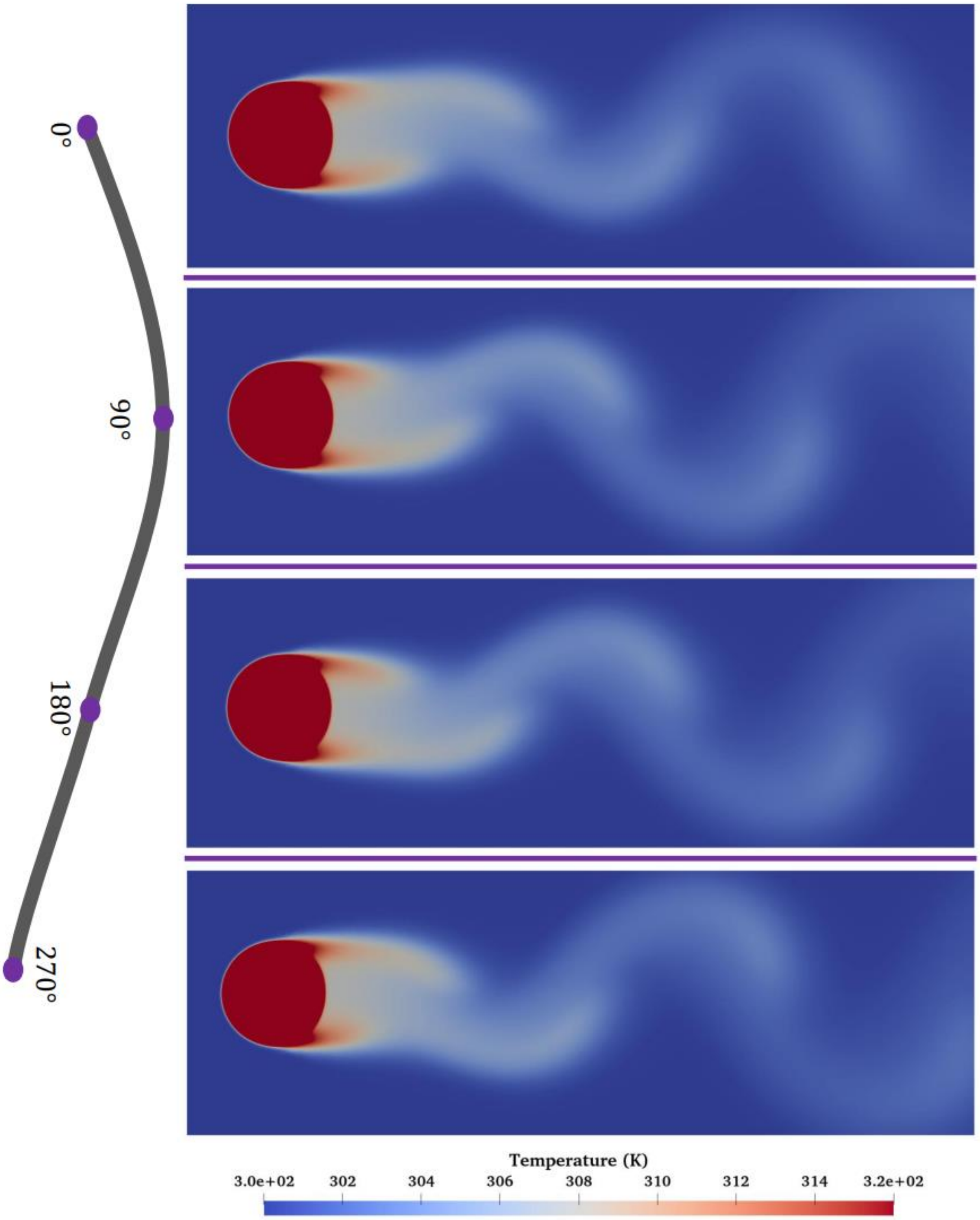

Figure 6-7 – Temperature field spatiotemporal due to a temporal sinusoidal vibration on the battery cell. Fluid Type: Air, $a = 50mm/s$, $f = 10Hz$.

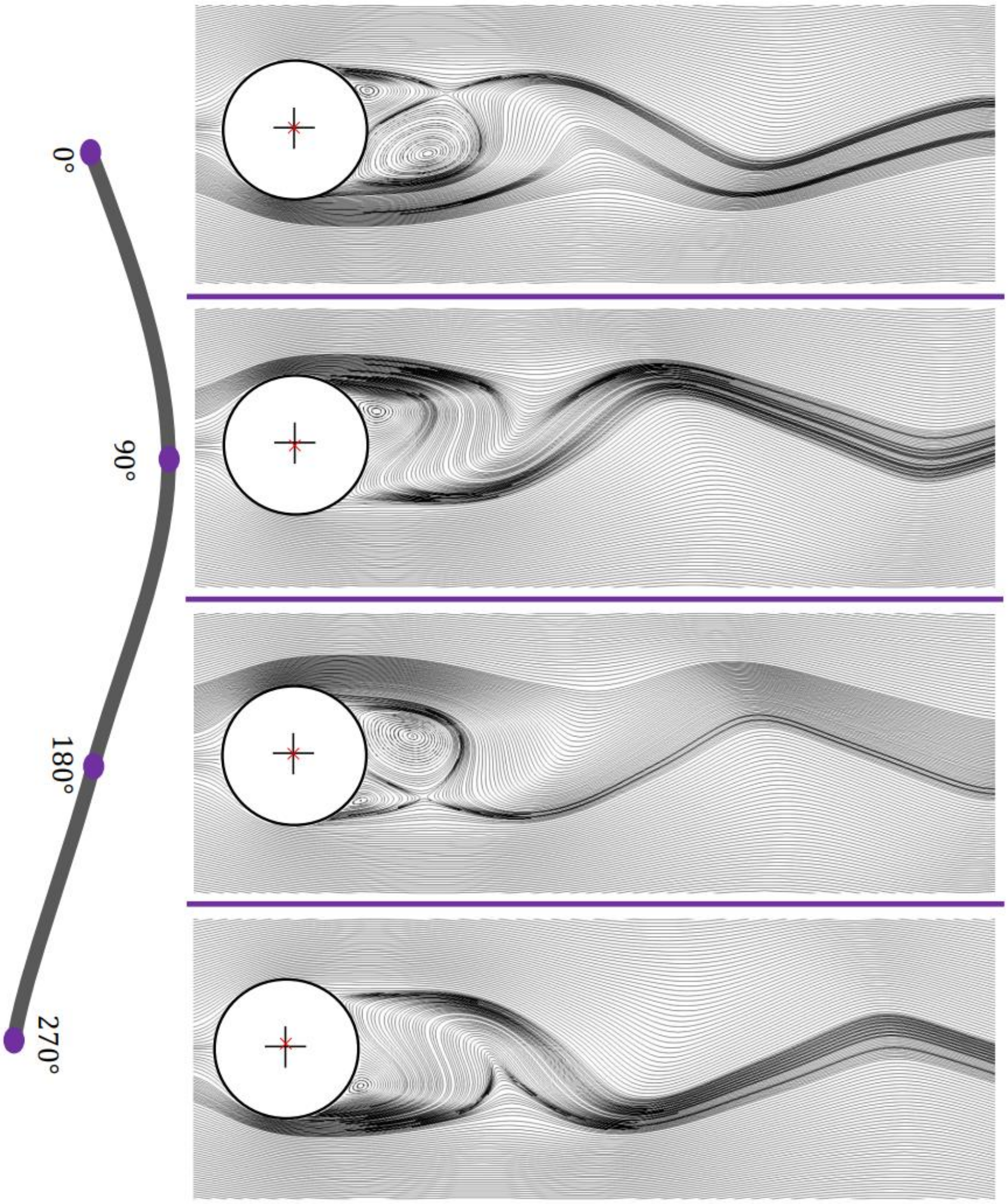

Figure 6-8 – Streamline spatiotemporal exposed to a temporal sinusoidal vibration on the battery cell. Fluid Type: Air, $a = 50mm/s$, $f = 10Hz$. Where $+$ is the centre of the circle and $\times$ is fixed point with coordinates (0,0).

6.7.1 *Air*

The temporal response of the Nusselt number and the spectral response with a modulation frequency of 10 Hz and the coolant fluid being air is shown in Figure 6-9. The battery cell thermal response shown in Figure 6-9a indicates that the Nusselt number represents a sine wave with many other additional frequencies; however, the overall shape of the response is that of a typical sine wave. As the modulation amplitude is increased, the amplitude of Nu also increases, which is an expected response since crossflow disturbances destabilise the flow around the battery cell, increasing the radial mixing of the fluid [176]. Increasing the vibrational amplitude aids in expelling heat from the surface of the battery cell, improving the overall heat transfer. This behaviour is also confirmed by Figure 6-4, where increasing the modulation amplitude led to higher values of the average Nusselt number. A classical indicator of a linear system is an equal response from the FFT and the excitation frequency [129]. In Figure 6-9b, the most decisive response in the spectra is given at one hertz, whereas the forcing frequency is ten hertz. Additionally, two frequency responses, one at six and another at twelve hertz, are circled in Figure 6-9b. These two frequencies were present in the model before vibrations were introduced. They are caused by vortex shedding, which disturbs the flow as it travels over the battery cell, causing the Nusselt number output to appear sinusoidal. This phenomenon has been visualised and described in previous studies [174, 175, 177].

Figure 6-10 shows the Nusselt number temporal response and FFT with air as the coolant fluid and a forcing frequency of 20 Hz. It can be observed that the response shown in Figure 6-10a far better represents a sine wave compared to the response shown in Figure 6-9a. Nevertheless, the Nu response shown in Figure 6-10a only illustrates two complete waves, clearly indicating a nonlinear response. The spectra response further confirms this observation, as Figure 6-10b shows. Most importantly, unlike the response shown in Figure 6-9b, the twelve-hertz pre-existing frequency gives the most decisive response. Furthermore, the spectral response also reveals an increase in the battery cell’s surface-average Nu response as the vibrational amplitude is increased from 30 mm/s to 50 mm/s. The temporal and spectral response of Nu at a modulation frequency of 30 Hz with air as the coolant fluid is shown in Figures 6-11a and 6-11b, respectively. Much like the response shown in Figure 6-10, the spectral response of Figure 6-11 also clearly indicates nonlinearity. Thus, increasing the forcing frequency from 20 to 30 Hz led to little change in the heat transfer behaviour. Changing the modulation frequency from 10 to 20 Hz drastically changed the Nu response and the spectra.

Nevertheless, systematically increasing the modulation frequency from 10 to 30 Hz with air as the coolant, the thermal response of the battery cell always appears strongly nonlinear, as shown in Figures 6-9, 6-10, and 6-11. The spectra of these modulation frequencies indicate that the excitation frequency never dominates the frequency response, and all harmonics occur below the excitation frequency. Additionally, the spectral response at the modulation frequencies of 20 and 30 Hz clearly shows that the frequencies present before introducing vibration dominate the system heat transfer dynamics. Later, another method of assessing the system linearity will be put forward.

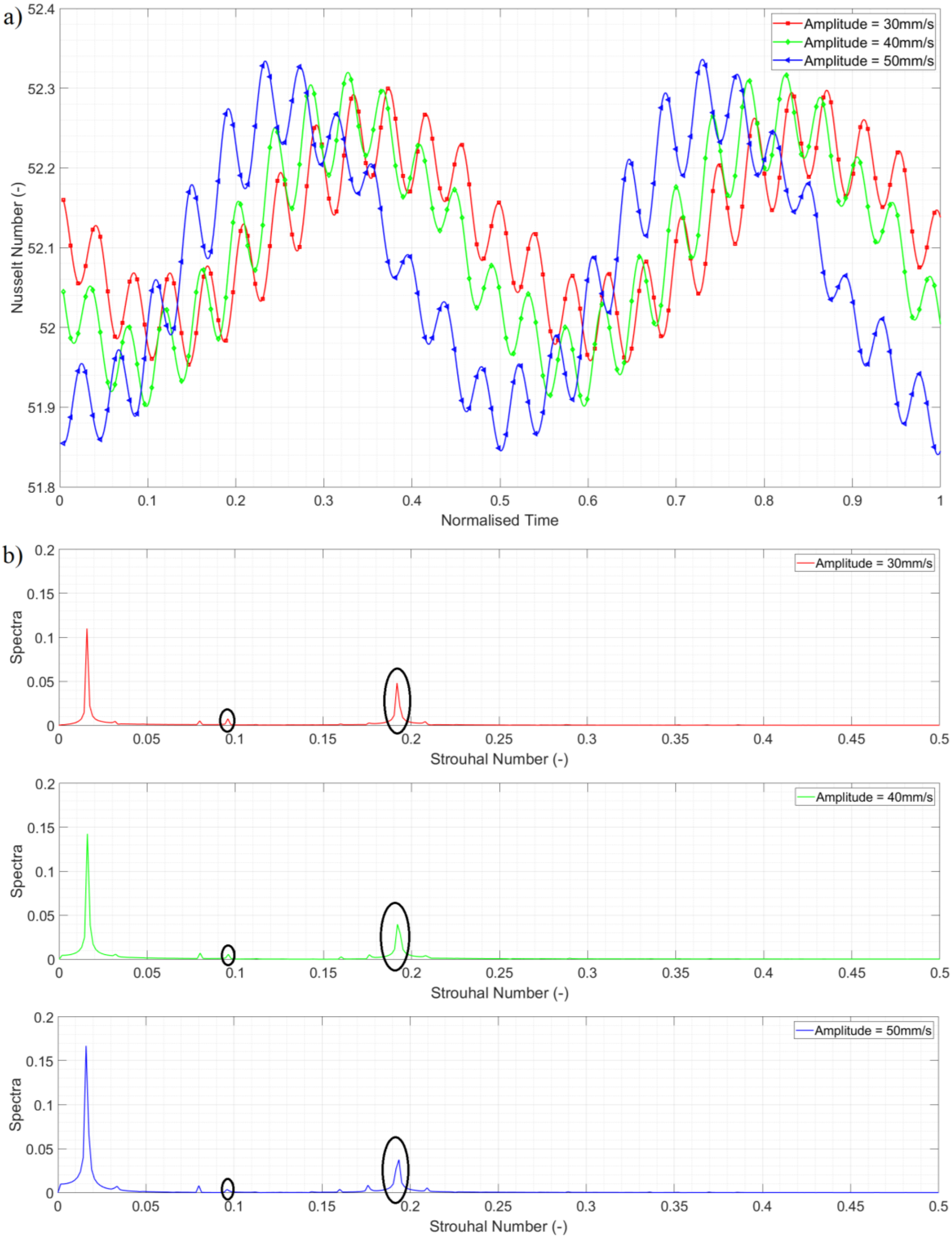

Figure 6-9 – a) Temporal evolution of Nusselt, b) Spectral response of Nusselt number. Fluid Type: Air, $f = 10Hz$ $(St = 0.16)$.

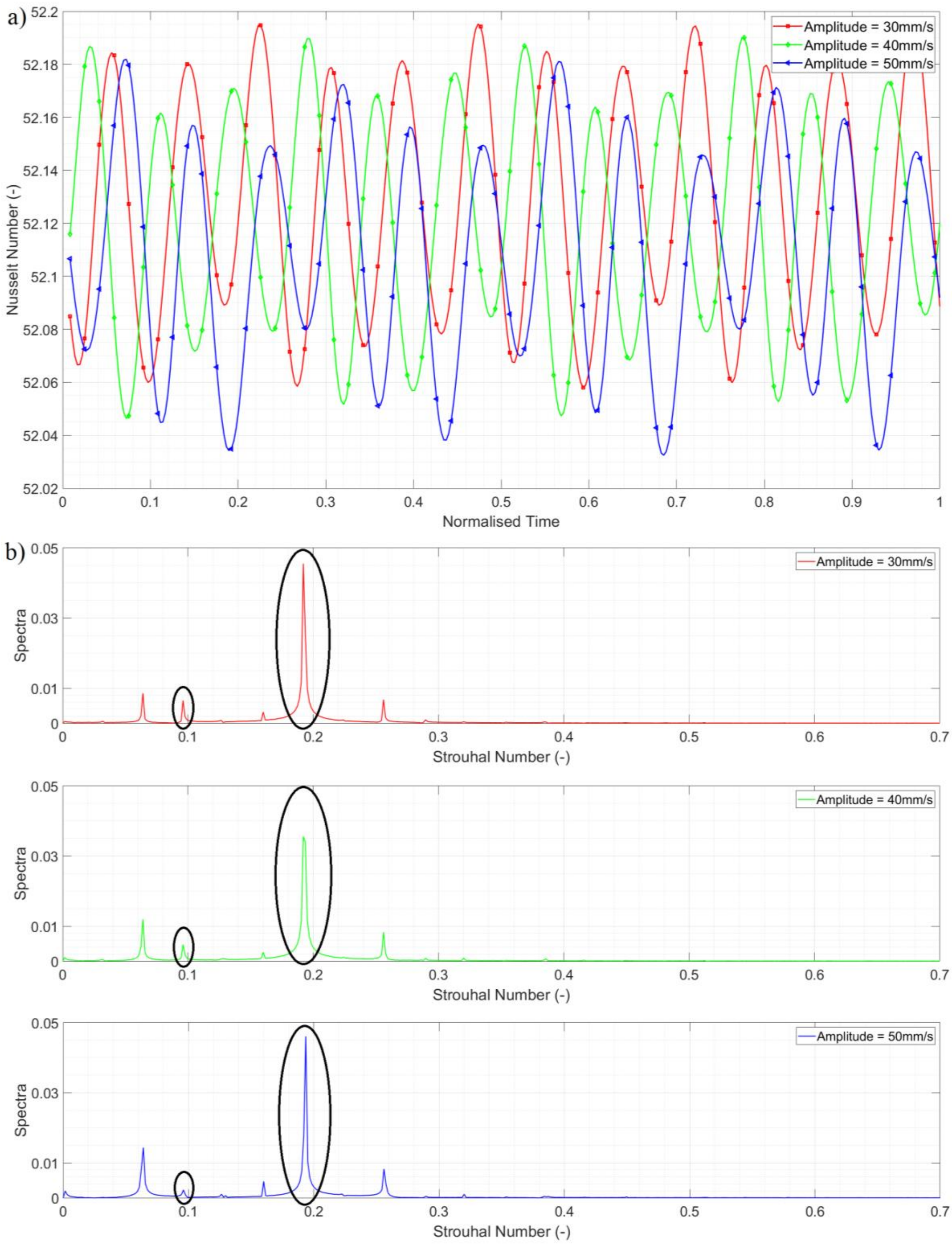

Figure 6-10 – a) Temporal evolution of Nusselt number, b) Spectral response of Nusselt number. Fluid Type: Air, $f = 20Hz$ $(St = 0.32)$.

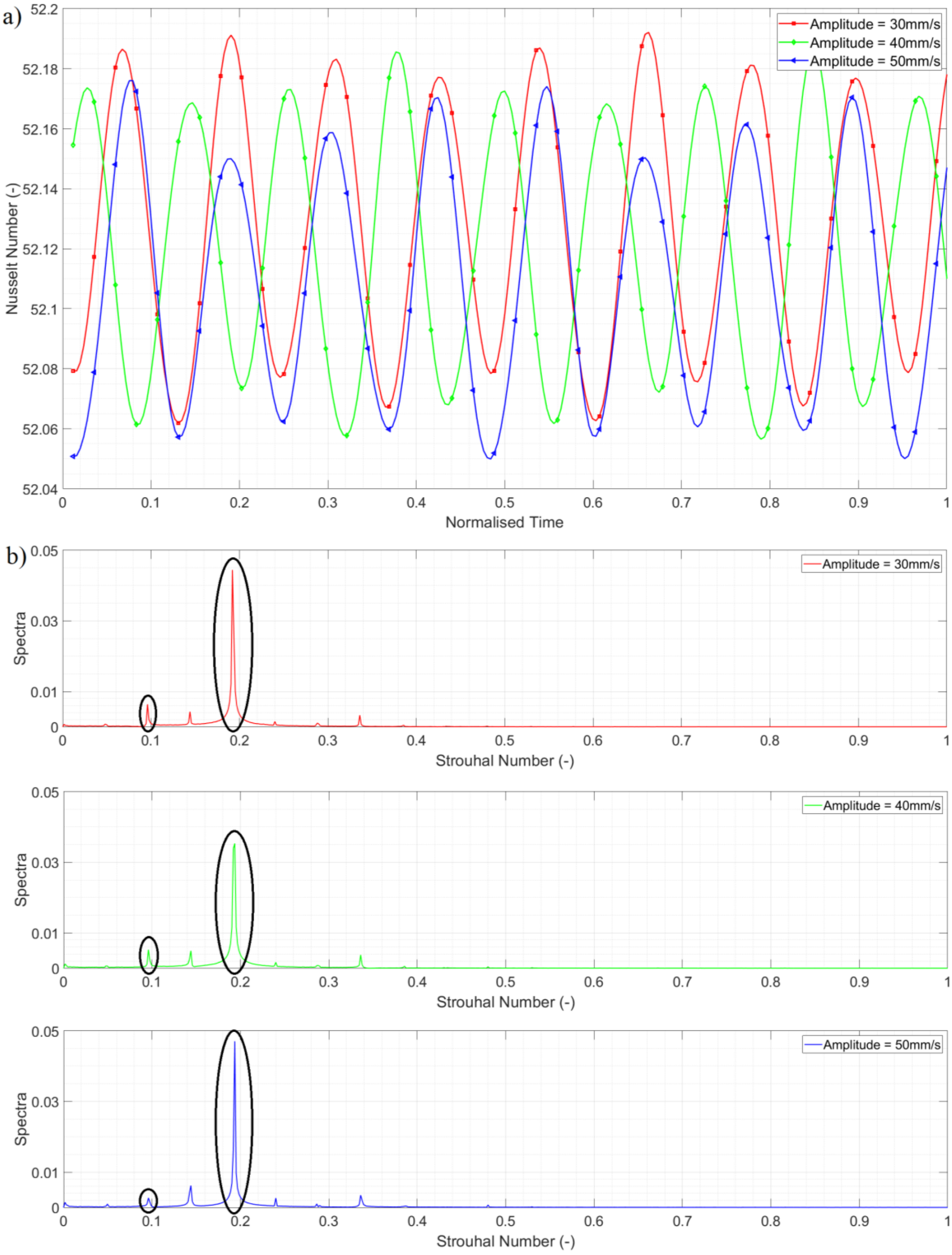

Figure 6-11 – a) Temporal evolution of Nusselt number, b) Spectral response of Nusselt number. Fluid Type: Air, $f = 30Hz$ $(St = 0.48)$.

6.7.2 *Water*

The surface-averaged battery cell Nusselt number and the corresponding FFT response at the forcing frequencies of 10, 20, and 30 Hz, where the cooling fluid is water, are shown in Figures 6-12, 6-13, and 6-14, respectively. In Figure 6-12a, the Nusselt number response of the 30 mm/s amplitude is representative of a typical sine wave. However, as the amplitude is increased, the Nu response shifts away from a sine wave, stipulating a multi-harmonic response. This shift is further evident from the FFT response shown in Figure 6-12b. Although the 30 mm/s amplitude shows a double harmonic response, the second peak is insignificant compared to the first; thus, the thermal response can be approximated as a linear dynamic system. However, the same cannot be said about the other two modulation amplitudes. From Figure 6-12a, although the Nu response of the 40 mm/s amplitude is representative of a typical sine wave, the spectral response depicts a double harmonic response. Further, the second peak in the 40 mm/s amplitude FFT response is not insignificant, indicating a mildly nonlinear system. Moving on to the Nu response from the 50 mm/s amplitude clearly shows deviation from a sine wave, depicting a strong nonlinear response. This is evident from the spectral response of the 50 mm/s modulation amplitude in Figure 6-12b, showcasing a triple harmonic output. Further, the substantial spectral amplitudes shown in Figure 6-12b compared to the air results are due to the significant differences in the thermophysical properties of the two fluids. The heat capacity of water is significantly larger than that of air; therefore, water can retain far larger quantities of heat before experiencing an increase in temperature, allowing for a larger Nusselt number output, as observable from Figure 6-12a.

The response of the 30 mm/s modulation amplitude in Figure 6-13b, where the modulation frequency is 20 Hz, continues to offer a linear response. However, the mildly nonlinear response of the 40 mm/s amplitude in Figure 6-12b is no longer a valid observation for Figure 6-13b due to the growth of the second and the appearance of a third harmonic. Therefore, the 40 mm/s amplitude response in Figure 6-13b is nonlinear. Further, the Nu response of the 40 mm/s amplitude in Figure 6-13a can be clearly seen to deviate from a typical sine wave. Simultaneously, the nonlinear response of Nu of the 50 mm/s amplitude has become more substantial compared to the response shown in Figure 6-12. This is further evident by the spectral response, which continues to be completely nonlinear. From Figure 6-13b, the FFT response of the 50 mm/s amplitude shows that the first and second harmonics are almost equal, the third harmonic is moderately stronger than Figure 6-12b, and a fourth harmonic is present. This behaviour is further amplified in Figure 6-14, where the forcing frequency is 30 Hz. The 30 mm/s amplitude continues to be linear. The nonlinearity has increased in the 40 mm/s amplitude response due to the growth of the second and third harmonics. However, in the 50 mm/s amplitude response, substantial growth in the second, third, and fourth harmonics amplifies the nonlinear response. Moreover, the excitation frequency of 30 Hz no longer dominates the dynamic response; instead, the strongest spectral response is given at a frequency of 60 Hz.

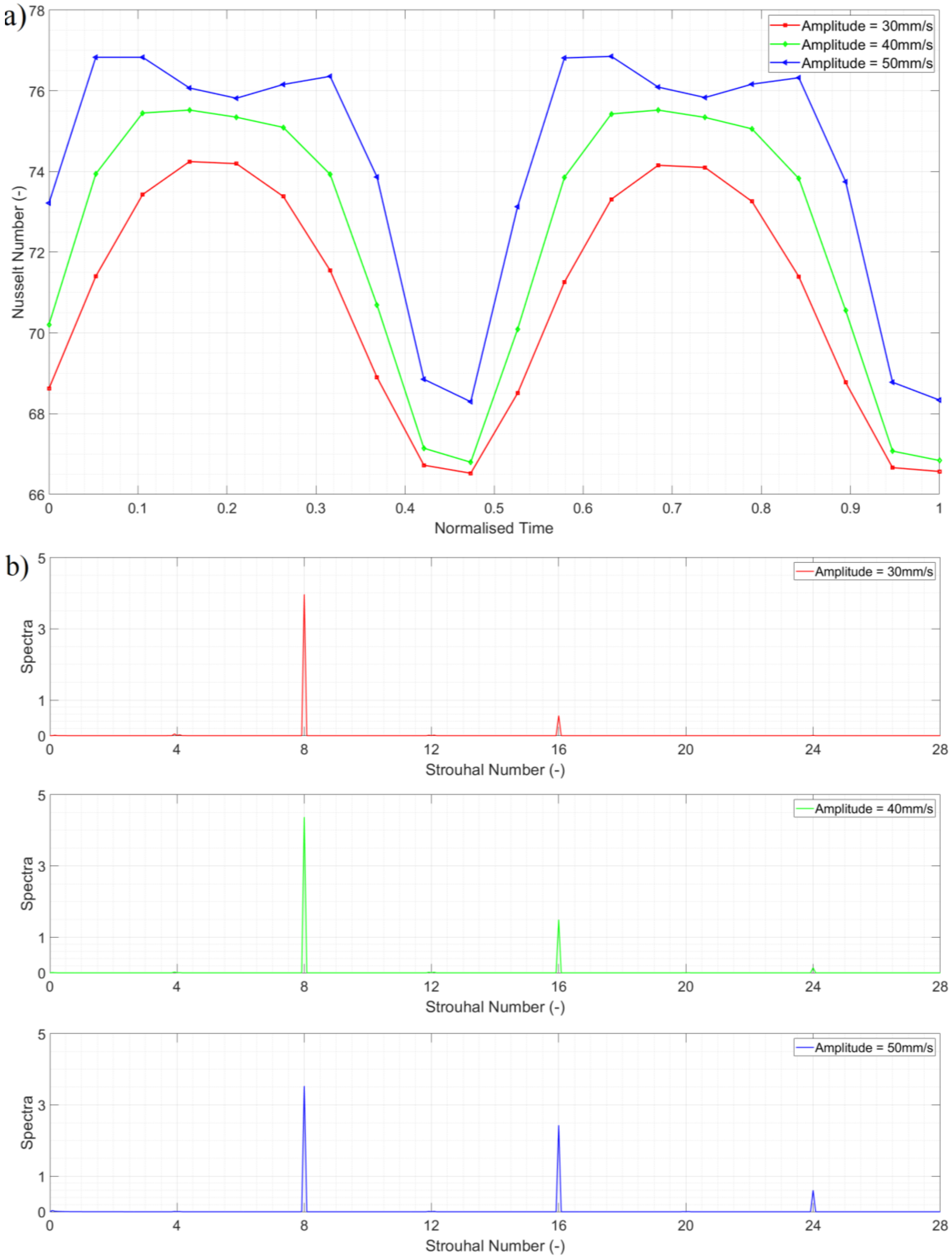

Figure 6-12 – a) Temporal evolution of Nusselt number, b) Spectral response of Nusselt number. Fluid Type: Water, $f = 10Hz$ $(St = 8)$.

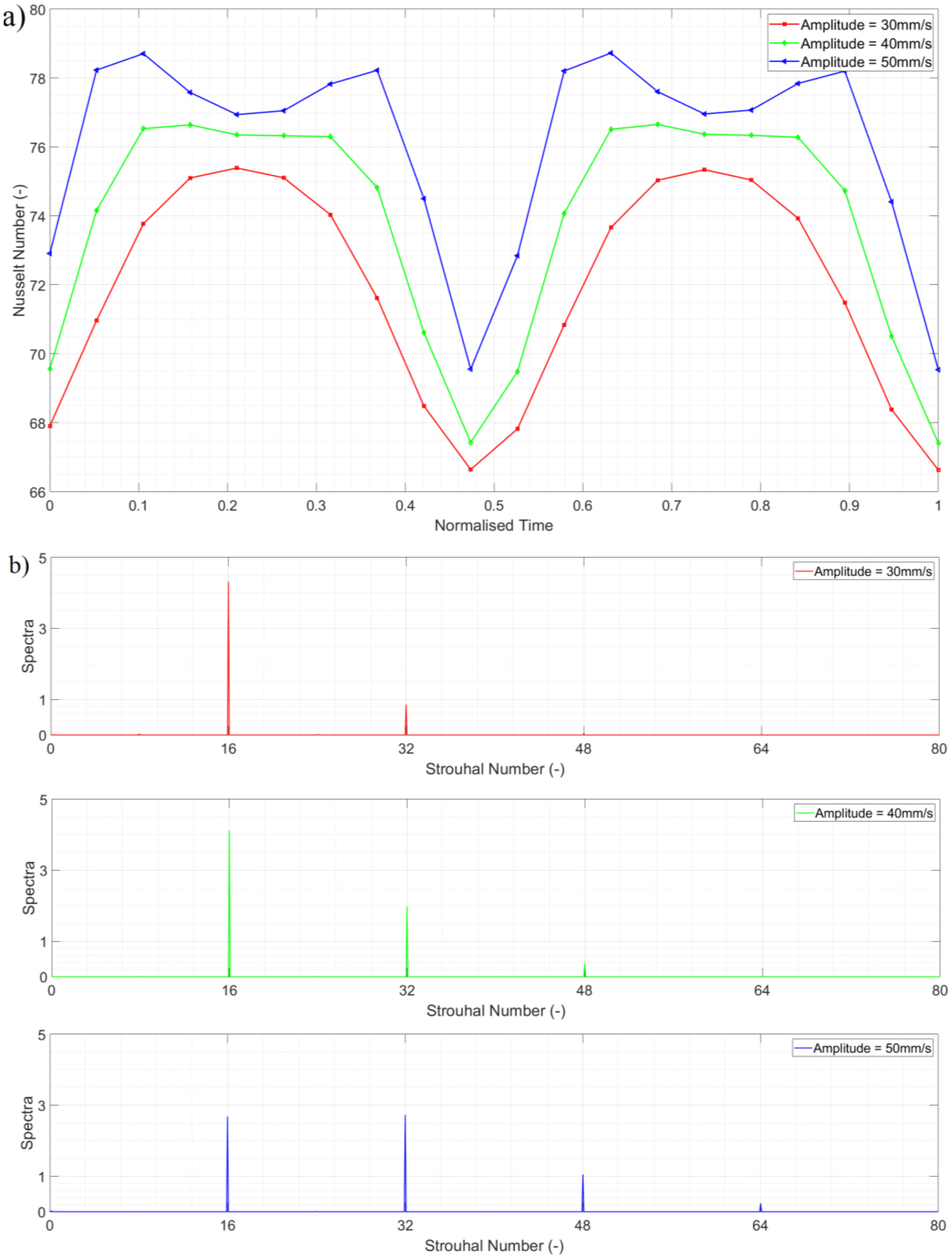

Figure 6-13 – a) Temporal evolution of Nusselt number, b) Spectral response of Nusselt number. Fluid Type: Water, $f = 20Hz$ $(St = 16)$.

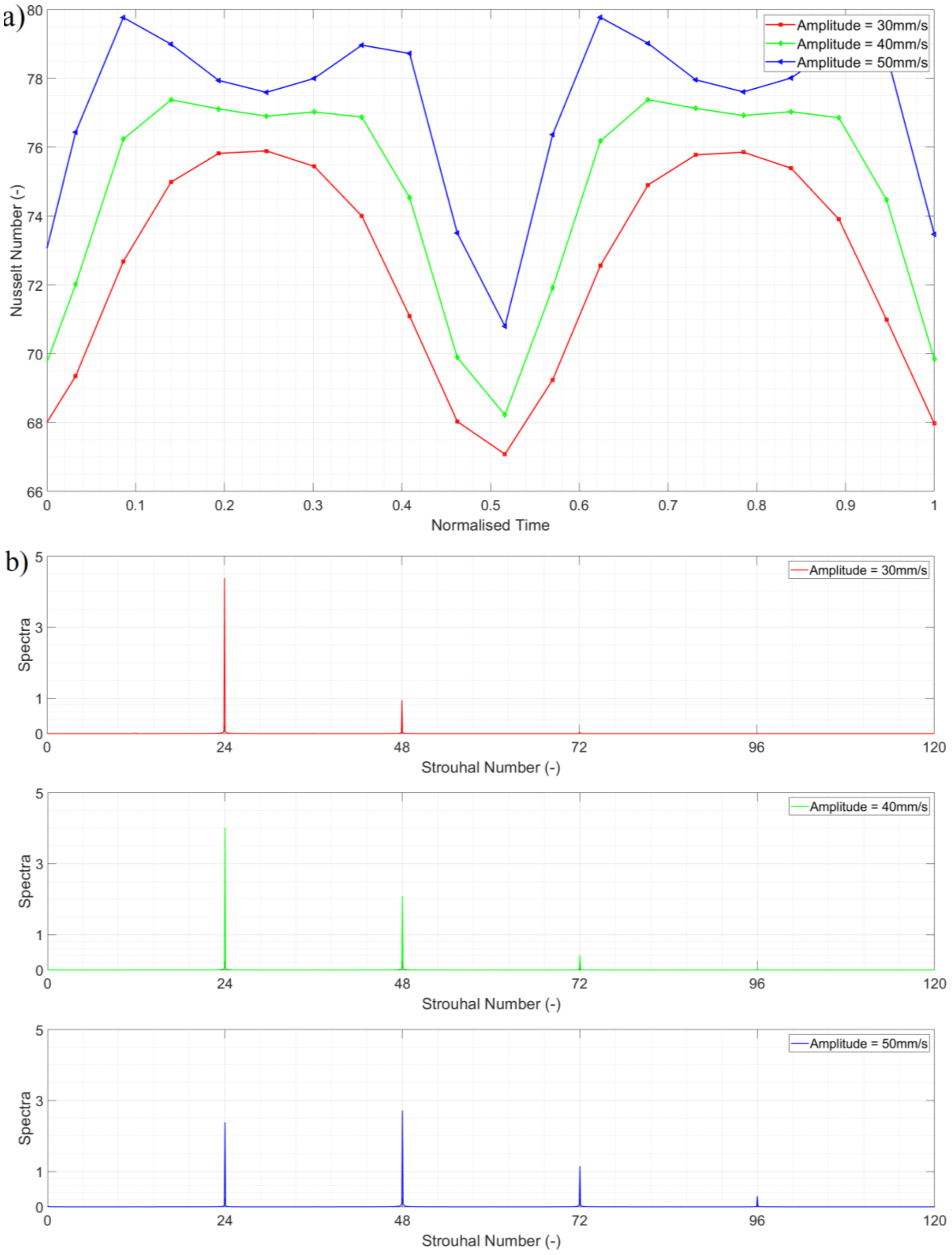

Figure 6-14 – a) Temporal evolution of Nusselt number, b) Spectral response of Nusselt number. Fluid Type: Water, $f = 30Hz$ ($St = 24$).

6.7.3 *Lissajous Patterns*

The findings presented in sections 6.7.1 and 6.7.2 are further supported by the Lissajous Patterns (phase portraits) of the normalised Nusselt number against the normalised input signal for air and water, as shown in Figures 6-15 and 6-16. Other studies have used phase portraits to determine the linearity of system dynamics [122, 133]. The dynamic system can be deemed linear if the phase portraits depict an axisymmetric response [134]. However, any deviation from symmetry would result in the system dynamics being mildly or strongly nonlinear. From Figure 6-15, none of the nine phase portraits show signs of symmetry, confirming that the spectral response of the air shown in Figures 6-9, 6-10, and 6-11 are completely nonlinear.

However, moving to the water results, some figures in Figure 6-16 show signs of symmetry. A ‘butterfly’ effect can be observed in Figures 6-16a, 6-16d, and 6-16g; however, these figures do not show perfect symmetry due to a minor second harmonic in their respective spectra. Nevertheless, the minor deviation causing the asymmetric behaviour can be safely ignored, and the system dynamics can be approximated as linear. Further, Figures 6-16b, 6-16e, and 6-16h correspond to the modulation amplitude of 40 mm/s at 10, 20, and 30 Hz, respectively. Figure 6-16b shows minor signs of symmetry in line with its spectral response, resulting in a mildly nonlinear case. However, Figures 6-16e and 6-16h show slightly larger signs of asymmetry, indicating a nonlinear response as shown by their respective spectral responses. Although Figures 6-16c, 6-16f, and 6-16i may seem axisymmetric, the numerical analysis presents no signs of symmetry, resulting in a strongly nonlinear response. Unlike linear cases, the dynamics of nonlinear systems cannot be straightforwardly or quickly predicted using simple control engineering methods – i.e. transfer functions [176]. In most cases, high-order modelling is necessary to predict these dynamics, which are computationally very demanding. Therefore, identifying conditions of nonlinear system dynamics is crucial for effective BTMSs.

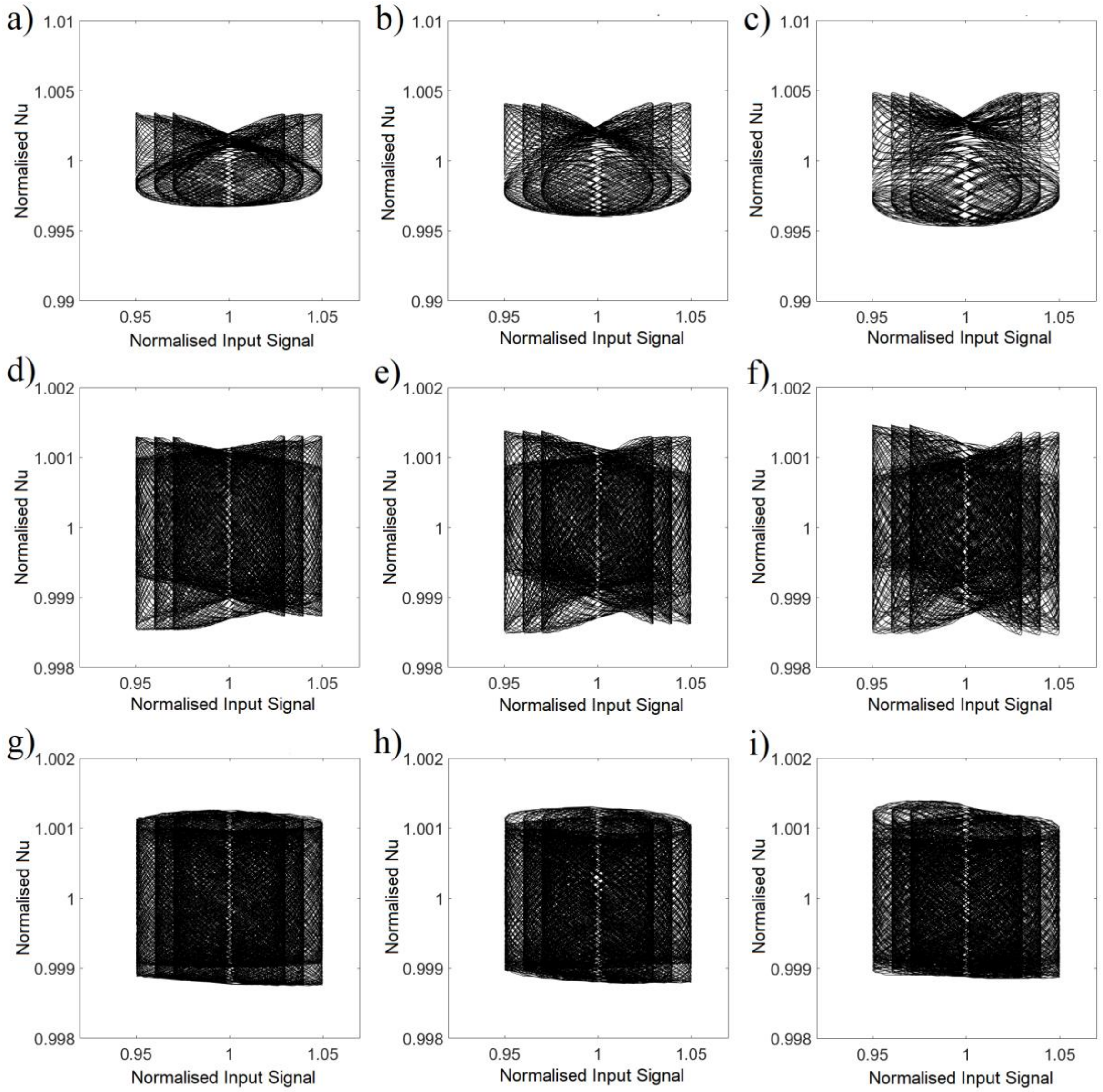

Figure 6-15 – Lissajour Patterns (Phase portraits). Fluid type: Air. $f = 10Hz$ a) $a = 30mm/s$, b) $a = 40mm/s$, c) $a = 50mm/s$; $f = 20Hz$ d) $a = 30mm/s$, e) $a = 40mm/s$, f) $a = 50mm/s$; $f = 30Hz$ g) $a = 30mm/s$, h) $a = 40mm/s$, i) $a = 50mm/s$.

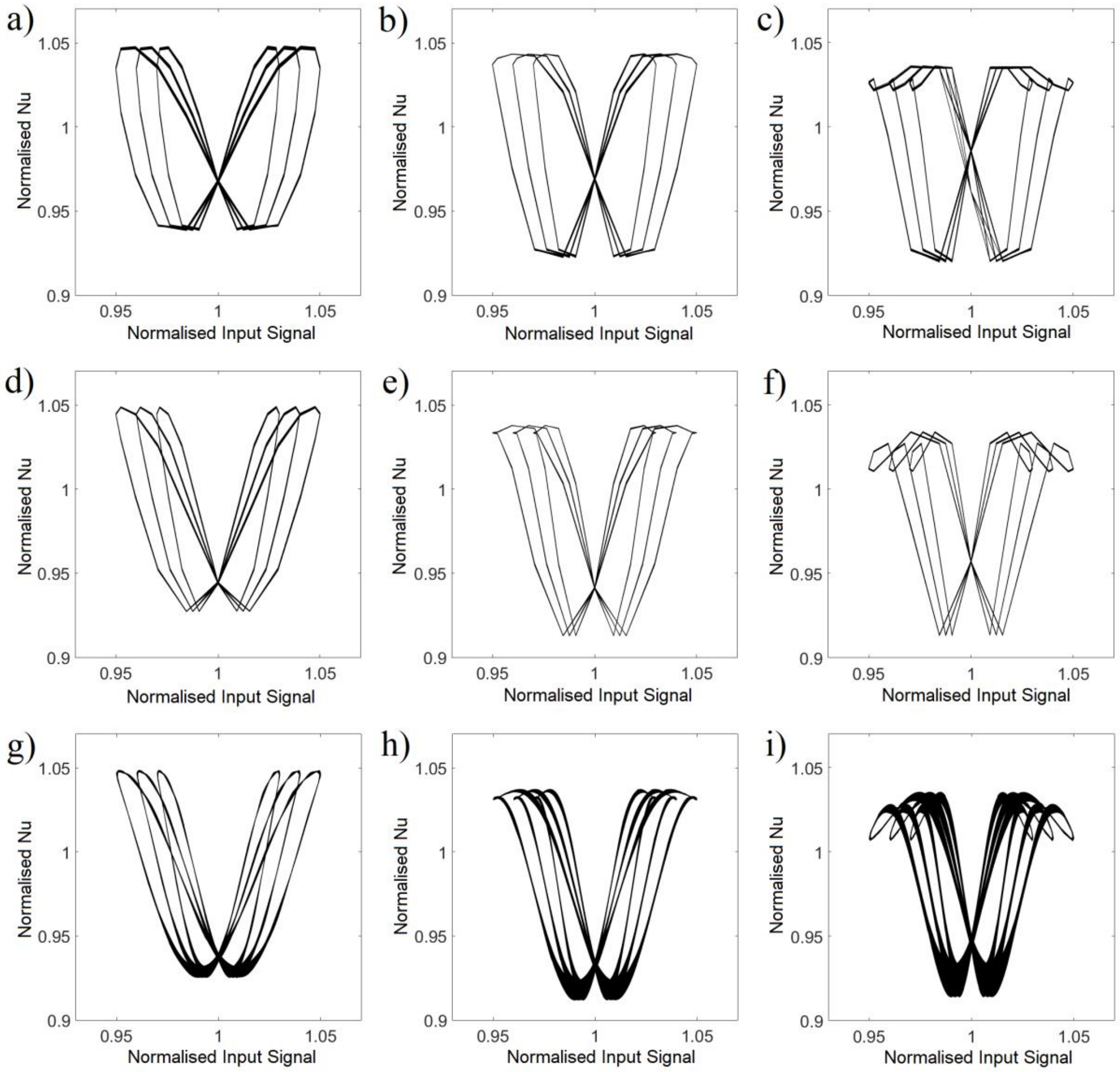

Figure 6-16 – Lissajour Patterns (Phase portraits). Fluid type: Water. $f = 10Hz$ a) $a = 30mm/s$, b) $a = 40mm/s$, c) $a = 50mm/s$; $f = 20Hz$ d) $a = 30mm/s$, e) $a = 40mm/s$, f) $a = 50mm/s$; $f = 30Hz$ g) $a = 30mm/s$, h) $a = 40mm/s$, i) $a = 50mm/s$.

6.7.4 *Forcing frequency approach*

The classical frequency response approach can be used to predict the system dynamics of linear or mildly nonlinear cases – given information on the amplitude and phase of the dynamic response [128]. The concept of frequency response is often used for SISO systems. In the present chapter, the vibrational disturbance is used as the single input, and the oscillating Nusselt number response is the single output. Therefore, the amplitude at the forcing frequency and the non-dimensional delay (phase response) are calculated and shown in Figures 6-17a and 6-17b, respectively. It should be noted that since the air cases always have a strong nonlinear response with many harmonics, only the frequency response of the water cases is presented. Figure 6-17a shows that as the modulation frequency increases, the amplitude at the forcing frequency decreases. This stipulates that the system is more responsive to lower modulation frequencies, which aligns with previous studies' findings [122, 131], where the fluid flow was excited and featured a stronger response at lower frequencies. Conventionally, lower excitation frequencies give the system sufficient time to respond to any disturbance, leading to a more substantial amplitude output. Moreover, the large amplitude can also be attributed to water's significantly large thermal conductivity and capacity, as evident from Figures 6-12, 6-13, and 6-14. Thus, for a given disturbance, water-cooled systems must experience significant variations in the convection coefficient, resulting in larger amplitudes in the frequency response.

Additionally, from Figure 6-17b, the non-dimensional delay decreases as the modulation frequency increases. This also follows the pattern presented by previous studies [122, 131]. The diminishing delay with increasing frequency is due to the available time between the vibration occurring and the ability of the fluid to draw heat away from the battery cell becoming significantly shorter – shorter wavelength frequencies do not allow the fluid-thermal reaction to complete as the frequency is increased.

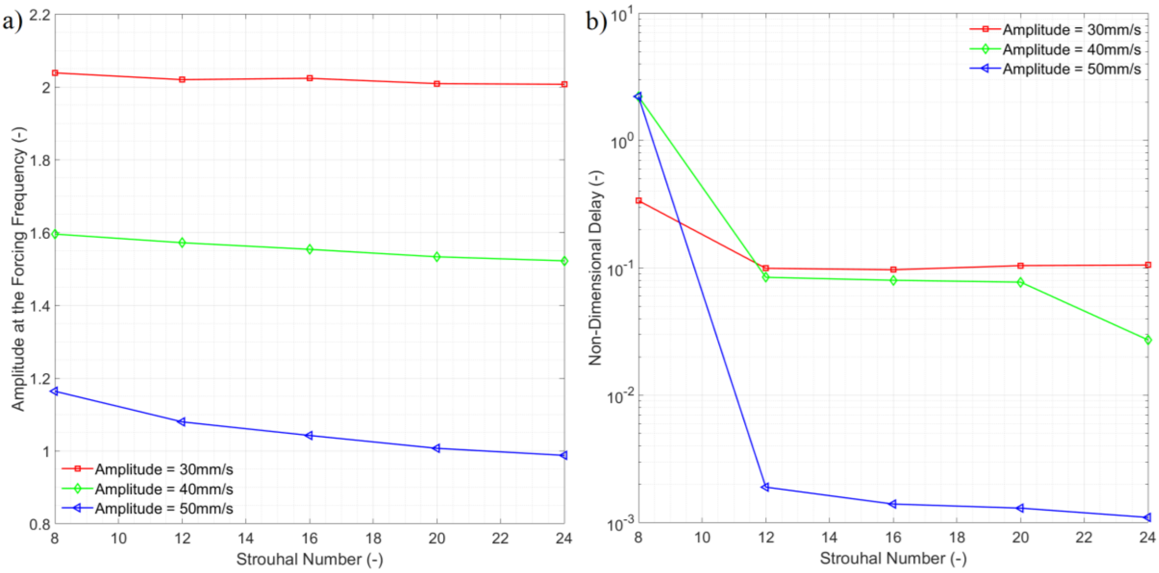

Figure 6-17 – Forcing frequency comparison, a) Amplitude response at the forcing frequency, and b) Phase response. Fluid Type: Water.

6.8 *Conclusions*

EV battery modules/packs are exposed to mechanical vibrations due to numerous environmental and driving factors, which renders their thermal response inherently unsteady. Therefore, effective BTMSs require the ability to predict a battery cell's temperature, which is conventional for linear systems through the classical frequency response approach (e.g. transfer functions). However, such methods become obsolete for systems featuring nonlinear dynamics. Thus, determining the condition under which the battery cooling dynamics feature linear or nonlinear responses to vibrational modulation is essential. In this chapter, the single-cell system response to vibrational loads was numerically examined by evaluating the surface-averaged Nusselt number of a battery cell. The results of the two fluids, air and water, were analysed in the time and frequency domains and evaluated using phase portraits. The vibrational input and the heat transfer output were considered as a SISO system to determine the applicability of the classical frequency response method. The key findings are summarised below.

- The thermal system response is always nonlinear for all air cases, with the dominating frequency never being the excitation frequency.
- The thermal system response can be approximated as linear for cases with water at low modulation amplitudes. The phase portraits display a 'butterfly' pattern for such cases.
- As the excitation frequency is increased for the water cases, the second and third harmonic response is slightly amplified, increasing their nonlinearity. This can be clearly observed by comparing the 30 mm/s response at 10 and 20 Hz.
- High-frequency temporal modulations generate a strong nonlinear response. This can be explained by the significant disturbance of the oncoming flow due to the high modulation speed. This causes increased radial mixing, impacting the battery cell heat transfer.
- The classical frequency response method (transfer functions) can be utilised to predict heat transfer dynamics. However, this method only applies to water cases as they feature a linear response at low-amplitudes (i.e. $a < 50\ mm/s$).

It remains a future task to develop low-order models for predicting the thermal behaviour of nonlinear system dynamics and to integrate the findings of this chapter into a BTMS.

Chapter 7. Conclusions and future work

The current work has studied the heat transfer dynamics of battery cells/modules that can influence the effectiveness of a BTMS which are crucial for maintaining the battery cells within their optimal temperature range. This is important because their operational temperature directly impacts the battery cell's performance. Vehicle manoeuvres and driving patterns differ from user to user, directly impacting the thermal characteristics of the battery cells. Therefore, effective thermal control of batteries is essential for EVs to gain further popularity and outgrow the traditional ICE vehicle market.

One method is to use predictive tools such as transfer functions as a cheap and effective method of modelling the battery's thermal behaviour. However, such predictions are effortless for linear systems and become laborious and complicated for any real system exhibiting a measure of nonlinearity larger than 10%. Therefore, it is essential to determine conditions in which the battery cells will feature linear or nonlinear thermal dynamics due to unsteady temporal disturbances.

RANS-based numerical simulations coupled with the energy equation were carried out for battery cell/module under unsteady loads. The realisable $k - \epsilon$ model was employed for enhanced model accuracy. When the inlet fluid was set to air, the ideal gas model was used. The model was switched to constant density for water and nanofluids. All models and equations utilised within the numerical simulations were discretised using the second-order upwind scheme, and the PIMPLE algorithm was used to solve for the velocity-pressure coupling. Due to the significance of the fluid flow, the impact of natural and forced convection was compared, and all gravitational effects were ignored. The current work was thoroughly validated against numerous empirical correlations and numerical and experimental data. The close agreement between the simulated results and the data mentioned earlier confirmed the analysis presented in this thesis.

7.1 *Summary of conclusions*

Considering the temporal modulation imposed on the battery cell's surface heat flux, the resultant Nusselt number response was analysed in the time and frequency domains. The results showed that the convective heat transfer dynamic response remains linear at low modulation amplitudes ($a = 10\%$) for all coolant fluids. Disturbances featuring low amplitude of modulation and short duration lead to linear conditions, which could be predicted using transfer function. As the modulation amplitude was increased ($a = 30\%$ or

$a = 60\%$), the surface-averaged Nusselt number became mildly nonlinear or strongly nonlinear dependant on the coolant fluid. Low frequencies, such as $f = 0.25\ Hz$, tend to generate a strong nonlinear response due to the prolonged time available for the fluid dynamic and heat transport interactions to occur. However, as the excitation frequency was increased, the measure of nonlinearity decreased.

Furthermore, the system response of a battery module under high strain due to extreme thermal loads being imposed on the battery cells was also investigated. The average surface battery cell temperature was quantitively examined. The analysis revealed that when using air as the coolant fluid, all the ramp cases produce an overshoot in the temperature temporals. Additionally, the air cases also produce high values of the settling time than the water cases. The ramp duration directly impacts the response of each case – this is to say that regardless of the coolant fluid, a ramp duration of 5 seconds (NYCC1) will always produce the highest value of settling time. As expected, water is far better at achieving cooler battery cell temperatures, while also minimising the cell-to-cell temperature difference. When comparing the heating or cooling time of the two coolant fluids, water produces a more horizontal trend line, whereas air produces a vertical trend line. This difference in the trend lines is due to the difference in the two fluids thermophysical properties. The significantly larger heat capacity of water allows it to retain higher quantities of heat before experiencing an increase in its temperature. Comparing the SC03 single-cycle segment, water reacts almost 34% faster to the temporal changes in the internal heat generation than air.

Finally, EV battery packs are exposed to mechanical vibrations during operation, making their thermal response unsteady. Although the vibrations are random, they are primarily influenced by the vehicle's suspension system and settings and reside in the 10 to 30 Hz range. The spectra response revealed that air cases always display strong nonlinearity, and the dominating response is never at the forcing frequency. The system dynamics of water at low modulation amplitudes can be approximated as linear. However, as the excitation frequency is increased, the nonlinear response is amplified, and the system deviates from linearity. Further, high-frequency (30 Hz) temporal disturbances generate the strongest nonlinear response. The classical approach of frequency response – such as transfer functions – can be used to predict the system heat transfer dynamics; however, such predictions are only limited to the water cases at low amplitudes as they feature a linear response ($a < 50\ mm/s$).

7.2 *Recommendations of future work*

This work investigated the thermal response of battery cells/modules to various unsteady disturbances. Since the process of heat generation and transfer of Li-ion battery cells is complex, there are numerous ways to enhance the effectiveness of battery thermal management systems and further push the use of EVs to combat the global climate impact. Further, BTMS is still immature, with the biggest research boom being conducted in the last decade. Therefore, some suggestions for future work are put forward.

1. The nanofluids modelling was simplified and treated as a single-phase liquid to save on computational resources. Modelling nanofluids using a liquid and solid phase is far more representative of their true nature. Further, the impact of having metallic particles near batteries may cause magnetic coupling. This would result in a far more comprehensive nanofluid investigation. Further, the influence of the direct flow of nanoparticles over a battery module can also be analysed.

2. The flow rate of the coolant fluid could be linked directly to the temperature of the battery cells making the BTMS an active control system. The control system would monitor each battery cell and the cell-to-cell temperature difference and take measures to prevent over or under-cooling of the battery cells. The response time of the coolant system to temporal changes could benefit from an active control system.

3. The vibrational study was only conducted on a single battery cell. This could be further expanded to include numerous cells under synchronous or asynchronous motion. Previous works have studied the fluid dynamics of asynchronous motion of tandem cylinders [178, 179]. The methodology of these studies can be replicated to find the thermal impact on tandem battery cells. Moreover, the vibration direction could be changed from longitudinal to transverse (vibration in x-direction), after which multi-degrees of freedom can be introduced so that the battery cells can vibrate diagonally.

4. The problems investigated throughout this thesis could be combined into a single problem. An example would be a battery module in which the cells are under vibration and unsteady thermal loads due to extreme power draw. The resultant Nusselt number would be analysed in the time and frequency domain. The analysis would then be compared against the results shown in Chapters 4 and 6.

5. Finally, the results of all studies conducted throughout this thesis could be combined and integrated into a BTMS. The results could also be used to develop low-order models that predict the nonlinear system dynamic response of heat transfer to unsteady inputs.

References

[1] "Global EV Outlook 2021 – Analysis - IEA," 2021. https://www.iea.org/reports/global-ev-outlook-2021 (accessed Jul. 27, 2023).

[2] "RENEWABLES 2022 GLOBAL STATUS REPORT," 2022. https://www.ren21.net/gsr-2022/ (accessed Jul. 27, 2023).

[3] "RENEWABLES 2017 GLOBAL STATUS REPORT," 2017. https://www.ren21.net/gsr-2017/ (accessed Jul. 27, 2023).

[4] "House of Commons Business, Energy and Industrial Strategy Committe. Electric vehicles: driving the transition," 2019. https://publications.parliament.uk/pa/cm201719/cmselect/cmbeis/383/383.pdf (accessed Jul. 27, 2023).

[5] S. F. Tie and C. W. Tan, "A review of energy sources and energy management system in electric vehicles," *Renew. Sustain. Energy Rev.*, vol. 20, pp. 82–102, Apr. 2013, doi: 10.1016/J.RSER.2012.11.077.

[6] H. Lee and G. Lovellette, "Will Electric Cars Transform The U.S. Vehicle Market? An Analysis of The Key Determinants," 2011, Accessed: Jul. 27, 2023. [Online]. Available: https://www.belfercenter.org/sites/default/files/legacy/files/Lee Lovellette Electric Vehicles DP 2011 web.pdf

[7] K. T. Chau and C. C. Chan, "Emerging energy-efficient technologies for hybrid electric vehicles," *Proc. IEEE*, vol. 95, no. 4, pp. 821–835, 2007, doi: 10.1109/JPROC.2006.890114.

[8] J. Speirs, M. Contestabile, Y. Houari, and R. Gross, "The future of lithium availability for electric vehicle batteries," *Renew. Sustain. Energy Rev.*, vol. 35, pp. 183–193, Jul. 2014, doi: 10.1016/J.RSER.2014.04.018.

[9] G. E. Blomgren, "The Development and Future of Lithium Ion Batteries," *J. Electrochem. Soc.*, vol. 164, no. 1, pp. A5019–A5025, Dec. 2017, doi: 10.1149/2.0251701JES/XML.

[10] H. J. Herfurth, "Building better batteries | Laser Focus World," *INDUSTRIAL LASER SOLUTIONS*, 2009. https://www.laserfocusworld.com/industrial-laser-solutions/article/14215442/building-better-batteries (accessed Jul. 27, 2023).

[11] S. Abada, G. Marlair, A. Lecocq, M. Petit, V. Sauvant-Moynot, and F. Huet, "Safety

focused modeling of lithium-ion batteries: A review," *Journal of Power Sources*, vol. 306. Elsevier B.V., pp. 178–192, Feb. 29, 2016. doi: 10.1016/j.jpowsour.2015.11.100.

[12] J. Vetter *et al.*, "Ageing mechanisms in lithium-ion batteries," *J. Power Sources*, vol. 147, no. 1–2, pp. 269–281, Sep. 2005, doi: 10.1016/j.jpowsour.2005.01.006.

[13] "Electric Cars, Buses, & Trucks Could Charge While Driving On eHighways — Will Soon In Sweden - CleanTechnica," 2019. https://cleantechnica.com/2019/05/02/electric-cars-buses-trucks-could-charge-while-driving-on-ehighways-will-soon-in-sweden/ (accessed Jul. 27, 2023).

[14] "How Long Do Electric Car Batteries Last?," 2023. https://www.autotrader.com/car-tips/how-long-do-electric-car-batteries-last (accessed Jul. 27, 2023).

[15] W. Walker, S. Yayathi, J. Shaw, and H. Ardebili, "Thermo-electrochemical evaluation of lithium-ion batteries for space applications," *J. Power Sources*, vol. 298, pp. 217–227, Dec. 2015, doi: 10.1016/J.JPOWSOUR.2015.08.054.

[16] "How Ford, GM, and Tesla are building better EV batteries - Vox," 2022. https://www.vox.com/recode/23027110/solid-state-lithium-battery-tesla-gm-ford (accessed Jul. 27, 2023).

[17] J. Lin, X. Liu, S. Li, C. Zhang, and S. Yang, "A review on recent progress, challenges and perspective of battery thermal management system," *Int. J. Heat Mass Transf.*, vol. 167, p. 120834, Mar. 2021, doi: 10.1016/j.ijheatmasstransfer.2020.120834.

[18] V. Talele, P. Thorat, Y. P. Gokhale, and H. Desai, "Technical Review on Battery Thermal Management System for Electric Vehicle Application," Singapore: Springer, 2023, pp. 177–225. doi: 10.1007/978-981-19-4502-1_9.

[19] G. Zhao, X. Wang, M. Negnevitsky, and C. Li, "An up-to-date review on the design improvement and optimization of the liquid-cooling battery thermal management system for electric vehicles," *Appl. Therm. Eng.*, vol. 219, p. 119626, Jan. 2023, doi: 10.1016/j.applthermaleng.2022.119626.

[20] A. G. Olabi *et al.*, "Battery thermal management systems: Recent progress and challenges," *Int. J. Thermofluids*, vol. 15, p. 100171, Aug. 2022, doi:

10.1016/j.ijft.2022.100171.

[21] V. Mali, R. Saxena, K. Kumar, A. Kalam, and B. Tripathi, “Review on battery thermal management systems for energy-efficient electric vehicles,” *Renew. Sustain. Energy Rev.*, vol. 151, p. 111611, Nov. 2021, doi: 10.1016/j.rser.2021.111611.

[22] S. M. Lukic, J. Cao, R. C. Bansal, F. Rodriguez, and A. Emadi, “Energy storage systems for automotive applications,” *IEEE Transactions on Industrial Electronics*, vol. 55, no. 6. pp. 2258–2267, 2008. doi: 10.1109/TIE.2008.918390.

[23] H. Budde-Meiwes *et al.*, “A review of current automotive battery technology and future prospects,” *Proc. Inst. Mech. Eng. Part D J. Automob. Eng.*, vol. 227, no. 5, pp. 761–776, May 2013, doi: 10.1177/0954407013485567.

[24] S. M. A. S. Bukhari, J. Maqsood, M. Q. Baig, S. Ashraf, and T. A. Khan, “Comparison of Characteristics-Lead Acid, Nickel Based, Lead Crystal and Lithium Based Batteries,” in *Proceedings - UKSim-AMSS 17th International Conference on Computer Modelling and Simulation, UKSim 2015*, Sep. 2016, pp. 444–450. doi: 10.1109/UKSim.2015.69.

[25] T. M. Bandhauer, S. Garimella, and T. F. Fuller, “A Critical Review of Thermal Issues in Lithium-Ion Batteries,” *J. Electrochem. Soc.*, vol. 158, no. 3, p. R1, Jan. 2011, doi: 10.1149/1.3515880.

[26] A. Pesaran, M. Keyser, G.-H. Kim, S. Santhanagopalan, and K. Smith, “Tools for Designing Thermal Management of Batteries in Electric Drive Vehicles,” Golden, Colorado, 2013.

[27] A. A. Pesaran, “Battery thermal models for hybrid vehicle simulations,” in *Journal of Power Sources*, Aug. 2002, vol. 110, no. 2, pp. 377–382. doi: 10.1016/S0378-7753(02)00200-8.

[28] R. Gogoana, “Internal resistance variances in lithium-ion batteries and implications in manufacturing,” 2012. https://dspace.mit.edu/handle/1721.1/74917 (accessed Jul. 27, 2023).

[29] Y. Ma, H. Mou, and H. Zhao, “Cooling optimization strategy for lithium-ion batteries based on triple-step nonlinear method,” *Energy*, vol. 201, p. 117678, Jun. 2020, doi: 10.1016/j.energy.2020.117678.

[30] G. Xia, L. Cao, and G. Bi, “A review on battery thermal management in electric

vehicle application," *Journal of Power Sources*, vol. 367. Elsevier B.V., pp. 90–105, Nov. 01, 2017. doi: 10.1016/j.jpowsour.2017.09.046.

[31] A. Pesaran, "Battery Thermal Management in EVs and HEVs : Issues and Solutions," 2001.

[32] Q. Wang, B. Jiang, B. Li, and Y. Yan, "A critical review of thermal management models and solutions of lithium-ion batteries for the development of pure electric vehicles," *Renewable and Sustainable Energy Reviews*, vol. 64. Elsevier Ltd, pp. 106–128, Oct. 01, 2016. doi: 10.1016/j.rser.2016.05.033.

[33] J. Kim, J. Oh, and H. Lee, "Review on battery thermal management system for electric vehicles," *Applied Thermal Engineering*, vol. 149. Elsevier Ltd, pp. 192–212, Feb. 25, 2019. doi: 10.1016/j.applthermaleng.2018.12.020.

[34] J. Xun, R. Liu, and K. Jiao, "Numerical and analytical modeling of lithium ion battery thermal behaviors with different cooling designs," *J. Power Sources*, vol. 233, pp. 47–61, Jul. 2013, doi: 10.1016/J.JPOWSOUR.2013.01.095.

[35] W. Li, Y. Xia, G. H. Chen, and E. Sahraei, "Comparative study of mechanical-electrical-thermal responses of pouch, cylindrical, and prismatic lithium-ion cells under mechanical abuse," *Sci. China Technol. Sci.*, vol. 61, no. 10, pp. 1472–1482, Oct. 2018, doi: 10.1007/S11431-017-9296-0/METRICS.

[36] T. Wang, K. J. Tseng, J. Zhao, and Z. Wei, "Thermal investigation of lithium-ion battery module with different cell arrangement structures and forced air-cooling strategies," *Appl. Energy*, vol. 134, pp. 229–238, Dec. 2014, doi: 10.1016/J.APENERGY.2014.08.013.

[37] D. Chen, J. Jiang, G. H. Kim, C. Yang, and A. Pesaran, "Comparison of different cooling methods for lithium ion battery cells," *Appl. Therm. Eng.*, vol. 94, pp. 846–854, Feb. 2016, doi: 10.1016/j.applthermaleng.2015.10.015.

[38] H. Wang, F. He, and L. Ma, "Experimental and modeling study of controller-based thermal management of battery modules under dynamic loads," *Int. J. Heat Mass Transf.*, vol. 103, pp. 154–164, Dec. 2016, doi: 10.1016/j.ijheatmasstransfer.2016.07.041.

[39] A. Lidbeck and K. R. Syed, "Experimental Characterization of Li-ion Battery cells for Thermal Management in Heavy Duty Hybrid Applications," *Chalmers*

University of Technology Gothenburg, 2017. http://publications.lib.chalmers.se/records/fulltext/252994/252994.pdf (accessed Jul. 27, 2023).

[40] N. Yang, X. Zhang, G. Li, and D. Hua, “Assessment of the forced air-cooling performance for cylindrical lithium-ion battery packs: A comparative analysis between aligned and staggered cell arrangements,” *Appl. Therm. Eng.*, vol. 80, pp. 55–65, Apr. 2015, doi: 10.1016/j.applthermaleng.2015.01.049.

[41] P. Nelson, D. Dees, K. Amine, and G. Henriksen, “Modeling thermal management of lithium-ion PNGV batteries,” in *Journal of Power Sources*, Aug. 2002, vol. 110, no. 2, pp. 349–356. doi: 10.1016/S0378-7753(02)00197-0.

[42] R. Schmidt, “Packaging of New Servers - Energy efficiency aspects,” *1st Berkeley Symposium on Energy Efficient Electronics*, 2009. https://e3s-center.berkeley.edu/wp-content/uploads/2017/07/RogerSchmidt.pdf (accessed Jul. 28, 2023).

[43] L. Zhu, R. F. Boehm, Y. Wang, C. Halford, and Y. Sun, “Water immersion cooling of PV cells in a high concentration system,” *Sol. Energy Mater. Sol. Cells*, vol. 95, no. 2, pp. 538–545, Feb. 2011, doi: 10.1016/j.solmat.2010.08.037.

[44] W. Yu and H. Xie, “A review on nanofluids: Preparation, stability mechanisms, and applications,” *J. Nanomater.*, vol. 2012, 2012, doi: 10.1155/2012/435873.

[45] Y. Xuan and Q. Li, “Heat transfer enhancement of nanofluids,” *Int. J. Heat Fluid Flow*, vol. 21, no. 1, pp. 58–64, Feb. 2000, doi: 10.1016/S0142-727X(99)00067-3.

[46] A. M. Sefidan, A. Sojoudi, and S. C. Saha, “Nanofluid-based cooling of cylindrical lithium-ion battery packs employing forced air flow,” *Int. J. Therm. Sci.*, vol. 117, pp. 44–58, Jul. 2017, doi: 10.1016/j.ijthermalsci.2017.03.006.

[47] L. Tran, J. Lopez, J. Lopez, A. Uriostegui, A. Barrera, and N. Wiggins, “Li-ion battery cooling system integrates in nano-fluid environment,” *Appl. Nanosci.*, vol. 7, no. 1–2, pp. 25–29, Feb. 2017, doi: 10.1007/s13204-016-0539-6.

[48] Y. Li, H. Xie, W. Yu, and J. Li, “Liquid cooling of tractive lithium ion batteries pack with nanofluids coolant,” *J. Nanosci. Nanotechnol.*, vol. 15, no. 4, pp. 3206–3211, Apr. 2015, doi: 10.1166/jnn.2015.9672.

[49] S. Wiriyasart, C. Hommalee, S. Sirikasemsuk, R. Prurapark, and P. Naphon,

“Thermal management system with nanofluids for electric vehicle battery cooling modules,” *Case Stud. Therm. Eng.*, vol. 18, p. 100583, Apr. 2020, doi: 10.1016/j.csite.2020.100583.

[50] G. Liang and I. Mudawar, “Review of single-phase and two-phase nanofluid heat transfer in macro-channels and micro-channels,” *Int. J. Heat Mass Transf.*, vol. 136, pp. 324–354, Jun. 2019, doi: 10.1016/J.IJHEATMASSTRANSFER.2019.02.086.

[51] M. Sheikholeslami, M. Gorji Bandpy, R. Ellahi, M. Hassan, and S. Soleimani, “Effects of MHD on Cu-water nanofluid flow and heat transfer by means of CVFEM,” *J. Magn. Magn. Mater.*, vol. 349, pp. 188–200, Jan. 2014, doi: 10.1016/j.jmmm.2013.08.040.

[52] A. Chu, Y. Yuan, J. Zhu, X. Lu, and C. Zhou, “The Design and Investigation of a Cooling System for a High Power Ni-MH Battery Pack in Hybrid Electric Vehicles,” *Appl. Sci.*, vol. 10, no. 5, p. 1660, Mar. 2020, doi: 10.3390/app10051660.

[53] S. Panchal, K. Gudlanarva, M.-K. Tran, R. Fraser, and M. Fowler, “High Reynold’s Number Turbulent Model for Micro-Channel Cold Plate Using Reverse Engineering Approach for Water-Cooled Battery in Electric Vehicles,” *Energies*, vol. 13, no. 7, Apr. 2020, doi: 10.3390/en13071638.

[54] Z. Ling, F. Wang, X. Fang, X. Gao, and Z. Zhang, “A hybrid thermal management system for lithium ion batteries combining phase change materials with forced-air cooling,” *Appl. Energy*, vol. 148, pp. 403–409, Jun. 2015, doi: 10.1016/J.APENERGY.2015.03.080.

[55] G. Zhang, L. Cao, S. Ge, C.-Y. Wang, C. E. Shaffer, and C. D. Rahn, “In Situ Measurement of Radial Temperature Distributions in Cylindrical Li-Ion Cells,” *J. Electrochem. Soc.*, vol. 161, no. 10, pp. A1499–A1507, Jul. 2014, doi: 10.1149/2.0051410jes.

[56] G. Karimi and X. Li, “Thermal management of lithium-ion batteries for electric vehicles,” *Int. J. Energy Res.*, vol. 37, no. 1, pp. 13–24, Jan. 2013, doi: 10.1002/er.1956.

[57] Z. Yu, J. Zhang, and W. Pan, “A review of battery thermal management systems about heat pipe and phase change materials,” *J. Energy Storage*, vol. 62, p. 106827, Jun. 2023, doi: 10.1016/J.EST.2023.106827.

[58] A. Kumar Thakur *et al.*, “A state-of-the art review on advancing battery thermal management systems for fast-charging,” *Appl. Therm. Eng.*, vol. 226, p. 120303, May 2023, doi: 10.1016/J.APPLTHERMALENG.2023.120303.

[59] J. Luo, D. Zou, Y. Wang, S. Wang, and L. Huang, “Battery thermal management systems (BTMs) based on phase change material (PCM): A comprehensive review,” *Chem. Eng. J.*, vol. 430, p. 132741, Feb. 2022, doi: 10.1016/j.cej.2021.132741.

[60] M. A. Abdelkareem *et al.*, “Battery thermal management systems based on nanofluids for electric vehicles,” *J. Energy Storage*, vol. 50, p. 104385, Jun. 2022, doi: 10.1016/J.EST.2022.104385.

[61] Q. L. Yue, C. X. He, M. C. Wu, and T. S. Zhao, “Advances in thermal management systems for next-generation power batteries,” *Int. J. Heat Mass Transf.*, vol. 181, p. 121853, Dec. 2021, doi: 10.1016/J.IJHEATMASSTRANSFER.2021.121853.

[62] G. Zhao, X. Wang, M. Negnevitsky, and H. Zhang, “A review of air-cooling battery thermal management systems for electric and hybrid electric vehicles,” *J. Power Sources*, vol. 501, p. 230001, Jul. 2021, doi: 10.1016/J.JPOWSOUR.2021.230001.

[63] Y. Huang, S. Wang, Y. Lu, R. Huang, and X. Yu, “Study on a liquid cooled battery thermal management system pertaining to the transient regime,” *Appl. Therm. Eng.*, vol. 180, p. 115793, Nov. 2020, doi: 10.1016/J.APPLTHERMALENG.2020.115793.

[64] Y. Fang, J. Shen, Y. Zhu, F. Ye, K. Li, and L. Su, “Investigation on the Transient Thermal Performance of a Mini-Channel Cold Plate for Battery Thermal Management,” *J. Therm. Sci. 2020 303*, vol. 30, no. 3, pp. 914–925, Aug. 2020, doi: 10.1007/S11630-020-1280-8.

[65] Y. Zhu, Y. Fang, L. Su, and F. Ye, “Experimental investigation of start-up and transient thermal performance of pumped two-phase battery thermal management system,” *Int. J. Energy Res.*, vol. 44, no. 14, pp. 11372–11384, Nov. 2020, doi: 10.1002/ER.5757.

[66] R. Mahamud and C. Park, “Reciprocating air flow for Li-ion battery thermal management to improve temperature uniformity,” *J. Power Sources*, vol. 196, no. 13, pp. 5685–5696, Jul. 2011, doi: 10.1016/j.jpowsour.2011.02.076.

[67] J. Zhang, X. Wu, K. Chen, D. Zhou, and M. Song, “Experimental and numerical

studies on an efficient transient heat transfer model for air-cooled battery thermal management systems," *J. Power Sources*, vol. 490, p. 229539, Apr. 2021, doi: 10.1016/J.JPOWSOUR.2021.229539.

[68] H. Wang, Z. Tao, Y. Fu, W. Li, and Y. Cai, "Analysis on Vibration of Li-ion Battery Module Used for Electric Vehicle," *DEStech Trans. Mater. Sci. Eng.*, vol. 0, no. icmsme, Apr. 2016, doi: 10.12783/DTMSE/ICMSME2016/7495.

[69] K. Shukla, A. R. M. Siddique, K. Venkateshwar, M. R. Mohaghegh, S. H. Tasnim, and S. Mahmud, "Experimental investigation on thermal field measurement of lithium-ion batteries under vibration," *J. Energy Storage*, vol. 53, p. 105110, Sep. 2022, doi: 10.1016/J.EST.2022.105110.

[70] W. Zhang, X. Li, W. Wu, and J. Huang, "Influence of mechanical vibration on composite phase change material based thermal management system for lithium-ion battery," *J. Energy Storage*, vol. 54, p. 105237, Oct. 2022, doi: 10.1016/J.EST.2022.105237.

[71] J. F. Lang and G. Kjell, "Comparing vibration measurements in an electric vehicle with standard vibration requirements for Li-ion batteries using power spectral density analysis," *Int. J. Electr. Hybrid Veh.*, vol. 7, no. 3, p. 272, 2015, doi: 10.1504/IJEHV.2015.071640.

[72] N. Joshy, M. Hajiyan, A. R. M. Siddique, S. Tasnim, H. Simha, and S. Mahmud, "Experimental investigation of the effect of vibration on phase change material (PCM) based battery thermal management system," *J. Power Sources*, vol. 450, p. 227717, Feb. 2020, doi: 10.1016/J.JPOWSOUR.2020.227717.

[73] H. J. Bergveld, W. S. Kruijt, and P. H. L. Notten, "Battery Management Systems," *Batter. Manag. Syst.*, vol. 1, Oct. 2002, doi: 10.1007/978-94-017-0843-2.

[74] S. Megahed and B. Scrosati, "Lithium-ion rechargeable batteries," *J. Power Sources*, vol. 51, no. 1–2, pp. 79–104, Aug. 1994, doi: 10.1016/0378-7753(94)01956-8.

[75] D. T. Sawyer, "Electrochemistry," *Encycl. Phys. Sci. Technol.*, pp. 161–197, Jan. 2003, doi: 10.1016/B0-12-227410-5/00206-4.

[76] Q. Zhang, D. Wang, B. Yang, X. Cui, and X. Li, "Electrochemical model of lithium-ion battery for wide frequency range applications," *Electrochim. Acta*, vol. 343, p.

136094, May 2020, doi: 10.1016/J.ELECTACTA.2020.136094.

[77] M. Doyle, T. F. Fuller, and J. Newman, “Modeling of Galvanostatic Charge and Discharge of the Lithium/Polymer/Insertion Cell,” *J. Electrochem. Soc.*, vol. 140, no. 6, pp. 1526–1533, Jun. 1993, doi: 10.1149/1.2221597.

[78] T. F. Fuller, M. Doyle, and J. Newman, “Simulation and Optimization of the Dual Lithium Ion Insertion Cell,” *J. Electrochem. Soc.*, vol. 141, no. 1, pp. 1–10, Jan. 1994, doi: 10.1149/1.2054684.

[79] Y. Ma, M. Yin, Z. Ying, and H. Chen, “Establishment and simulation of an electrode averaged model for a lithium-ion battery based on kinetic reactions,” *RSC Adv.*, vol. 6, no. 30, pp. 25435–25443, 2016, doi: 10.1039/C5RA27556C.

[80] T.-S. Dao, C. P. Vyasarayani, and J. McPhee, “Simplification and order reduction of lithium-ion battery model based on porous-electrode theory,” *J. Power Sources*, vol. 198, pp. 329–337, Jan. 2012, doi: 10.1016/j.jpowsour.2011.09.034.

[81] A. Pozzi, G. Ciaramella, S. Volkwein, and D. M. Raimondo, “Optimal Design of Experiments for a Lithium-Ion Cell: Parameters Identification of an Isothermal Single Particle Model with Electrolyte Dynamics,” *Ind. Eng. Chem. Res.*, vol. 58, no. 3, pp. 1286–1299, Jan. 2019, doi: 10.1021/acs.iecr.8b04580.

[82] E. Barsoukov and J. R. Macdonald, Eds., *Impedance Spectroscopy*. Wiley, 2005. doi: 10.1002/0471716243.

[83] S. Panchal, M. Mathew, R. Fraser, and M. Fowler, “Electrochemical thermal modeling and experimental measurements of 18650 cylindrical lithium-ion battery during discharge cycle for an EV,” *Appl. Therm. Eng.*, vol. 135, pp. 123–132, May 2018, doi: 10.1016/j.applthermaleng.2018.02.046.

[84] Y. Li, F. Qi, H. Guo, Z. Guo, M. Li, and W. Wu, “Characteristic investigation of an electrochemical-thermal coupled model for a LiFePO4/Graphene hybrid cathode lithium-ion battery,” *Case Stud. Therm. Eng.*, vol. 13, p. 100387, Mar. 2019, doi: 10.1016/J.CSITE.2018.100387.

[85] S. U. Kim, P. Albertus, D. Cook, C. W. Monroe, and J. Christensen, “Thermoelectrochemical simulations of performance and abuse in 50-Ah automotive cells,” *J. Power Sources*, vol. 268, pp. 625–633, Dec. 2014, doi: 10.1016/j.jpowsour.2014.06.080.

[86] F. Meng, L. Chen, and Z. Xie, “Numerical simulations and analyses on thermal characteristics of 18650 lithium-ion batteries with natural cooling conditions,” *Int. J. ENERGY Environ.*, vol. 8, no. 1, 2017.

[87] O. Reynolds, “IV. On the dynamical theory of incompressible viscous fluids and the determination of the criterion,” *Philos. Trans. R. Soc. London.*, vol. 186, pp. 123–164, Dec. 1895, doi: 10.1098/RSTA.1895.0004.

[88] S. B. Pope, *Turbulent Flows*. Cambridge University Press, 2000. doi: 10.1017/CBO9780511840531.

[89] Á. L. De Bortoli, G. S. L. Andreis, and F. N. Pereira, “Equations of Fluid Dynamics,” *Model. Simul. React. Flows*, pp. 35–51, Jan. 2015, doi: 10.1016/B978-0-12-802974-9.00003-9.

[90] P. Y. Chou, “On velocity correlations and the solutions of the equations of turbulent fluctuation,” *Q. Appl. Math.*, vol. 3, no. 1, pp. 38–54, 1945, doi: 10.1090/QAM/11999.

[91] C. C. Mei, “CHAPTER 4. THERMAL EFFECTS IN FLUIDS - Heat and energy conservation,” 2007. [Online]. Available: http://web.mit.edu/1.63/www/Lec-notes/chap4_heat_mass/4-1energy.pdf

[92] D. P. D. Theodore L. Bergman, Adrienne S. Lavine, Frank P. Incropera, *Fundamentals of Heat and Mass Transfer, 7th Edition*, 7th ed. USA: John Wiley & Sons, Inc., 2011.

[93] B. E. Launder and D. B. Spalding, “The numerical computation of turbulent flows,” *Comput. Methods Appl. Mech. Eng.*, vol. 3, no. 2, pp. 269–289, Mar. 1974, doi: 10.1016/0045-7825(74)90029-2.

[94] T. H. Shih, W. W. Liou, A. Shabbir, Z. Yang, and J. Zhu, “A new k-ϵ eddy viscosity model for high reynolds number turbulent flows,” *Comput. Fluids*, vol. 24, no. 3, pp. 227–238, Mar. 1995, doi: 10.1016/0045-7930(94)00032-T.

[95] ANSYS, “ANSYS FLUENT 19.0 Theory Guide - Realizable Model,” USA.

[96] The OpenFOAM Foundation, “realizableKE - C++ Source Code Guide.” [Online]. Available: https://cpp.openfoam.org/v11/classFoam_1_1RASModels_1_1realizableKE.html

[97] J. O. Hinze, *Turbulence*, 2nd ed. New York: McGraw-Hill Book Co., 1975.

[98] ANSYS, “ANSYS FLUENT 19.0 Theory Guide - Spatial Discretization.”

[99] CFD Direct, “CFD Direct - OpenFOAM V8 User Guide - 4.5 Numerical Schemes.” [Online]. Available: https://doc.cfd.direct/openfoam/user-guide-v8/fvschemes

[100] Siemens, “Simcenter STAR-CCM+ - Help? - Second-order temporal discretization.”

[101] CFD Online, “Approximation Schemes for convective term - structured grids - Common -- CFD-Wiki, the free CFD reference.” https://www.cfd-online.com/Wiki/Approximation_Schemes_for_convective_term_-_structured_grids_-_Common (accessed Aug. 08, 2023).

[102] J. Blazek, “Consistency, Accuracy and Stability,” in *Computational Fluid Dynamics: Principles and Applications*, Elsevier, 2005, pp. 351–371. doi: 10.1016/B978-008044506-9/50012-6.

[103] S. V. Patankar, *Numerical Heat Transfer and Fluid Flow*. CRC Press, 2018. doi: 10.1201/9781482234213.

[104] O. Zikanov, *Essential Computational Fluid Dynamics*. John Wiley & Sons, Ltd, 2019.

[105] D. S. Kershaw, “The incomplete Cholesky—conjugate gradient method for the iterative solution of systems of linear equations,” *J. Comput. Phys.*, vol. 26, no. 1, pp. 43–65, Jan. 1978, doi: 10.1016/0021-9991(78)90098-0.

[106] M. H. Malekshah, E. H. Malekshah, M. Salari, A. Rahimi, M. Rahjoo, and A. Kasaeipoor, “Thermal analysis of a cell of lead-acid battery subjected by non-uniform heat flux during natural convection,” *Therm. Sci. Eng. Prog.*, vol. 5, pp. 317–326, Mar. 2018, doi: 10.1016/j.tsep.2018.01.004.

[107] T. H. Tran, S. Harmand, B. Desmet, and S. Filangi, “Experimental investigation on the feasibility of heat pipe cooling for HEV/EV lithium-ion battery,” *Appl. Therm. Eng.*, vol. 63, no. 2, pp. 551–558, Feb. 2014, doi: 10.1016/j.applthermaleng.2013.11.048.

[108] S. Panchal, I. Dincer, M. Agelin-Chaab, R. Fraser, and M. Fowler, “Design and simulation of a lithium-ion battery at large C-rates and varying boundary conditions through heat flux distributions,” *Meas. J. Int. Meas. Confed.*, vol. 116, pp. 382–390, Feb. 2018, doi: 10.1016/j.measurement.2017.11.038.

[109] K. A. Murashko, A. V. Mityakov, J. Pyrhönen, V. Y. Mityakov, and S. S.

Sapozhnikov, “Thermal parameters determination of battery cells by local heat flux measurements,” *J. Power Sources*, vol. 271, pp. 48–54, Aug. 2014, doi: 10.1016/j.jpowsour.2014.07.117.

[110] S. J. Drake *et al.*, “Heat generation rate measurement in a Li-ion cell at large C-rates through temperature and heat flux measurements,” *J. Power Sources*, vol. 285, pp. 266–273, Jul. 2015, doi: 10.1016/j.jpowsour.2015.03.008.

[111] Tesla Motors Patent US 8286743, “Vehicle battery pack ballistic shield,” Dec. 05, 2012 Accessed: Sep. 12, 2020. [Online]. Available: http://www.patentlens.net/patentlens/patents.html?patnums=US_8286743

[112] L. O. Valøen and M. I. Shoesmith, “The effect of PHEV and HEV duty cycles on battery and battery pack performance,” *Plug-in hybrid Veh. Conf.*, no. April, pp. 1–9, 2007, Accessed: Sep. 12, 2020. [Online]. Available: https://www.osti.gov/etdeweb/biblio/21007769

[113] X. M. Xu and R. He, “Research on the heat dissipation performance of battery pack based on forced air cooling,” *J. Power Sources*, vol. 240, pp. 33–41, Oct. 2013, doi: 10.1016/J.JPOWSOUR.2013.03.004.

[114] J. Zhao, Z. Rao, and Y. Li, “Thermal performance of mini-channel liquid cooled cylinder based battery thermal management for cylindrical lithium-ion power battery,” *Energy Convers. Manag.*, vol. 103, pp. 157–165, Oct. 2015, doi: 10.1016/J.ENCONMAN.2015.06.056.

[115] C. Lan, J. Xu, Y. Qiao, and Y. Ma, “Thermal management for high power lithium-ion battery by minichannel aluminum tubes,” *Appl. Therm. Eng.*, vol. 101, pp. 284–292, May 2016, doi: 10.1016/J.APPLTHERMALENG.2016.02.070.

[116] A. Jarrett and I. Y. Kim, “Design optimization of electric vehicle battery cooling plates for thermal performance,” *J. Power Sources*, vol. 196, no. 23, pp. 10359–10368, Dec. 2011, doi: 10.1016/J.JPOWSOUR.2011.06.090.

[117] M. Sheikholeslami, M. Gorji Bandpy, R. Ellahi, M. Hassan, and S. Soleimani, “Effects of MHD on Cu–water nanofluid flow and heat transfer by means of CVFEM,” *J. Magn. Magn. Mater.*, vol. 349, pp. 188–200, Jan. 2014, doi: 10.1016/J.JMMM.2013.08.040.

[118] M. Sheikholeslami, D. D. Ganji, and H. R. Ashorynejad, “Investigation of squeezing

unsteady nanofluid flow using ADM," *Powder Technol.*, vol. 239, pp. 259–265, May 2013, doi: 10.1016/j.powtec.2013.02.006.

[119] M. Malý, A. S. Moita, J. Jedelsky, A. P. C. Ribeiro, and A. L. N. Moreira, "Effect of nanoparticles concentration on the characteristics of nanofluid sprays for cooling applications," *J. Therm. Anal. Calorim.*, vol. 135, no. 6, pp. 3375–3386, Mar. 2019, doi: 10.1007/s10973-018-7444-z.

[120] M. H. U. Bhuiyan, R. Saidur, M. A. Amalina, R. M. Mostafizur, and A. Islam, "Effect of Nanoparticles Concentration and Their Sizes on Surface Tension of Nanofluids," *Procedia Eng.*, vol. 105, pp. 431–437, 2015, doi: 10.1016/j.proeng.2015.05.030.

[121] M. Torabi, N. Karimi, M. Torabi, G. P. Peterson, and C. J. Simonson, "Generation of entropy in micro thermofluidic and thermochemical energy systems-A critical review," *International Journal of Heat and Mass Transfer*, vol. 163. Elsevier Ltd, p. 120471, Dec. 01, 2020. doi: 10.1016/j.ijheatmasstransfer.2020.120471.

[122] R. Habib, N. Karimi, B. Yadollahi, M. H. Doranehgard, and L. K. B. Li, "A pore-scale assessment of the dynamic response of forced convection in porous media to inlet flow modulations," *Int. J. Heat Mass Transf.*, vol. 153, p. 119657, Jun. 2020, doi: 10.1016/j.ijheatmasstransfer.2020.119657.

[123] S. W. Churchill and M. Bernstein, "A correlating equation for forced convection from gases and liquids to a circular cylinder in crossflow," *J. Heat Transfer*, vol. 99, no. 2, pp. 300–306, May 1977, doi: 10.1115/1.3450685.

[124] Y. Patel, "Numerical Investigation of Flow Past a Circular Cylinder and in a Staggered Tube Bundle Using Various Turbulence Models," Lappeenranta University of Technology, 2010. Accessed: Sep. 12, 2020. [Online]. Available: https://lutpub.lut.fi/handle/10024/63863

[125] R. Hilpert, "Wärmeabgabe von geheizten Drähten und Rohren im Luftstrom," *Forsch. auf dem Gebiete des Ingenieurwesens*, vol. 4, no. 5, pp. 215–224, Sep. 1933, doi: 10.1007/BF02719754.

[126] S. Whitaker, "Forced convection heat transfer correlations for flow in pipes, past flat plates, single cylinders, single spheres, and for flow in packed beds and tube bundles," *AIChE J.*, vol. 18, no. 2, pp. 361–371, Mar. 1972, doi: 10.1002/aic.690180219.

[127] E. D. Grimson, “Correlation and utilization of new data on flow resistance and heat transfer cross-flow of gases over tube banks,” *Trans. ASME*, vol. 59, pp. 583–594, 1937, Accessed: Sep. 12, 2020. [Online]. Available: https://ci.nii.ac.jp/naid/10009523716/

[128] K. Ogata, *System Dynamics*, 4th ed. Pearson, 2004. Accessed: Sep. 13, 2020. [Online]. Available: https://www.pearson.com/us/higher-education/program/Ogata-System-Dynamics-4th-Edition/PGM257440.html

[129] K. Ogata, *Modern Control Engineering*, 5th ed. Pearson, 2010. Accessed: Sep. 13, 2020. [Online]. Available: https://www.pearson.com/us/higher-education/program/Ogata-Modern-Control-Engineering-5th-Edition/PGM100186.html

[130] R. H. Bishop and R. C. Dorf, *Modern Control Systems*, 13th ed. Boston, MA: Pearson, 2016.

[131] N. Karimi, “Response of a conical, laminar premixed flame to low amplitude acoustic forcing - A comparison between experiment and kinematic theories,” *Energy*, vol. 78, pp. 490–500, Dec. 2014, doi: 10.1016/j.energy.2014.10.036.

[132] K. R. McManus, T. Poinsot, and S. M. Candel, “A review of active control of combustion instabilities,” *Progress in Energy and Combustion Science*, vol. 19, no. 1. Pergamon, pp. 1–29, Jan. 01, 1993. doi: 10.1016/0360-1285(93)90020-F.

[133] R. Habib, B. Yadollahi, N. Karimi, and M. H. Doranegard, “On the unsteady forced convection in porous media subject to inlet flow disturbances-A pore-scale analysis,” *Int. Commun. Heat Mass Transf.*, vol. 116, p. 104639, Jul. 2020, doi: 10.1016/j.icheatmasstransfer.2020.104639.

[134] T. B. Greenslade, *Adventures with Lissajous Figures*. Morgan & Claypool Publishers, 2018.

[135] W. H. MOASE, M. J. BREAR, and C. MANZIE, “The forced response of choked nozzles and supersonic diffusers,” *J. Fluid Mech.*, vol. 585, pp. 281–304, Aug. 2007, doi: 10.1017/S0022112007006647.

[136] G. N. Bochkov and I. E. Kuzovlev, “General theory of thermal fluctuations in nonlinear systems,” *Zhurnal Eksp. i Teor. Fiz.*, vol. 72, pp. 238–247, 1977.

[137] D. A. Tortorelli, R. B. Haber, and S. C.-Y. Lu, “Design sensitivity analysis for

nonlinear thermal systems," *Comput. Methods Appl. Mech. Eng.*, vol. 77, no. 1–2, pp. 61–77, Dec. 1989, doi: 10.1016/0045-7825(89)90128-X.

[138] V. G. Choudhari, A. S. Dhoble, and S. Panchal, "Numerical analysis of different fin structures in phase change material module for battery thermal management system and its optimization," *Int. J. Heat Mass Transf.*, vol. 163, p. 120434, Dec. 2020, doi: 10.1016/j.ijheatmasstransfer.2020.120434.

[139] R.-G. Chi, W.-S. Chung, and S.-H. Rhi, "Thermal Characteristics of an Oscillating Heat Pipe Cooling System for Electric Vehicle Li-Ion Batteries," *Energies*, vol. 11, no. 3, p. 655, Mar. 2018, doi: 10.3390/en11030655.

[140] T. Amalesh and N. L. Narasimhan, "Introducing new designs of minichannel cold plates for the cooling of Lithium-ion batteries," *J. Power Sources*, vol. 479, p. 228775, Dec. 2020, doi: 10.1016/j.jpowsour.2020.228775.

[141] W. Wu, X. Xiao, and X. Huang, "The effect of battery design parameters on heat generation and utilization in a Li-ion cell," *Electrochim. Acta*, vol. 83, pp. 227–240, Nov. 2012, doi: 10.1016/J.ELECTACTA.2012.07.081.

[142] V. G. Choudhari, D. A. S. Dhoble, and T. M. Sathe, "A review on effect of heat generation and various thermal management systems for lithium ion battery used for electric vehicle," *J. Energy Storage*, vol. 32, p. 101729, Dec. 2020, doi: 10.1016/J.EST.2020.101729.

[143] Y. Wei and M. Agelin-Chaab, "Development and experimental analysis of a hybrid cooling concept for electric vehicle battery packs," *J. Energy Storage*, vol. 25, p. 100906, Oct. 2019, doi: 10.1016/j.est.2019.100906.

[144] "Ansys FAQ - CFD-Wiki." https://www.cfd-online.com/Wiki/Ansys_FAQ (accessed May 05, 2022).

[145] T. J. Barlow, S. Latham, I. S. Mccrae, and P. G. Boulter, "A reference book of driving cycles for use in the measurement of road vehicle emissions," Jun. 2009.

[146] "United States Environmental Protection Agency - Dynamometer Drive Schedules," 2022. https://www.epa.gov/vehicle-and-fuel-emissions-testing/dynamometer-drive-schedules#:~:text=The New York City Cycle,-and-go traffic conditions.&text=New York City Cycle Driving,%22Supplemental FTP%22 driving schedule. (accessed Jun. 07, 2022).

[147] V. Muenzel *et al.*, “A Comparative Testing Study of Commercial 18650-Format Lithium-Ion Battery Cells,” *J. Electrochem. Soc.*, vol. 162, no. 8, pp. A1592–A1600, May 2015, doi: 10.1149/2.0721508JES/XML.

[148] A. Barai, K. Uddin, W. D. Widanage, A. McGordon, and P. Jennings, “A study of the influence of measurement timescale on internal resistance characterisation methodologies for lithium-ion cells,” *Sci. Reports 2017 81*, vol. 8, no. 1, pp. 1–13, Jan. 2018, doi: 10.1038/s41598-017-18424-5.

[149] K. An, P. Barai, K. Smith, and P. P. Mukherjee, “Probing the Thermal Implications in Mechanical Degradation of Lithium-Ion Battery Electrodes,” *J. Electrochem. Soc.*, vol. 161, no. 6, pp. A1058–A1070, May 2014, doi: 10.1149/2.069406jes.

[150] J. M. Hooper, J. Marco, G. H. Chouchelamane, C. Lyness, and J. Taylor, “Vibration Durability Testing of Nickel Cobalt Aluminum Oxide (NCA) Lithium-Ion 18650 Battery Cells,” *Energies 2016, Vol. 9, Page 281*, vol. 9, no. 4, p. 281, Apr. 2016, doi: 10.3390/EN9040281.

[151] T. Bruen, J. M. Hooper, J. Marco, M. Gama, and G. H. Chouchelamane, “Analysis of a Battery Management System (BMS) Control Strategy for Vibration Aged Nickel Manganese Cobalt Oxide (NMC) Lithium-Ion 18650 Battery Cells,” *Energies 2016, Vol. 9, Page 255*, vol. 9, no. 4, p. 255, Apr. 2016, doi: 10.3390/EN9040255.

[152] R. Gogoana, M. B. Pinson, M. Z. Bazant, and S. E. Sarma, “Internal resistance matching for parallel-connected lithium-ion cells and impacts on battery pack cycle life,” *J. Power Sources*, vol. 252, pp. 8–13, Apr. 2014, doi: 10.1016/J.JPOWSOUR.2013.11.101.

[153] D. Wang, Y. Bao, and J. Shi, “Online Lithium-Ion Battery Internal Resistance Measurement Application in State-of-Charge Estimation Using the Extended Kalman Filter,” *Energies*, vol. 10, no. 9, p. 1284, Aug. 2017, doi: 10.3390/en10091284.

[154] L. Chen, Z. Lü, W. Lin, J. Li, and H. Pan, “A new state-of-health estimation method for lithium-ion batteries through the intrinsic relationship between ohmic internal resistance and capacity,” *Measurement*, vol. 116, pp. 586–595, Feb. 2018, doi: 10.1016/J.MEASUREMENT.2017.11.016.

[155] D. J. Noelle, M. Wang, A. V. Le, Y. Shi, and Y. Qiao, “Internal resistance and

polarization dynamics of lithium-ion batteries upon internal shorting," *Appl. Energy*, vol. 212, pp. 796–808, Feb. 2018, doi: 10.1016/J.APENERGY.2017.12.086.

[156] L. Sun, G. Li, and F. You, "Combined internal resistance and state-of-charge estimation of lithium-ion battery based on extended state observer," *Renew. Sustain. Energy Rev.*, vol. 131, p. 109994, Oct. 2020, doi: 10.1016/J.RSER.2020.109994.

[157] L. Christodoulou, N. Karimi, A. Cammarano, M. Paul, and S. Navarro-Martinez, "State prediction of an entropy wave advecting through a turbulent channel flow," *J. Fluid Mech.*, vol. 882, Jan. 2020, doi: 10.1017/JFM.2019.799.

[158] J. P. (Jack P. Holman, *Heat transfer*, 10th ed. New York: McGraw Hill Higher Education, 2010.

[159] T.-T. Tay, I. Mareels, and J. B. Moore, *High Performance Control*. Boston, MA: Birkhäuser Boston, 1998. doi: 10.1007/978-1-4612-1786-2.

[160] K. Ogata, *Discrete-time control systems*. Prentice-Hall, 1987.

[161] I. S. Suh, H. Cho, and M. Lee, "Feasibility study on thermoelectric device to energy storage system of an electric vehicle," *Energy*, vol. 76, pp. 436–444, Nov. 2014, doi: 10.1016/J.ENERGY.2014.08.040.

[162] H. Liu, Z. Wei, W. He, and J. Zhao, "Thermal issues about Li-ion batteries and recent progress in battery thermal management systems: A review," *Energy Convers. Manag.*, vol. 150, pp. 304–330, Oct. 2017, doi: 10.1016/j.enconman.2017.08.016.

[163] C. Bibin, M. Vijayaram, V. Suriya, R. Sai Ganesh, and S. Soundarraj, "A review on thermal issues in Li-ion battery and recent advancements in battery thermal management system," *Mater. Today Proc.*, vol. 33, pp. 116–128, 2020, doi: 10.1016/j.matpr.2020.03.317.

[164] A. G. Kravchenko and P. Moin, "Numerical studies of flow over a circular cylinder at ReD=3900," *Phys. Fluids*, vol. 12, no. 2, pp. 403–417, Feb. 2000, doi: 10.1063/1.870318.

[165] P. Parnaudeau, J. Carlier, D. Heitz, and E. Lamballais, "Experimental and numerical studies of the flow over a circular cylinder at Reynolds number 3900," *Phys. Fluids*, vol. 20, no. 8, Aug. 2008, doi: 10.1063/1.2957018.

[166] J. E. Cooper, "AEROELASTIC RESPONSE," in *Encyclopedia of Vibration*,

Elsevier, 2001, pp. 87–97. doi: 10.1006/rwvb.2001.0125.

[167] X. M. Xu and R. He, “Research on the heat dissipation performance of battery pack based on forced air cooling,” *J. Power Sources*, vol. 240, pp. 33–41, Oct. 2013, doi: 10.1016/j.jpowsour.2013.03.004.

[168] R. S. Patil and V. A. Juvekar, “Analysis of multiparticle bipolar electrolysis using single particle cell model,” *Chem. Eng. Sci.*, vol. 110, pp. 72–82, May 2014, doi: 10.1016/j.ces.2013.12.003.

[169] V. Ramadesigan, P. W. C. Northrop, S. De, S. Santhanagopalan, R. D. Braatz, and V. R. Subramanian, “Modeling and Simulation of Lithium-Ion Batteries from a Systems Engineering Perspective,” *J. Electrochem. Soc.*, vol. 159, no. 3, pp. R31–R45, Jan. 2012, doi: 10.1149/2.018203jes.

[170] J. Jaguemont, L. Boulon, and Y. Dubé, “A comprehensive review of lithium-ion batteries used in hybrid and electric vehicles at cold temperatures,” *Appl. Energy*, vol. 164, pp. 99–114, Feb. 2016, doi: 10.1016/j.apenergy.2015.11.034.

[171] G. Steinbuss, B. Rzepka, S. Bischof, T. Blank, and K. Böhm, “FOBSS: Monitoring data from a modular battery system,” *e-Energy 2019 - Proc. 10th ACM Int. Conf. Futur. Energy Syst.*, pp. 456–459, Jun. 2019, doi: 10.1145/3307772.3331020.

[172] G. dos Reis, C. Strange, M. Yadav, and S. Li, “Lithium-ion battery data and where to find it,” *Energy AI*, vol. 5, p. 100081, Sep. 2021, doi: 10.1016/J.EGYAI.2021.100081.

[173] A. Placzek, J. F. Sigrist, and A. Hamdouni, “Numerical simulation of an oscillating cylinder in a cross-flow at low Reynolds number: Forced and free oscillations,” *Comput. Fluids*, vol. 38, no. 1, pp. 80–100, Jan. 2009, doi: 10.1016/J.COMPFLUID.2008.01.007.

[174] D. Karanth, G. W. Rankin, and K. Sridhar, “A finite difference calculation of forced convective heat transfer from an oscillating cylinder,” *Int. J. Heat Mass Transf.*, vol. 37, no. 11, pp. 1619–1630, Jul. 1994, doi: 10.1016/0017-9310(94)90177-5.

[175] W. S. Fu and B. H. Tong, “Numerical investigation of heat transfer from a heated oscillating cylinder in a cross flow,” *Int. J. Heat Mass Transf.*, vol. 45, no. 14, pp. 3033–3043, Jul. 2002, doi: 10.1016/S0017-9310(02)00016-9.

[176] K. M. SANTOSH, A. ARUN, and H. CHANDRA, “APPLICATION OF

VIBRATION ON HEAT TRANSFER - A REVIEW," *i-manager's J. Futur. Eng. Technol.*, vol. 15, no. 1, p. 72, 2019, doi: 10.26634/jfet.15.1.15877.

[177] U. Roy and P. K. Roy, "Advances in heat intensification techniques in shell and tube heat exchanger," in *Advanced Analytic and Control Techniques for Thermal Systems with Heat Exchangers*, Elsevier, 2020, pp. 197–207. doi: 10.1016/B978-0-12-819422-5.00007-4.

[178] W. Wu, J. Wang, and Z. Hu, "Study on the flow-induced vibration of a two-tandem cylinder system in rigid body motion," *Phys. Fluids*, vol. 34, no. 1, Jan. 2022, doi: 10.1063/5.0077090.

[179] A. S. Berman, T. S. Lundgren, and A. Cheng, "Asynchronous whirl in a rotating cylinder partially filled with liquid," *J. Fluid Mech.*, vol. 150, pp. 311–327, Jan. 1985, doi: 10.1017/S0022112085000143.

Appendix

Appendix A – Post-processing code

A1 – FFT

```
% FFT analysis of battery analysis under fluctuationg loads
% Written by: Ali Saeed - 2140637
% Writing start date: 17/05/20

% Clear variables, workspace and close all open windows
clear
clc
close all
% Store all variables with 32 bit precision
format long;

allfolders = dir('C:\Users\aligs\Desktop\MATLAB\Fres'); %Main folder for all
case files
for k = 3:length(allfolders) %Starts from real folders by point 3
    myfolder = allfolders(k).name; %Finds the name of the folder
    myfolder = fullfile(allfolders(k).folder,myfolder);%Finds full file
name/file path
    cd(myfolder)%change directory to main folder
    sub = strcat(myfolder,'\T'); %Add \T to original file name
    cd(sub) %Enter one of the Folders
    csvfiles = dir('*.csv'); %Read CSV Files

    for file = csvfiles' %Loop over all CSV Files
        fprintf(1,'Working with %s\n',file.name) %Tracks the file we are
working with and displays it
        fullFileName = fullfile(sub,file.name); %Identifies File patch
        str = file.name; %Identifies File name
        dat = csvread(fullFileName,1,0); %Reads data in File skipping 3 rows &
0 coloumns
        Fs = 1.0/(dat(2,1)-dat(1,1));
        fname = str(1:i);

        time = dat(int32(25*Fs)+1:int32(125*Fs),1); %Calculates time increments
of 1 cell from 25-125
        time = time'; %Inverse Time cells
        data = dat(int32(25*Fs)+1:int32(125*Fs),2:7); %Calculates Nu in
increments 1 cell in increments of 1 cell increase 25-125
        data = data'; %Inverse Nu Data
        [rows,columns] = size(data); %Calculates the size of rows & coloumns
pores for Nu
        T = 1/Fs; % Calculates Sampling period
        L = columns; % Calculates Length of signal by using size of coloumns
        n = 2^nextpow2(L); %Calculates the positive next powers of 2
        fname1 = strcat(fname,'_Time'); fname2 = fname1; %File name suffix
_Time is added
        fname1 = fullfile('C:\Users\aligs\Desktop\MATLAB\Fres',fname1);
%Filepath where first file is saved
        fname2 = fullfile(sub,fname2);

        time2 = dat(int32(32*Fs)+1:int32(40*Fs),1); %Calculates time increments
of 1 cell from 25-125
        time2 = time2-min(time2);
        time2 = time2'; %Inverse Time cells
```

```
        data2 = dat(int32(32*Fs)+1:int32(40*Fs),2:7); %Calculates Nu in
increments 1 cell in increments of 1 cell increase 25-125
        data2 = data2'; %Inverse Nu Data
        figure('units','normalized','outerposition',[0 0 1 1],'Visible','off');
        set(gcf,'CreateFcn','set(gcf,''Visible'',''on'')');
        mark = ['r-*'; 'y-+'; 'b-o'; 'k-p'; 'k-s'; 'g-d'];
        mark2 = ['r'; 'y'; 'b'; 'k'; 'k'; 'g'];
        for i = [1,3,6]
            txt = ['Cell ',num2str(i)];
            time2 = time2/max(time2);
            data2(i,:) = data2(i,:)/mean(data2(i,:));

plot(time2,data2(i,:),mark(i,:),'MarkerIndices',1:200:length(data2(i,:)),'Displ
ayName',txt,'LineWidth',1.1) %Plots Nu of each pore with time in 6 different
plots
            ylabel('Normalised Nu')
            xlabel('Normalised Time')
            hold on
        end
        ax = gca;
        ax.FontSize = 22;
        ax.LineWidth = 1.2;
        pbaspect([1 1 1])
        legend('show','orientation','vertical','FontSize',18);
        saveas(gcf,fname1,'tiff')
        hold off

        figure('units','normalized','outerposition',[0 0 1 1],'Visible','off');
        set(gcf,'CreateFcn','set(gcf,''Visible'',''on'')');
        xx = Fs*(0:(L/2))/L; %Calculating the Frequency Domain
        xxtick = 0:0.25:2;
        j = 1;
        for i = [1,3,6]
            data(i,:) = data(i,:)/mean(data(i,:)); %Nu Numbers (Output) at each
pore normalized (Around 1)
            data(i,:) = data(i,:)-mean(data(i,:)); %Nu Number (Output) at each
pore normalized (Around 0)
            yy = fft(data(i,:)); %Calculates the Discrete Fourier Transform
            pp2 = abs(yy/L); %Calculates the two-sided spectrum PP2
            pp1 = pp2(1:L/2+1); %Calculates the single-sided spectrum PP1 based
on PP2
            pp1(2:end-1) = 2*pp1(2:end-1);
            subplot(3,1,j)
            txt = ['Cell ',num2str(i)];
            plot(xx,pp1,mark2(i,:),'DisplayName',txt,'LineWidth',1.1)
            set(gca,'XLim',[0,2]);
            set(gca,'XTick',xxtick)
            set(gca,'YLim',[0,0.025]);
            ax = gca;
            ax.FontSize = 22;
            ax.LineWidth = 1.2;
            pbaspect([3.5 1 0.5])
            ylabel('Spectra')
            xlabel('Freq (Hz)')
            legend('show','orientation','vertical','FontSize',18);
            j = j+1;
        end
        fname1 = strcat(fname,'_FFT');
        fname1 = fullfile('C:\Users\aligs\Desktop\MATLAB\Fres',fname1);
        saveas(gcf,fname1,'tiff')
    end
    cd ..
```

```
end
cd ..\..
```

A2 – Transfer functions

```
% Time-Delay analysis of battery analysis under fluctuationg loads
% Written by: Ali Saeed - 2140637
% Writing start date: 17/05/20

% Clear variables, workspace and close any open windows
clear
clc
close all
% Store all variables with 32 bit precision
format long;

allfolders = dir('C:\Users\aligs\Desktop\MATLAB\Fres'); %Main folder for all
case files
for k = 3:length(allfolders) %Starts from real folders by point 3
    myfolder = allfolders(k).name; %Finds the name of the folder
    myfolder = fullfile(allfolders(k).folder,myfolder);%Finds full file
name/file path
    cd(myfolder)%change directory to main folder
    sub = strcat(myfolder,'\T'); %Add \T to original file name
    cd(sub) %Enter one of the Folders
    csvfiles = dir('*.csv'); %Read CSV Files
    j = 0; %Start Counter
    am = 0.1;

    for file = csvfiles' %Loop over all CSV Files
        fprintf(1,'Working with %s\n',file.name) %Tracks the file we are
working with and displays it
        fullFileName = fullfile(sub,file.name); %Identifies File patch
        str = file.name; %Identifies File name
        dat = csvread(fullFileName,1,0); %Reads data in File skipping 3 rows &
0 coloumns
        j = j+1; %Read one & add  to counter
        Fs = 1.0/(dat(2,1)-dat(1,1));
        Fr = input('Forcing Frequency = /n');
        fname = str(1:i);

        velocity = 30; %Velocity of the fluid
        diameter = 0.04; %Diameter of the battery cells
        st = (Fr*diameter)/velocity; %Strouhal Number (Normalised Frequency)

        time1 = dat(int32(0*Fs)+1:int32(125*Fs),1); %Calculates increments of 1
cell from 0-125
        %Used for calculating time lag
        time2 = dat(int32(25*Fs)+1:int32(125*Fs),1); %Calculates increments of
1 cell from 25-125
        %Used for amplitude analysis
        data1 = dat(int32(0*Fs)+1:int32(125*Fs),2:7); %Calculates Nu in
increments 1 cell increase 0-125
        %Used for calculating time lag
        data2 = dat(int32(25*Fs)+1:int32(125*Fs),2:7); %Calculates Nu in
increments 1 cell increase 25-125
        %Used for amplitude analysis
        time1 = time1'; %Inverse Time1
```

```
        time2 = time2'; %Inverse Time2
        data1 = data1'; %Inverse Nu Data1
        data2 = data2'; %Inverse Nu Data2

        [rows,columns] = size(data1); %Calculates the size of rows & coloumns
pores for Nu (0-125)
        T = 1/Fs;    % Calculates Sampling period
        L = columns; % Calculates Length of signal by using size of coloumns
        n = 2^nextpow2(L); %Calculates the positive next powers of 2

        aa = 1.0+am*sin(2.0*pi*Fr*time1); %Input flow signal (inlet - 0-125)
        aa = aa/mean(aa); %Normalized signal (Around 1 - 0-125)
        bb = 1.0+am*sin(2.0*pi*Fr*time2); %Input flow signal (inlet - 25-125)
        bb = bb/mean(bb); %Normalized signal (Around 1 - 25 - 125)
        for i = 1:6 %Loop over the 6 cells
            cc = data1(i,:)/mean(data1(i,:)); %Nu Numbers (Output) at each pore
normalized (Around 1 - 0-125)
            dd = data2(i,:)/mean(data2(i,:)); %Nu Numbers (Output) at each pore
normalized (Around 1 - 25-125)
            aa = aa-mean(aa); %Input flow signal normalized (Around 0 - 0-125)
            bb = bb-mean(bb); %Input flow signal normalized (Around 0 - 25-125)
            cc = cc-mean(cc); %Nu Numbers (Output) at each pore normalized
(Around 0 - 0-125)
            dd = dd-mean(dd); %Nu Numbers (Output) at each pore normalized
(Around 0 - 25-125)
            amplit(i) = rms(dd)/rms(bb); %Amplitude Output/Input flow Ratio for
all particles (25-125)
            [acor,lag] = xcorr(aa,cc); %cross correlation of input and output
signal (0-125)
            [~,I] = max((acor)); %calculates the maximum of the cross
correlation (When lag equals the delay)
            lagDiff = lag(I); %Lag difference between 2 signals
            timeDiff = (abs(lagDiff))/Fs; %Time difference between 2 signals
            phaselag(j,i) = timeDiff*2.0*180.0*Fr; %Convert phase lag signal in
Angles degrees

            H=0.05; %Defining the distance from the inlet to the first particle
            if i == 1 %Calculating the distance between each particle from
inlet onwards
                dist = 1*H;
            elseif i == 2
                dist = 3*H;
            elseif i == 3
                dist = 5*H;
            elseif i == 4
                dist = 7*H;
            elseif i == 5
                dist = 9*H;
            elseif i == 6
                dist = 11*H;
            end

            timeDiff=timeDiff/(dist/velocity); %Non-Dimensionalising time
Difference using velocity and cell distance
            res1(j,i) = amplit(i); %Amplitude Ratio for all 8 Frequencies
across all cells (25-125)
            res3(j,i)= timeDiff; %Time delay/Lag for all 8 Frequencies across
all cells (0-125)
        end
        freq(j) = st; %8 Frequency Values (Now Strouhal Number)
    end
```

```
    freq=freq/max(freq); %Normalises the Strouhal number around 1 by dividing
by the maximum value

    AmpAve1=mean(res1(1,1:6));
    AmpAve2=mean(res1(2,1:6));
    AmpAve3=mean(res1(3,1:6));
    AmpAve4=mean(res1(4,1:6));
    AmpAve5=mean(res1(5,1:6));
    AmpAve6=mean(res1(6,1:6));
    AmpAve7=mean(res1(7,1:6));
    AmpAve8=mean(res1(8,1:6));

AmpAve1_8=[AmpAve1,AmpAve2,AmpAve3,AmpAve4,AmpAve5,AmpAve6,AmpAve7,AmpAve8];

    TdAve1=mean(res3(1,1:6));
    TdAve2=mean(res3(2,1:6));
    TdAve3=mean(res3(3,1:6));
    TdAve4=mean(res3(4,1:6));
    TdAve5=mean(res3(5,1:6));
    TdAve6=mean(res3(6,1:6));
    TdAve7=mean(res3(7,1:6));
    TdAve8=mean(res3(8,1:6));
    TdAve1_8=[TdAve1,TdAve2,TdAve3,TdAve4,TdAve5,TdAve6,TdAve7,TdAve8];

    figure('units','normalized','outerposition',[0 0 1 1],'Visible','off');
    set(gcf,'CreateFcn','set(gcf,''Visible'',''on'')');
    mark = ['k-*'; 'k-<'; 'k->'; 'k-^'; 'k-v';'k-o'; 'k-+'; 'k-p'; 'k-s'; 'k-
d'];
    for i= 1:6
        ax1 = subplot(1,2,1);
        dispnam = strcat('C ',num2str(i));
        plot(freq,res1(:,i),mark(i,:),'DisplayName',dispnam,'LineWidth',1.1);
        pbaspect([1 1 1]) %Sets Aspect Ratio to 1 (Square Plot)
        hold on
        ax3 = subplot(1,2,2);
        plot(freq,res3(:,i),mark(i,:),'DisplayName',dispnam,'LineWidth',1.1);
        pbaspect([1 1 1]) %Sets Aspect Ratio to 1 (Square Plot)
        xlim([0 1]) %Limits X Axis with a range from 0-1
        hold on
    end
    ax1 = subplot(1,2,1);
    dispnam1= 'C-Average'; %Renames Best Fit Line as a low pass filter
    plot11 = plot(freq,AmpAve1_8,'LineWidth',2, 'DisplayName',dispnam1,
'Color','b', 'LineStyle','--');
    xlim([0 1]) %Limits X Axis with a range from 0-1

    ax3 = subplot(1,2,2);
    dispnam1= 'C-Average'; %Renames Best Fit Line as a low pass filter
    plot111 = plot(freq,TdAve1_8,'LineWidth',2, 'DisplayName',dispnam1,
'Color','b', 'LineStyle','--');
    xlim([0 1]) %Limits X Axis with a range from 0-1

    fname1 = strcat(fname,'_TransferFunction');
    fname1 = fullfile('C:\Users\aligs\Desktop\MATLAB\Fres',fname1);
    saveas(gcf,fname1,'tiff')
    cd ..
end
cd ..\..
```

A3 – Phase portraits

```
% Clear variables, workspace and close all open windows
clear
clc
% close all
% Store all variables with 32 bit precision
format long;

allfolders = dir('C:\Users\aligs\Desktop\MATLAB\Fres'); %Main folder for all
case files
for k = 3:length(allfolders) %Starts from real folders by point 3
    myfolder = allfolders(k).name; %Finds the name of the folder
    myfolder = fullfile(allfolders(k).folder,myfolder);%Finds full file
name/file path
    cd(myfolder)%change directory to main folder
    sub = strcat(myfolder,'\T'); %Add \T to original file name
    cd(sub) %Enter one of the Folders
    csvfiles = dir('*.csv'); %Read CSV Files
    am = input('Please input the amplitude -> (0.1), (0.3), (0.6)\n');

    for file = csvfiles' %Loop over all CSV files
        fprintf(1,'Working with %s\n',file.name) %Tracks the file we are
working with & displays it
        fullFileName = fullfile(sub,file.name); %Identifies File patch
        str = file.name; %Identifies File name
        dat = csvread(fullFileName,1,0); %Reads data in File skipping 3 rows &
0 coloumns
        Fs = 1.0/(dat(2,1)-dat(1,1));
        Fr = input('Forcing Frequency = /n');
        fname = str(1:i);

        time = dat(int32(45*Fs)+1:int32(50*Fs),1); %Calculates time increments
of 1 cell from 25-125
        time = time'; %Inverse Time cells
        data = dat(int32(45*Fs)+1:int32(50*Fs),2:7); %Calculates Nu in
increments 1 cell in increments of 1 cell increase 25-125
        data = data'; %Inverse Nu Data
        [rows,columns] = size(data); %Calculates the size of rows & coloumns
pores for Nu
        T = 1/Fs; % Calculates Sampling period
        L = columns; % Calculates Length of signal by using size of coloumns
        n = 2^nextpow2(L); %Calculates the positive next powers of 2

        fname1 = strcat(fname,'_FP'); %Filename suffix _FP added
        fname1 = fullfile('C:\Users\aligs\Desktop\MATLAB\Fres',fname1);

        aa = 1.0+am*sin(2.0*pi*Fr*time); %Input flow signal (inlet)
        figure('units','normalized','outerposition',[0 0 1 1],'Visible','off');
        set(gcf,'CreateFcn','set(gcf,''Visible'',''on'')');
        for i = [1,3,6]
            data(i,:) = data(i,:)/mean(data(i,:));
            plot(aa,data(i,:),'k','LineWidth',2)
            set(gca,'XLim',[0.88,1.12]);
            set(gca,'YLim',[0.4,1.6]);
            axis square
            hold on
            ylabel('Normalised Nu')
            xlabel('Normalized Input Signal')
        end
```

```
        ax = gca;
        ax.FontSize = 22;
        ax.LineWidth = 1.2;
        saveas(gcf,fname1,'tiff')
        hold off
    end
    cd ..
end
cd ..\..
```

A4 – Measure of nonlinearity

```
% Clear variables, workspace and close all open windows
clear
clc
close all
% Store all variables with 32 bit precision
format long;

allfolders = dir('C:\Users\aligs\Desktop\MATLAB\Fres'); %Main folder for all
case files
for k = 3:length(allfolders) %Starts from real folders by point 3
    myfolder = allfolders(k).name; %Finds the name of the folder
    myfolder = fullfile(allfolders(k).folder,myfolder);%Finds full file
name/file path
    cd(myfolder)%change directory to main folder
    sub = strcat(myfolder,'\T'); %Add \T to original file name
    cd(sub) %Enter one of the Folders
    csvfiles = dir('*.csv'); %Read CSV Files
    j = 0;

    figure('units','normalized','outerposition',[0 0 1 1],'Visible','off');
    set(gcf,'CreateFcn','set(gcf,''Visible'',''on'')');
    for file = csvfiles' %Loop over all CSV Files
        fprintf(1,'Working with %s\n',file.name) %Tracks the file we are
working with and displays it
        fullFileName = fullfile(sub,file.name); %Identifies File patch
        str = file.name; %Identifies File name
        dat = csvread(fullFileName,1,0); %Reads data in File skipping 3 rows &
0 coloumns
        j = j+1; %Reads one and adds to counter
        Fs = 1.0/(dat(2,1)-dat(1,1));
        Fr = input('Forcing Frequency = /n');
        fname = str(1:i);

        time = dat(int32(25*Fs)+1:int32(125*Fs),1); %Calculates time increments
of 1 cell from 25-125
        time = time'; %Inverse Time cells
        data = dat(int32(25*Fs)+1:int32(125*Fs),2:7); %Calculates Nu in
increments 1 cell in increments of 1 cell increase 25-125
        data = data'; %Inverse Nu Data
        [rows,columns] = size(data); %Calculates the size of rows & coloumns
pores for Nu
        T = 1/Fs; % Calculates Sampling period
        L = columns; % Calculates Length of signal by using size of coloumns
        n = 2^nextpow2(L); %Calculates the positive next powers of 2

        for i = 1:6 %Loop over the 6 battery cells
```

```
            data(i,:) = data(i,:)/mean(data(i,:)); %Nu Numbers at each pore 
Normalized (Around 1)
            data(i,:) = data(i,:)-mean(data(i,:)); %Nu Numbers at each pore 
Normalized (Around 0)
            yy = fft(data(i,:)); %Calculates the Discrete Fourier Transform
            p2 = size(yy);
            p1 = zeros(p2);
            indx = nearest(Fr*L/Fs+1); %Calculates the Frequency x 100 (+ 1)
            p1(indx-2:indx+2) = 2*yy(indx-2:indx+2);
            y = ifft(p1); y = real(y);
            Mho(i) = norm(data(i,:)-y)/norm(data(i,:));
            nonlin(j,i) = Mho(i);
        end
        mark = ['k-*'; 'k-<'; 'k->'; 'k-^'; 'k-v';'k-o'; 'k-+'; 'k-p'; 'k-s'; 
'k-d'];
        dispnam = strcat('Frequency ',num2str(j));
        plot([1:6],Mho,mark(j,:),'DisplayName',dispnam)
        hold on
    end
    legend('show','orientation','horizontal','location','northoutside');
    title('Nonlinearity Factor in Nusselt Numbers over Different Battery 
Cells')
    ylabel('\mu (-)')
    xlabel('Battery Cells (-)')
    ax = gca;
    ax.FontSize = 12;
    ax.LineWidth = 1.2;
    fname1 = strcat(fname,'_NLT');
    fname1 = fullfile('C:\Users\aligs\Desktop\MATLAB\Fres',fname1);
    saveas(gcf,fname1,'tiff')
    hold off
    fname2 = strcat(fname,'.txt');
    fname2 = fullfile('C:\Users\aligs\Desktop\MATLAB\Fres',fname2);
    dlmwrite(fname2,nonlin,'delimiter','\t','precision',12)
    cd ..
end
cd ..\..
```

Appendix B – Battery cell vibration code

The following code is specific for a modulation amplitude of 30 mm/s and forcing frequency of 10 Hz.

```
#include"udf.h"

#include "math.h"


DEFINE_CG_MOTION(moving_box,dt,vel,omega,time,dtime)

{


real t = time;

NV_S(vel,=,0.0);

NV_S(omega,=,0.0);

vel[1] = 0.03*sin(2*3.14159*10*t);


}
```